

**Model Predictive Control-based Surface Condensation Prevention for
Thermo-active Building Systems (TABS):
In Regard to the Partial Theoretical Model Approach**

by

Deokoh Woo

A dissertation submitted in partial fulfilment
of the requirements for the degree of
Doctor of Philosophy
(Architecture)
in The University of Michigan
2021

Doctoral Committee:

Associate Professor Lars Junghans, Chair
Associate Professor Herek Clack
Associate Professor Mojtaba Navvab
Professor Peter David von Buelow

Deokoh Woo

deokoh@umich.edu

ORCID iD: 0000-0001-5662-8831

© Deokoh Woo 2021

TABLE OF CONTENTS

LIST OF TABLES	v
LIST OF FIGURES	vi
LIST OF APPENDICES	xi
LIST OF ACRONYMS.....	xii
LIST OF NOMENCLATURE	xiii
ABSTRACT.....	xv
CHAPTER 1. Introduction.....	1
1.1. Background.....	1
1.2. Thermo-active Building Systems in Architecture.....	11
1.3 Problem Statement.....	14
CHAPTER 2. Literature Review	18
2.1. Moisture Movement in Building Construction Layers	18
2.2. Surface Condensation Control with a Vapor Retarder.....	22
2.3 Surface Condensation Prediction Models.....	27
2.4. Control Methods for HVAC Systems	30
2.5. Basics of Classical Model Predictive Control	34

2.6. Model Predictive Control for Surface Condensation.....	35
2.7. Dynamic Modeling for Model Predictive Control.....	36
2.7.1 Theoretical Model (White Box Model)	38
2.7.2 Data-driven Model (Black Box Model).....	38
2.7.3 Partial Theoretical Model (Grey Box Model).....	41
2.8. Long-term Model Predictive Control.....	44
CHAPTER 3. Research Purpose.....	47
3.1. Research Question	48
3.2. Research Importance.....	49
CHAPTER 4. Methodology.....	51
4.1. Dynamic Modeling with the Partial Theoretical Model	52
4.1.1. Dynamic Modeling of Heat and Moisture Transfer in Building Construction	52
4.1.2. Dynamic Modeling of Buildings	55
4.1.3. Solar Heat Flux	58
4.2. Experimental Setup and Instrumentation.....	61
4.3. Model Calibration Using a Curve-fitting Process.....	67
4.4. An MPC-based Surface Condensation Prevention Framework Development	69
4.5. Site-specific Surface Condensation Prevention Performance Analysis.....	73
4.6. Energy Savings and Cost Reduction by the MPC-based TABS Operation	74
CHAPTER 5. Results and Discussion	80

5.1. Experiment Results	80
5.2. Model calibration Results	81
5.3. Required Time Charts of Surface Condensation Development	82
5.4. An MPC-based Surface Condensation Prevention Framework	86
5.5. Site-specific Surface Condensation Prevention Performance.....	90
5.6. Energy Savings and Cost Reduction by the MPC-based TABS Operation	93
CHAPTER 6. Conclusion	103
6.1. Highlights.....	103
6.2. Conclusions.....	103
6.3. Limitations	110
6.4. Future Works.....	111
REFERENCES	112
APPENDICES	118

LIST OF TABLES

Table 1. Comparison between forced air-based cooling systems and hydronic-based radiant cooling systems.....	3
Table 2. Comparison among forced air-based cooling, hydronic-based cooling with mech. ventilation, and hydronic-based cooling with natural ventilation.....	7
Table 3. List of TABS applied buildings with climatic regions	16
Table 4. Three mechanisms of moisture movement can occur while TABS operation.....	20
Table 5. Vapor retarder classifications.....	23
Table 6. Vapor retarder code recommendations from International Residential Code.....	25
Table 7. Summary of literature review in heat and moisture transfer models.....	28
Table 8. Comparison of dynamic modeling approaches for MPC	38
Table 9. Test condition settings	63
Table 10. Physical parameters and their ranges for the curve-fitting process	68
Table 11. The selected site for each climate zone (Energy savings and cost reduction analysis)	75
Table 12. The building envelope requirements for each climate zone (ASHRAE 90.1)	77
Table 13. MSE change with curve-fitting process	81
Table 14. The physical property values and the convective heat transfer coefficient obtained after the curve-fitting process	82
Table 15. Required time to develop surface condensation from measurement and simulation	84
Table 16. Annual user cooling energy demand for different climatic regions	93
Table 17. Annual site cooling energy for different climate regions and cooling modes	98
Table 18. Annual cooling operational cost for different climate regions and cooling modes	102
Table 19. Summary of parameter values for the site cooling energy calculation.....	163

LIST OF FIGURES

Figure 1. Percentage of people dissatisfied (PPD) from different types of radiant asymmetry.	2
Figure 2. Schematic comparison between the forced air-based cooling system and hydronic-based radiant cooling system.....	6
Figure 3. Three types of hydronic-based radiant cooling systems.....	8
Figure 4. Theoretical diagram of peak shaving with TABS.....	9
Figure 5. Schematic diagram of the water pipe-embedded TABS and its operation on ceiling.....	10
Figure 6. The Zollverein School with TABS, Essen, Germany	12
Figure 7. The Fred Kaiser Building with TABS, Vancouver, Canada.....	13
Figure 8. The Crown Hall with the surface radiant cooling system, Chicago, United States..	14
Figure 9. TABS widely used climatic regions vs. Risky TABS application	15
Figure 10. The condensation occurrence and the resultant mold growth on the concrete surfaces	17
Figure 11. IECC climate zone map	23
Figure 12. Dew point/temperature curve and saturation/partial vapor pressure curve in TABS.....	27
Figure 13. Classification of control methods for HVAC systems.....	30
Figure 14. Schematic diagram of predictive model control for indoor temperature.....	33
Figure 15. The basic framework of model predictive Control for HVAC systems.....	35
Figure 16. Slow and gradual hygrothermal response time of heavy construction layer	44
Figure 17. Surface condensation control with long-term MPC	45
Figure 18. Outline of the dissertation.....	48
Figure 19. Overview of the proposed MPC-based TABS operation.....	51
Figure 20. Solar radiation on a tilted surface	58

Figure 21-a. Experimental equipment settings of the chamber	62
Figure 21-b. Measuring points inside the chamber.....	62
Figure 22. Measuring equipment setting.....	63
Figure 23-a. Initial test results: surface relative humidity, φ_{sf}	66
Figure 23-b. Initial test results: surface temperature, T_{sf}	66
Figure 23-c. Initial test results: volumetric moisture content, w	66
Figure 24. Mean radiant temperature change according to the position of occupants.....	71
Figure 25. Analyzed U.S. sites in this study (based on the IECC climate zone classification)	74
Figure 26. Location of the selected sites for each climate zone (Energy savings and cost reduction analysis)	75
Figure 27. Prototype medium-size office building defined by the Building Energy Code Program.....	76
Figure 28. Measured data and simulation data after the curve-fitting process	80
Figure 29. Validation results for the required time of surface condensation development on the concrete	83
Figure 30. The required time charts of surface condensation development on the concrete layer.....	85
Figure 31. Sensitivity study of control horizon.....	88
Figure 32. Schematic MPC-based TABS operation over the time horizon	89
Figure 33. MPC-based TABS operation procedure	90
Figure 34. Geographic plot: surface condensation prevention performance using the MPC framework in the U.S.....	92
Figure 35. Annual user cooling energy demand for different climatic regions.....	93
Figure 36-a. Annual site cooling energy for different climate regions (1A–4C).....	96
Figure 36-b. Annual site cooling energy for different climate regions (5A–7A)	97
Figure 37. Annual site cooling energy for different cooling modes.....	99
Figure 38. Annual cooling operational cost for different climate regions and cooling modes	101
Figure 39. Site-specific surface condensation prevention performance	107
Figure 40. Site-specific surface condensation prevention performance (Geographic plot)...	107
Figure 41. Site-specific distribution energy savings potential	108

Figure 42. Site-specific distribution energy savings potential (Geographic plot)	108
Figure 43. Site-specific operational cost reduction.....	109
Figure 44. Site-specific operational cost reduction (Geographic plot)	109
Figure 45. Volumetric moisture content change in concrete layer with TABS operation, disregarding surface condensation risk (Miami_FL).....	145
Figure 46. Surface condensation development on TABS with on/off control and MPC (Miami_FL).....	145
Figure 47. Outdoor air temperature and indoor operative temperature with MPC-based TABS operation (Miami_FL).....	146
Figure 48. TABS operation with the MPC-based surface condensation prevention framework in cooling season (Miami_FL)	146
Figure 49. Volumetric moisture content change in concrete layer with TABS operation, disregarding surface condensation risk (Austin_TX)	147
Figure 50. Surface condensation development on TABS with on/off control and MPC (Austin_TX).....	147
Figure 51. Outdoor air temperature and indoor operative temperature with MPC-based TABS operation (Austin_TX).....	148
Figure 52. TABS operation with the MPC-based surface condensation prevention framework in cooling season (Austin_TX).....	148
Figure 53. Volumetric moisture content change in concrete layer with TABS operation, disregarding surface condensation risk (Charleston_SC).....	149
Figure 54. Surface condensation development on TABS with on/off control and MPC (Charleston_SC).....	149
Figure 55. Outdoor air temperature and indoor operative temperature with MPC-based TABS operation (Charleston_SC).....	150
Figure 56. TABS operation with the MPC-based surface condensation prevention framework in cooling season (Charleston_SC)	150
Figure 57. Volumetric moisture content change in concrete layer with TABS operation, disregarding surface condensation risk (San Francisco_CA)	151
Figure 58. Surface condensation development on TABS with on/off control and MPC (San Francisco_CA)	151

Figure 59. Outdoor air temperature and indoor operative temperature with MPC-based TABS operation (San Francisco_CA).....	152
Figure 60. TABS operation with the MPC-based surface condensation prevention framework in cooling season (San Francisco_CA)	152
Figure 61. Volumetric moisture content change in concrete layer with TABS operation, disregarding surface condensation risk (Philadelphia_PA)	153
Figure 62. Surface condensation development on TABS with on/off control and MPC (Philadelphia_PA).....	153
Figure 63. Outdoor air temperature and indoor operative temperature with MPC-based TABS operation (Philadelphia_PA).....	154
Figure 64. TABS operation with the MPC-based surface condensation prevention framework in cooling season (Philadelphia_PA).....	154
Figure 65. Volumetric moisture content change in concrete layer with TABS operation, disregarding surface condensation risk (Crescent City_CA).....	155
Figure 66. Surface condensation development on TABS with on/off control and MPC (Crescent City_CA)	155
Figure 67. Outdoor air temperature and indoor operative temperature with MPC-based TABS operation (Crescent City_CA)	156
Figure 68. TABS operation with the MPC-based surface condensation prevention framework in cooling season (Crescent City_CA).....	156
Figure 69. Volumetric moisture content change in concrete layer with TABS operation, disregarding surface condensation risk (Chicago_IL)	157
Figure 70. Surface condensation development on TABS with on/off control and MPC (Chicago_IL).....	157
Figure 71. Outdoor air temperature and indoor operative temperature with MPC-based TABS operation (Chicago_IL).....	158
Figure 72. TABS operation with the MPC-based surface condensation prevention framework in cooling season (Chicago_IL)	158
Figure 73. Volumetric moisture content change in concrete layer with TABS operation, disregarding surface condensation risk (Minneapolis_MN).....	159

Figure 74. Surface condensation development on TABS with on/off control and MPC (Minneapolis_MN)	159
Figure 75. Outdoor air temperature and indoor operative temperature with MPC-based TABS operation (Minneapolis_MN)	160
Figure 76. TABS operation with the MPC-based surface condensation prevention framework in cooling season (Minneapolis_MN)	160
Figure 77. Volumetric moisture content change in concrete layer with TABS operation, disregarding surface condensation risk (Duluth_MN).....	161
Figure 78. Surface condensation development on TABS with on/off control and MPC (Duluth_MN)	161
Figure 79. Outdoor air temperature and indoor operative temperature with MPC-based TABS operation (Duluth_MN)	162
Figure 80. TABS operation with the MPC-based surface condensation prevention framework in cooling season (Duluth_MN).....	162

LIST OF APPENDICES

A. The Whole Process of Solving the MPC Problem.....	118
B. The Analyzed United States Sites Lists.....	121
C. Annual Simulation Result of MPC-based TABS Operation.....	145
D. Summary of Parameter Values for the Site Cooling Energy Calculation.....	163

LIST OF ACRONYMS

ANN	Artificial neural network
ASHRAE	American Society of Heating, Refrigerating and Air-conditioning Engineers
COP	Coefficient of performance
CLT	Cross-laminated timber
HVAC	Heating, ventilation, and air conditioning
IAQ	Indoor air quality
IECC	International Energy Conservation Code
KNN	K-nearest neighbor
LIM	Lowest isopleth for mold
MLP	Multilayer perceptron
MLR	Multiple linear regression
MRT	Mean radiant temperature
MPC	Model predictive control
MSE	Mean squared error
NLP	Nonlinear programming
PID	Proportional–integral–derivative
RC	Resistance-Capacitance
SHGC	Solar heat gain coefficient
TABS	Thermo-active building system

LIST OF NOMENCLATURE

a	Thermal diffusivity of solid (m^2/s)
C_p	Specific heat capacity at constant pressure ($\text{J}/\text{kg K}$)
F_o	Fourier number
h_c	Convective heat transfer coefficient ($\text{W}/\text{m}^2 \text{K}$)
h_m	Moisture convective coefficient ($\text{W}/\text{m}^2 \text{K}$)
h_s	Space heat exchange coefficient ($\text{W}/\text{m}^2 \text{K}$)
$h(T)$	The heat of vaporization (J/kg)
K	Hydraulic conductivity for liquid ($\text{kg}/\text{m s Pa}$)
k	Thermal conductivity ($\text{W}/\text{m K}$)
\dot{L}_{in}	Internal moisture source
\dot{m}	Vapor flux ($\text{kg}/\text{m}^2 \text{s}$)
μ	Vapor permeability ($\text{kg}/\text{m s Pa}$)
N	Prediction horizon
P	Pressure (Pa)
Φ_{solar}	Solar heat flux (W/m^2)
\dot{Q}	Internal heat source
\dot{q}	Heat flux (W/m^2)
ρ	Density (kg/m^3)
S	Surface area (m^2)
T	Temperature ($^{\circ}\text{C}$)
T_1	Initial temperature ($^{\circ}\text{C}$)
T_{∞}	Fluid temperature ($^{\circ}\text{C}$)
t	Time (s)
θ	Exposure angle of surface ($^{\circ}$)
u	Command effort
V	Volume
w	Moisture content (%)
ω	Weighting factor
φ	Relative humidity
x	Length (m)
y	Output

Subscripts

d	Dry
i	Ice
in	Indoor air
l	Liquid water
mr	Mean radiant

<i>op</i>	Operative
<i>set</i>	Set point
<i>sf</i>	Surface
<i>v</i>	Vapor

ABSTRACT

The potential risk of developing surface condensation keeps thermo-active building systems (TABS) from being applied in buildings located in partly warm and humid climate regions. This study presents a framework for model predictive control (MPC)-based surface condensation prevention that can avoid the surface condensation during the cooling periods when the TABS is in operation. Because MPC determines the input signal for the system not only based on the current states but also on the impact that the actions will have on the future states, it is suitable for anticipatory surface condensation control that must respond to both dynamic indoor condition changes and the time-delay in hygrothermal transfer in advance. Heat and moisture transfer dynamic models were developed for prediction of future states and these dynamic models were calibrated with the measured data to improve the surface condensation prediction accuracy. Based on future states predicted by the calibrated dynamic models, the MPC-based condensation prevention framework adjusts the surface temperature for the TABS in ways that ensure indoor thermal comfort and energy efficiency without the development of surface condensation. The proposed MPC-based surface condensation prevention framework reduced the surface condensation occurrence risk as well as the cooling energy even when the TABS is in operation under warm and humid climate regions. Given the growing demand for the TABS, the proposed MPC framework meets a critical need. By controlling the potential risk of surface condensation development, it can extend TABS use to an area in which climate conditions had made them infeasible.

CHAPTER 1. Introduction

1.1. Background

The effect of greenhouse gas emissions on the global climate is one of the century's main problems. Various approaches to reducing greenhouse gas emissions have been studied. Because the built environment accounts for almost 40 % of industrialized society's total energy demand [1] and roughly 20 % of the total CO₂ emission [2], targeting the built environment has proven to be the most economically beneficial strategy for greenhouse gas emissions reduction [3].

A generally accepted strategy in achieving greenhouse gas emissions reduction aims to apply energy-efficient heating or cooling technologies in buildings. To accomplish the energy-efficient heating or cooling technologies in buildings, occupant's comfort needs to be maintained with minimum energy input to the systems. Based on the American Society of Heating, Refrigerating and Air-conditioning Engineers (ASHRAE) Standard 55 [4], thermal comfort for a person is defined as *a condition of mind that expresses satisfaction with the thermal environment*'. Generally, the following six comfort parameters are widely accepted for determining the indoor thermal comfort for occupants: 1) air temperature, 2) mean radiant temperature, 3) air velocity, 4) vapor pressure in ambient air, 5) activity level, and 6) thermal resistance of clothing.

Among these parameters, air temperature, mean radiant temperature, air velocity, and vapor pressure in ambient air can be controlled with heating or cooling technologies. However, in many cases, heating or cooling technologies are operated based on ambient air conditions only, disregarding the impacts of indoor surface radiant temperature [5]. When we ignore the influence

of indoor surface radiant temperature on thermal comfort, occupants may experience discomfort conditions like radiant asymmetry [4]. Figure 1 shows how much people experience thermal discomfort to the radiant asymmetry [6]. According to Figure 1, people are more sensitive to asymmetry caused by an overhead warm surface than a cold surface. This leads to facts that: 1) both air temperature and indoor surface radiant temperature should be considered altogether to maintain occupants' thermal comfort, and 2) there is excellent energy savings potential of utilizing surface radiant cooling systems on the ceiling side.

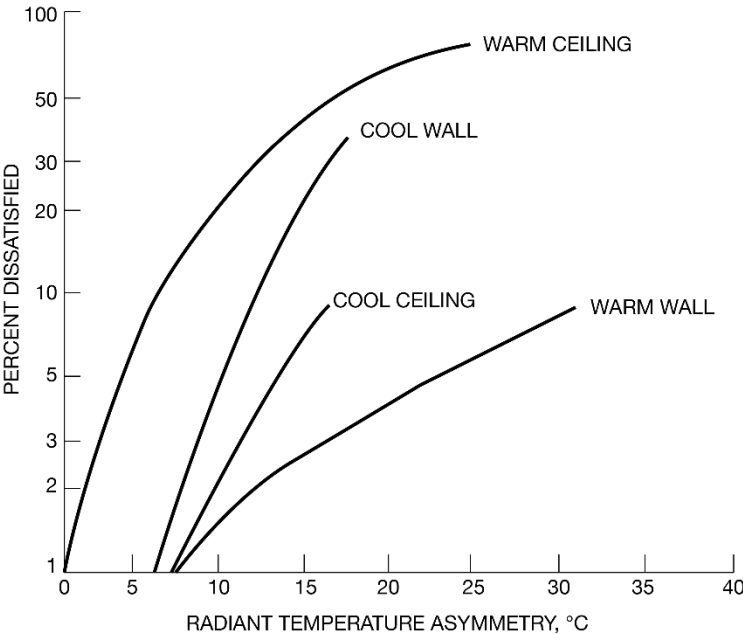


Figure 1. Percentage of people dissatisfied (PPD) from different types of radiant asymmetry

Over the past few decades, numerous cooling technologies have been examined to reduce buildings' cooling energy. One of the most promising strategies is to use cold surfaces as a radiant cooling device to reduce the cooling load for multi-story buildings [7]. The radiant cooling system refers to using cooled shells or construction layers to remove sensible indoor heat by thermal radiation. The radiant cooling systems can be classified into non-hydronic-based systems (or air-

based systems) and hydronic-based systems based on what medium they use. Among these two systems, the hydronic-based radiant cooling system is considered more energy-efficient because of its less transport energy input than the non-hydronic-based system. Given the same volume, water has much more capacity to deliver heat energy than air, leading to significant transport energy savings for the hydronic-based systems than the air-based systems.

Table 1. Comparison between forced air-based cooling systems and hydronic-based radiant cooling systems

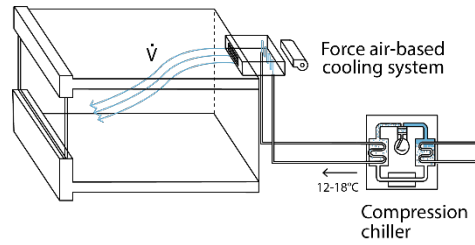
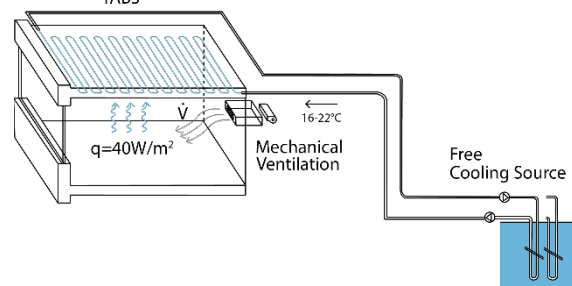
Forced air-based cooling systems	Hydronic-based radiant cooling systems
 <p data-bbox="194 997 406 1081">Need to deal with: - Cooling load (q) - Ventilation load (\dot{V})</p>	 <p data-bbox="812 997 1412 1134">Need to deal with: - Cooling load (q) A sub-mechanical ventilation cooling systems (or natural ventilation) can deal with ventilation load (\dot{V}) to maintain indoor air quality</p>

Table 1 shows a conceptual comparison between forced air-based cooling systems and hydronic-based radiant cooling systems. The hydronic-based radiant cooling systems have the following advantages compared to the conventional forced air-based cooling systems. First, the relatively high heat capacity of water allows the hydronic-based radiant cooling system to have a smaller distribution system size. In general, 10mm radius water pipes are installed within or adjacent to the radiant cooling systems at intervals of 150-200mm [8]. This small space required for a hydronic-based radiant cooling distribution system can bring greater flexibility in the architectural design practice. Therefore, many designers and planners adopted the hydronic-based radiant cooling systems in many multi-story building projects to bring more freedom to the design decision process [8].

Second, the radiant cooling systems can lead to significant energy savings by isolating the control for cooling and ventilation [9]. In the forced air-based cooling systems, the amount of air conditioning is decided considering both cooling load and ventilation demand. However, the calculated amount derived from the cooling demand and ventilation demand is rarely equal [8]; this discrepancy can lead to a redundant energy input for air conditioning and transport energy of the forced air-based cooling systems. Potentially, some amount of power for air conditioning can be reduced by recirculating the conditioned air within the air-based cooling systems. Still, this air recirculation strategy is not applicable for multi-story buildings with a large occupant density because most of the returned air needs to be replaced with the outdoor air to keep an acceptable indoor air quality.

In contrast, the radiant cooling systems allow an accurate control for both cooling and ventilation by separating each other. In general, the radiant cooling systems are coupled with a sub-mechanical ventilation cooling system [8]; the majority of sensible cooling load is covered with the radiant cooling systems while the rest of the cooling load and ventilation demand is controlled by the sub-mechanical ventilation cooling systems. This separation in cooling and ventilation functions within the system will allow more accurate control for cooling load and ventilation demand, thus enabling significant energy savings.

Third, when the radiant cooling systems are coupled with the sub-mechanical ventilation cooling systems, a higher thermal comfort level can be provided to the occupants. As addressed above, six factors impact human thermal comfort [10]: 1) air temperature, 2) mean radiant temperature, 3) air velocity, 4) vapor pressure in ambient air, 5) activity level, and 6) thermal resistance of clothing. Besides two personal factors (activity level and thermal resistance of clothing), the other four elements can be controlled by the cooling system to achieve a higher

thermal comfort level. The forced air-based cooling systems only contain three of these factors, ignoring the radiant temperature. Disregarding the impact of radiant temperature on occupants' thermal comfort may result in uncomfortable conditions for occupants such as cold draft or radiant asymmetry. For example, when lightly clothed occupants are working in front of the desk under moderate indoor airspeed (< 0.2 m/s), they tend to exchange more of their sensible heat through radiation than convection [8]. Thus, once the radiant cooling systems are coupled with the sub-mechanical ventilation cooling systems, it can deal with the sensible and latent cooling load and control the radiant surface temperature, thus creating genuinely comfortable indoor conditions for the occupants.

Fourth, the hydronic-based radiant cooling systems can be operated more energy-efficiently than the forced air-based cooling systems because of their effective ways of exchanging heat through the surface radiant cooling effect [8]. Because heat exchange through radiation is more dominant than convection under the same cooling energy input [8], a supply water temperature for radiant cooling systems can be higher than a supply air temperature for the forced air-based system to bring the same cooling effect to the occupants (Figure 2). By having the supply water temperature (from the evaporator) close to the temperature of the condenser where waste heat is emitted, the coefficient of performance (COP) for the chillers can be increased [11]. Additionally, when this condenser is connected to a ground source loop or a cooling tower, the COP for the chillers can be increased significantly.

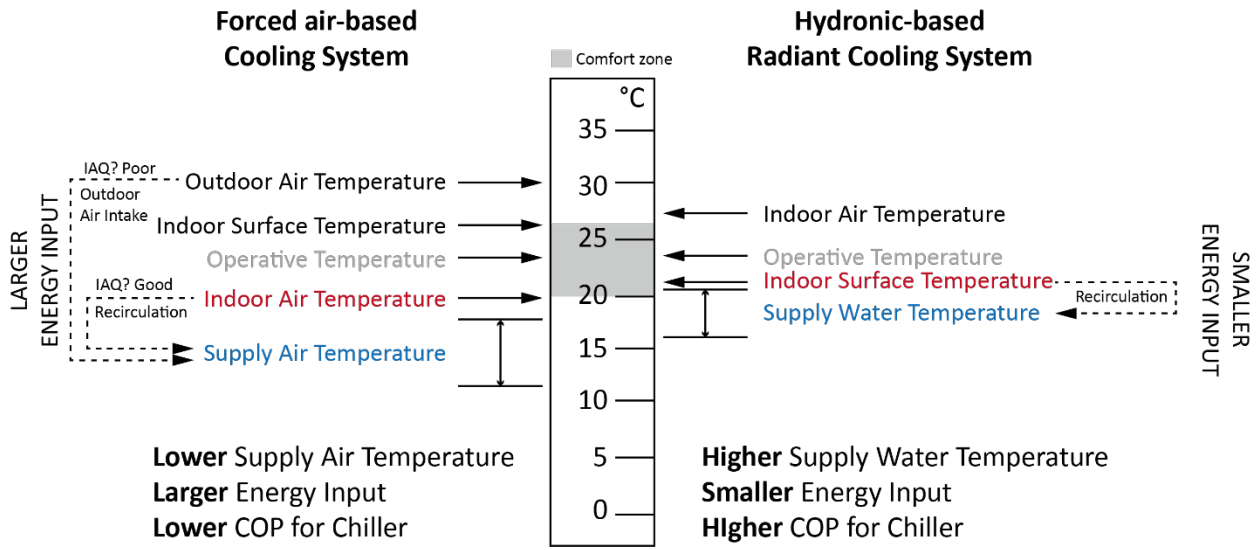
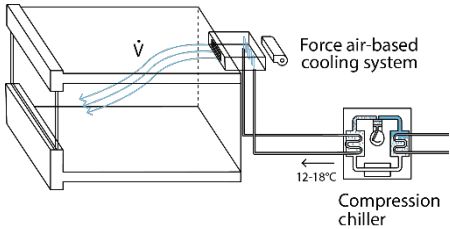
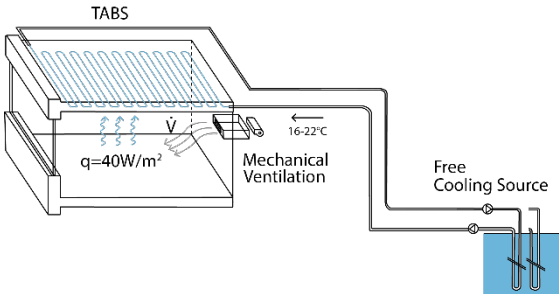
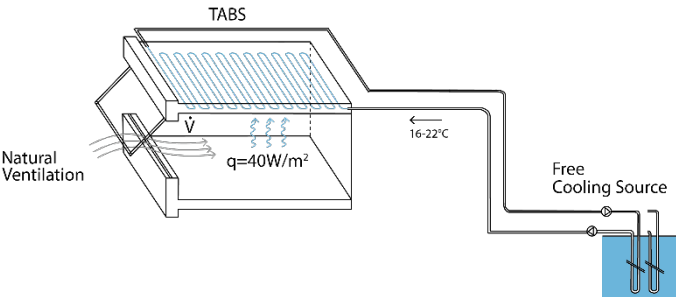


Figure 2. Schematic comparison between the forced air-based cooling system and hydronic-based radiant cooling system

Table 2. Comparison among forced air-based cooling, hydronic-based cooling with mech. ventilation, and hydronic-based cooling with natural ventilation

Cooling mode	Ventilation load (\dot{V})	Cooling load (q)	Feed temperature (T)	Thermal comfort level	Distribution energy
Forced air-based cooling systems					
	Determined by: IAQ and Cooling load	Determined by: IAQ and Cooling load	Low-temperature cooling 12-18°C	Can be bad	High
Hydronic-based cooling with mechanical ventilation					
	Determined by: IAQ	Determined by: Cooling load	High-temperature cooling 16-22°C	Better	Low
Hydronic-based cooling with natural ventilation					
	Determined by: IAQ	Determined by: Cooling load	High-temperature cooling 16-22°C	Better	Low

Three types of hydronic-based radiant cooling systems have been identified (Figure 3): radiant cooling panels, embedded surface cooling systems, and thermo-active building systems (TABS) [12]. The radiant cooling panels are suspended metal panels that produce cold surfaces to remove indoor heat by radiation. The cold surface temperature can be made by water pipes laid on the metal panels. The embedded surface cooling system exchanges heat through the embedded water pipes within gypsum board layers, but the system is insulated from the building construction layer. The thermo-active building systems (TABS), on the other hand, pass cooled water directly through the water pipes embedded in construction layers for cooling rooms [13].

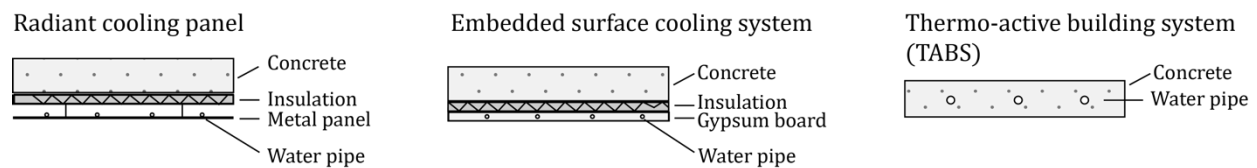


Figure 3. Three types of hydronic-based radiant cooling systems

Among the three types of hydronic-based radiant cooling systems, the TABS can exploit the thermal storage effect significantly better over the other systems by cooling down the construction layers (e.g., concrete slab) directly. The heavy construction layers of TABS are pre-cooled with nighttime cooling sources (outdoor air or groundwater sources nearby) a few hours ahead of occupancy to cope with rapidly increasing cooling energy demand during the daytime. On the other hand, the heat stored within the heavy construction layers of TABS during the daytime can be kept beyond the time of occupancy and is then cooled down by the nighttime cooling sources (outdoor air or groundwater sources nearby) that have been produced during the less expensive operational cost period (Figure 4). Therefore, both the peak cooling load and the operating cost for cooling can be reduced significantly [14].

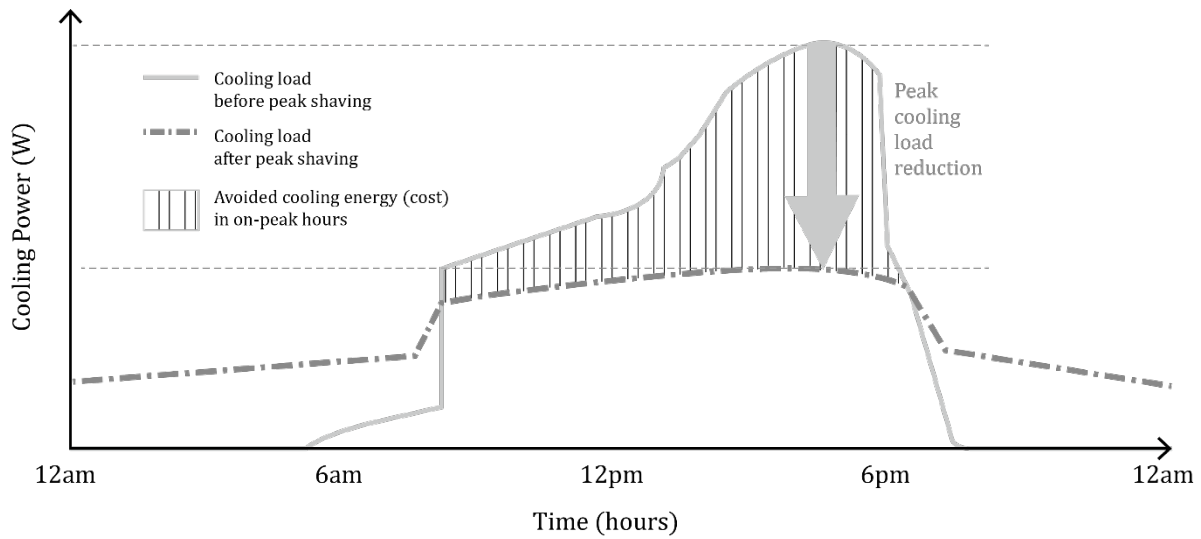


Figure 4. Theoretical diagram of peak shaving with TABS

Besides the thermal storage effect of TABS, the low initial installation cost for the TABS is another advantage [11]. Because the TABS only requires the installation of pipes or tubes inside the concrete layers, initial installation costs for new construction buildings are considered more cost-efficient than those for the conventional forced air-based cooling systems.

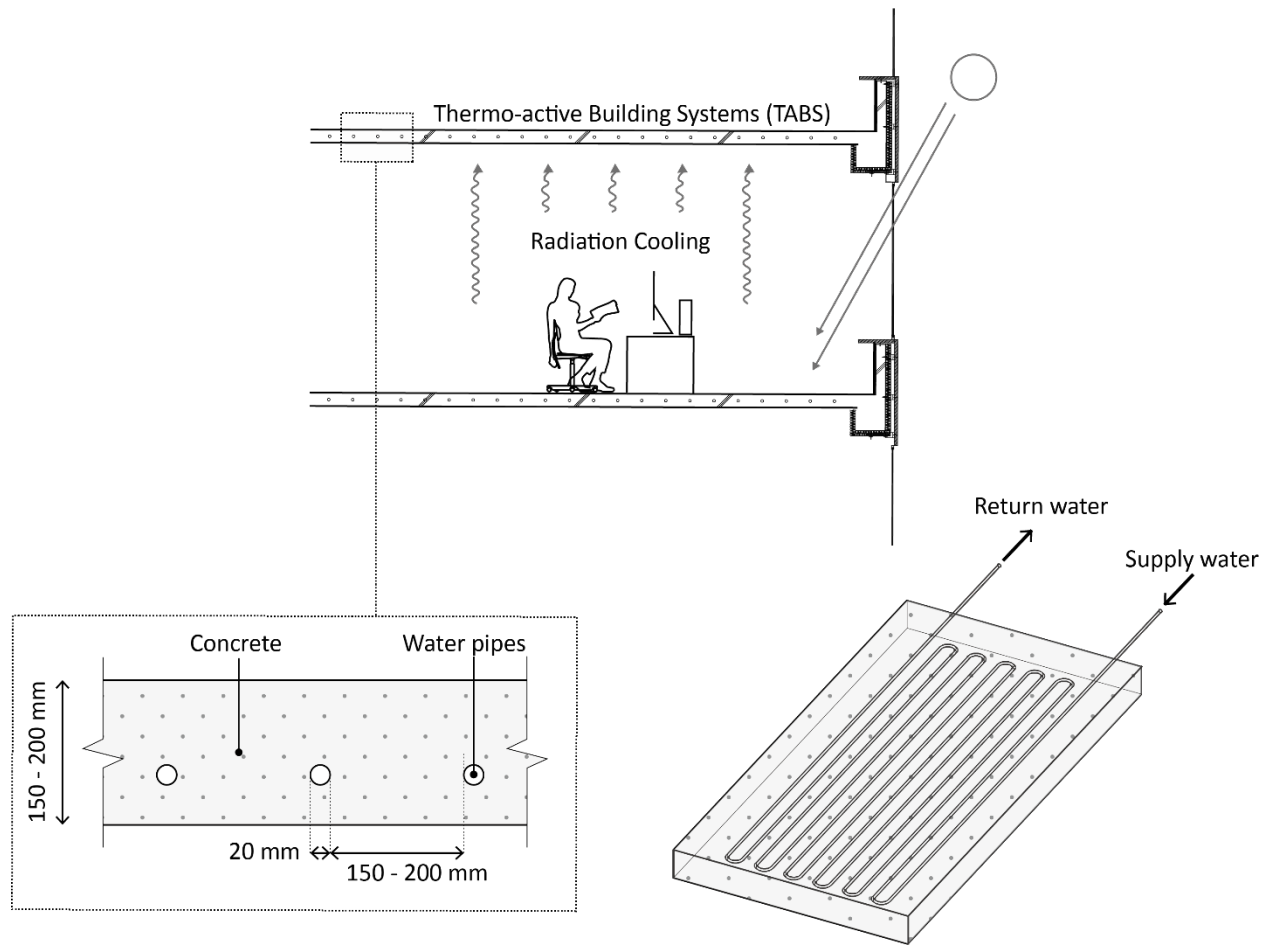


Figure 5. Schematic diagram of the water pipe-embedded TABS and its operation on ceiling

When utilizing the TABS for cooling, the following should be considered with caution. First, the installation of TABS on the structural systems should be avoided [8]. The TABS should be installed in the less load-bearing structures because hollow pipes or tubes do not have load-bearing capability. Second, designers or engineers should consider installing noise buffers underneath the TABS to control the potential noise problems that can be caused by flowing water through the embedded water pipes or tubes.

1.2. Thermo-active Building Systems in Architecture

By the beginning of this century, thermo-active buildings systems (TABS) are gaining more technological momentum because of the significant cost-saving and high occupant thermal satisfaction level. The TABS has been widely utilized for cooling in multi-story buildings in central Europe (Switzerland, Germany, Austria, etc.) and spread out to North America and Asia partly [11].

Starting from the 1990s, many practitioners and architects in Europe adopted TABS as the major cooling system for their projects. In Germany, the TABS is also one of the most widely used cooling systems for multi-story buildings. The Zollverein school of management and design (Figure 6), located in Essen, is a good example that solved its design challenge by utilizing the TABS. The building was designed by renowned architectural firm SANAA. In the initial design phase, this project's main challenge was to achieve the passive house standard for the building envelopes. To achieve the standard, relatively thick wall construction and insulation were required, which was not a very favorable situation for the design team because indoor spaces would be compromised, and initial insulation costs would increase. Thus, the engineers came up with TABS integrated with a free source of heating and cooling. For the heating, they reused the heated water from the 1000 m -deep mine shafts; for the cooling, the cooling tower produced cold water by exchanging heat with low nighttime outdoor air temperature. By utilizing the free source of heating and cooling for the TABS, the thickness of building envelopes could remain as they initially planned. Compared to the conventional air-based HVAC system, significant heating and cooling energy savings were achieved thanks to the TABS. The installation cost of TABS for heating and cooling systems is one-third of a conventional forced air-based cooling system [15].

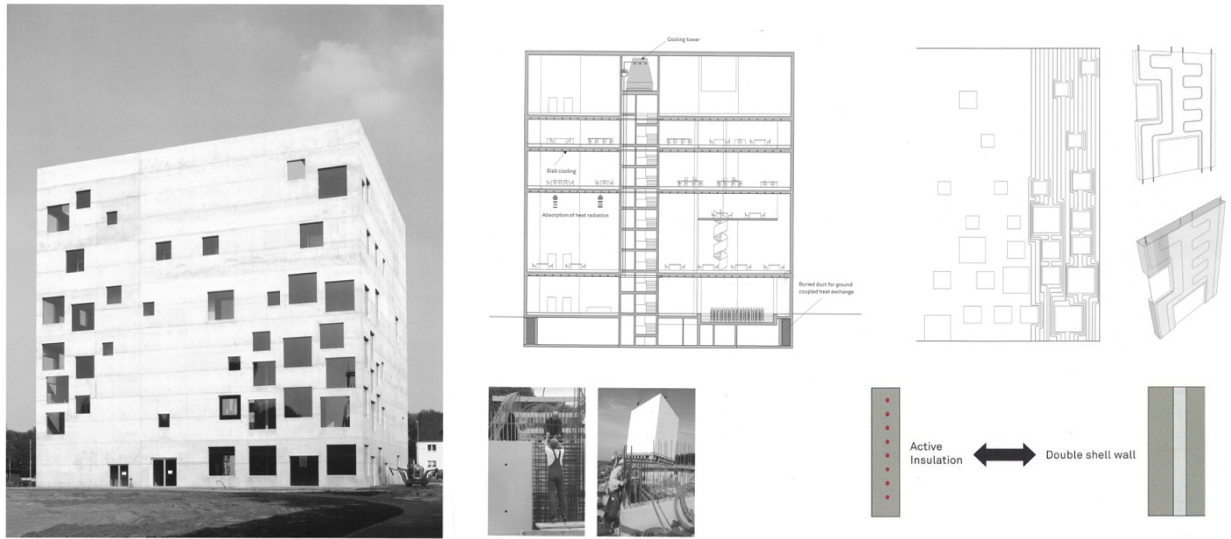


Figure 6. The Zollverein School with TABS, Essen, Germany [15]

After the energy and cost savings potential of the TABS has been proven throughout many projects in central Europe, newly built building projects in North America started to adopt the TABS as a primary cooling system. The Fred Kaiser building at the University of British Columbia (Figure 7), located in Vancouver, is a multi-story building that adopted the TABS for heating and cooling. A cooling tower at the rooftop produces cold water from the nighttime cold outdoor temperature; the produced cold water is distributed to each room for cooling. The building could save approximately 55% of energy compared to Canada's building code, thanks to the TABS [15].

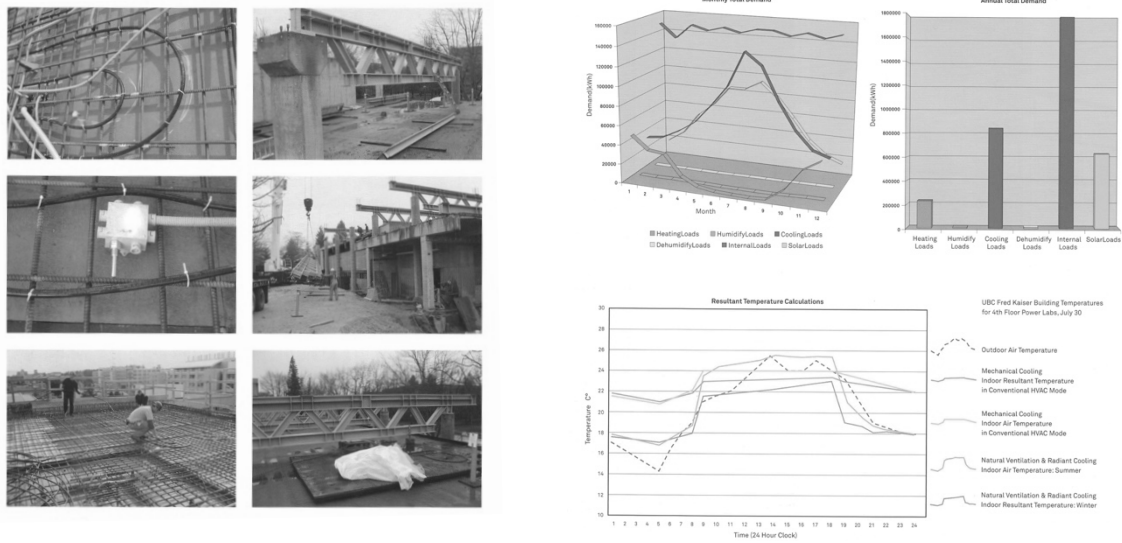


Figure 7. The Fred Kaiser Building with TABS, Vancouver, Canada [15]

When historic buildings require a major HVAC systems renovation without penalizing aesthetic aspects of the spaces' original design features, the hydronic-based radiant cooling systems can be a solution. Crown Hall (Figure 8) in Chicago, Illinois, was designed by Mies van der Rohe. The building initially lacked an air-conditioning system; however, an increase in enrollment to the school led to the renovation of the building with a cooling system. Unfortunately, the renovation was implemented disregarding the original design integrity of Crown Hall; air ducts were exposed to the indoors. After the building was granted National Historic Landmark status in 2001, the building went through a second major renovation of the cooling system. A surface radiant cooling system replaced all of the exposed air ducts. By replacing all of the ductwork with the surface radiant cooling system, the building could recover the purity of the space that was intended by Mies [15].

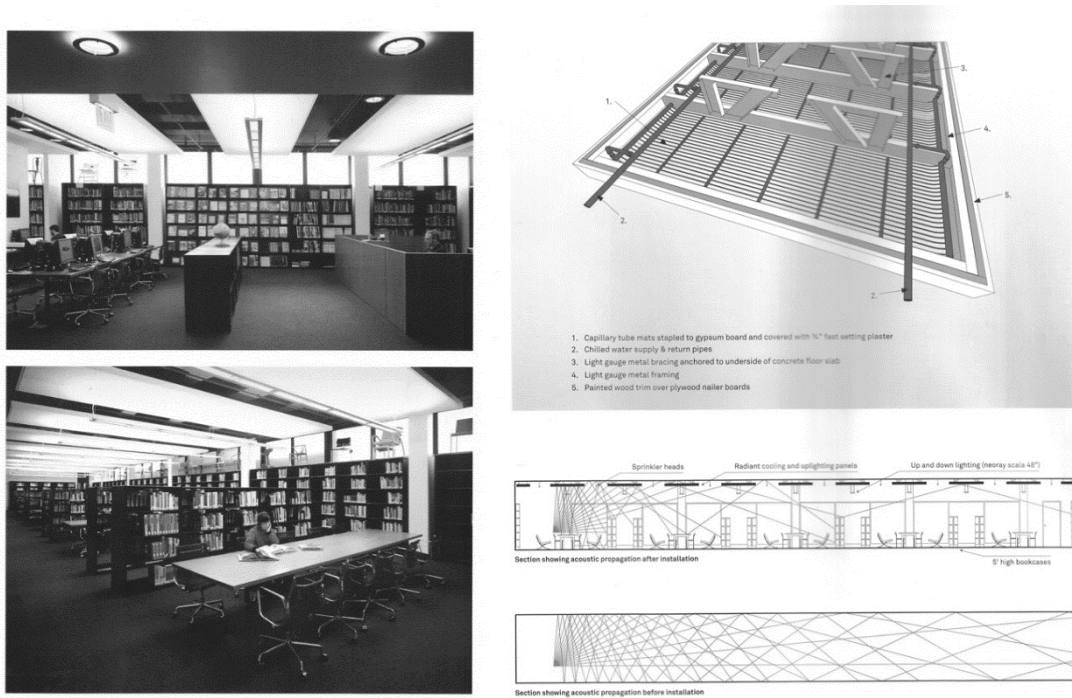


Figure 8. The Crown Hall with the surface radiant cooling system, Chicago, United States [15]

1.3 Problem Statement

Although the TABS has proven to be a promising cooling technology and is widely used in Central Europe and partly in North America, many practitioners and engineers still consider the TABS an unsuitable cooling technology in humid summer areas [8]. This is because the radiant cooling systems, including the TABS, cannot control the humidity level in the air. Thus, surface condensation can occur when it is used in areas with humid summer seasons. The green shaded areas on Figure 9 indicate the climatic regions where TABS have been widely used; the red shaded areas on Figure 9 show the climatic areas with a high risk of surface condensation development while TABS is in operation. These red shaded areas are classified as "Group A: Tropical climates" under the Koppen climate classification with warm and humid summer seasons.

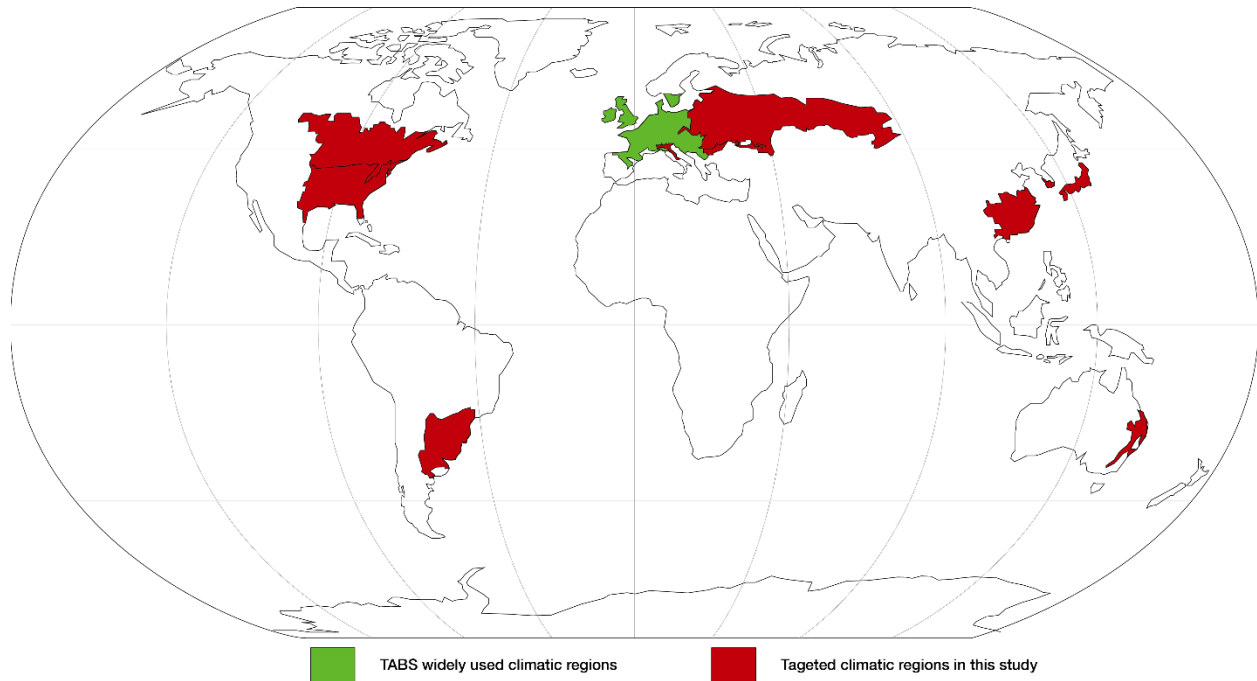


Figure 9. TABS widely used climatic regions vs. Risky TABS application

Because of this potential risk of developing surface condensation, surface radiant cooling systems, including the TABS, are not recommended in the regions with warm and humid summer (red shaded areas in Figure 9). For example, Crown Hall requires an automated dehumidification system in addition to the radiant cooling system to prevent surface condensation. Without the dehumidification process, warm and humid air coming from Lake Michigan would meet the system's cold surface, leading to the surface condensation occurrence on the method applied in Crown Hall. As shown in Table 3, more than two-thirds of TABS-applied buildings are located in climatic regions with less humid summer; the rest are situated in the areas with warm and often humid summer seasons.

Table 3. List of TABS applied buildings with climatic regions

	Project	Location	Climate Classification (Koppen Geiger)	Condition in Summer
1	Charles Hostler Student Recreation Center	Beirut, Lebanon	Csa, Mediterranean climate	Dry
2	Dolce Vita Tejo	Lisbon, Portugal	Csa, Mediterranean climate	Dry
3	IDOM Company Headquarters	Madrid, Spain	Csa, Mediterranean climate	Dry
4	Fred Kaiser Building	Vancouver, Canada	Csb, Mediterranean climate	Warm and dry
5	Euromed Clinic	Furth, Germany	Cfb, Oceanic climate	Mild
6	Semmelweis Medical University	Budapest, Hungary	Cfb, Oceanic climate	Mild
7	Zollverein School	Essen, German	Cfb, Oceanic climate	Mild
8	Südwestmetall Office Building	Heilbronn, Germany	Cfb, Oceanic climate	Mild
9	Dauerhaft wandelbar	Stuttgart, Germany	Cfb, Oceanic climate	Mild
10	Wohnhaus	Basel, Switzerland	Cfb, Oceanic climate	Mild
11	Middelfart Savings Bank	Middelfart, Denmark	Cfb, Oceanic climate	Mild
12	Opera House in Copenhagen	Copenhagen, Denmark	Cfb, Oceanic climate	Mild
13	BMW World	Munich, Germany	Cfb, Oceanic climate	Mild
14	Balanced Office Building	Aachen, Germany	Cfb, Oceanic climate	Mild
15	Viborg Town Hall	Viborg_Denmark	Cfb, Oceanic climate	Mild
16	Klarchek Information Commons	Chicago, Illinois, USA	Dfa, Humid continental climate	Warm and often humid
17	Crown Hall	Chicago, Illinois, USA	Dfa, Humid continental climate	Warm and often humid
18	Cooper Union New York	Manhattan, New York, USA	Dfa, Humid continental climate	Warm and often humid
19	Kripalu Housing Tower	Stockbridge, Massachusetts, USA	Dfb, Humid continental climate	Warm and often humid
20	The Terrence Donnelly Center	Toronto, Canada	Dfb, Humid continental climate	Warm and often humid
21	Dockland Offices	Hamburg, Germany	Dfb, Humid continental climate	Warm and often humid
22	Berliner Bogen Offices	Hamburg, Germany	Dfb, Humid continental climate	Warm and often humid
23	Mercedes World	Berlin, Germany	Dfb, Humid continental climate	Warm and often humid
24	Linked Hybrid	Beijing, China	Dwa, Humid continental climate	Hot and often humid

When the interstitial moisture cannot escape from the building construction layers and accumulates, moisture starts to condense and can cause moisture-related problems, including corrosion of the building fabric, deterioration of insulation, etc. [16]. Mold is the most critical of these problems (Figure 10). Based on [17], under ideal conditions (optimal temperature and level of humidity), it takes 24 to 48 hours for mold to germinate and grow [18]. Suppose this mold growth continues for a certain period. In that case, the building construction layers will decay, or

in some cases, the mold can extend to interior surfaces, which can lead to occupants' health problems, such as allergic rhinitis. This potential risk of developing surface condensation keeps thermo-active building systems (TABS) from being applied in buildings located in partly warm and humid climate regions.

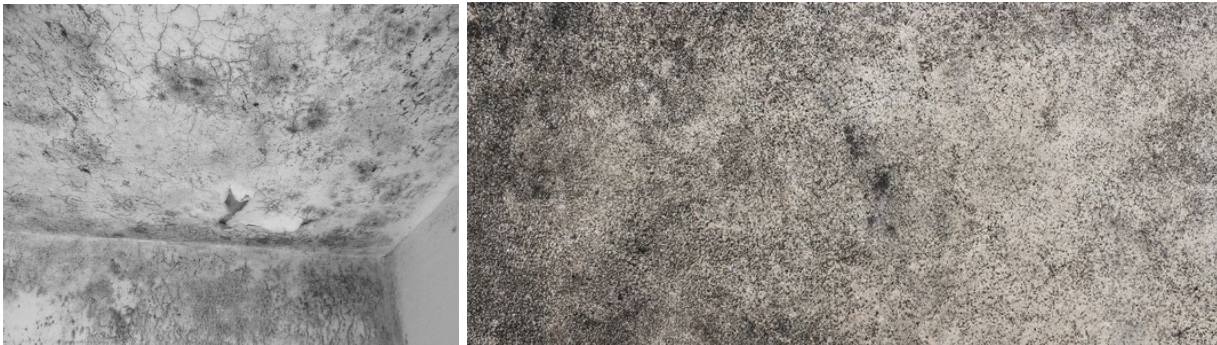


Figure 10. The condensation occurrence and the resultant mold growth on the concrete surfaces

To sum up, a thermo-active buildings system (TABS), one of the surface radiant cooling systems, is a promising cooling technology in reducing energy demand and providing better thermal comfort for occupants, but the potential risk of developing surface condensation on the TABS surface has kept the system to be applied widely under partly warm and humid climatic regions. Without solving the potential risk of developing surface condensation on the TABS, designers and planners will hesitate to choose the TABS as a major cooling system for their projects.

In the following section, literature review will be addressed how researchers have explored ways to predict, prevent, and control risk of developing surface condensation within construction layers. Also, a promising approach to prevent the risk of surface condensation is addressed and proposed in this study.

CHAPTER 2. Literature Review

2.1. Moisture Movement in Building Construction Layers

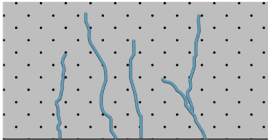
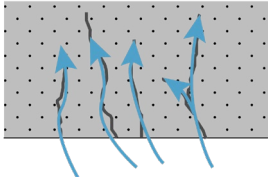
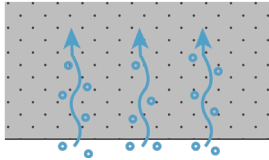
While controlling heat transfer through the building envelopes has been the primary concern for reducing building energy demand over the past few decades, a moisture-driven problem within the building construction layers has relatively less been considered [19]. The source of this problem is that as designers target increase insulation of the building envelope walls to achieve higher thermal resistance, there will be an increased temperature differential between the inner and outer portions of the walls; depending on the climate, the inner portion of the wall may get warmer but, at the same time, the outer part will get much colder, or vice versa [20]. Temperature differences in these walls affect the flow and redistribution of moisture in the wall, a moisture transport process in both vapor and liquid phases, which can lead to interstitial condensation. Thus, special care and attention are required when designers select material and control layers in envelope systems.

There are mainly four moisture movement mechanisms where the surface condensation development can damage building construction layers: 1) liquid flow caused by gravity or an air pressure difference, 2) capillary suction through porous materials, 3) air movement, and 4) vapor diffusion. Any moisture-related problem is a result of one or a combination of the above four mechanisms. The liquid flow is responsible for moving moisture into the building construction layers from the exterior caused by gravity or an air pressure difference. Capillary suction is a combined effect from the pore size in building construction layers and condensation existence

nearby. If the pore size in the construction layers is small enough, like concrete material, the capillary suction effect can be significant. The moisture can also penetrate the construction layers via air movement. When a crack or gap exists in the construction layers, the air can bring moisture deep into the layers, which can cause severe damage to the construction material. Vapor diffusion is the moisture movement in the vapor state through construction layers. This process is driven by a function of the vapor permeability of material and the vapor pressure differential imposed across the construction layers. During the vapor diffusion process, once the air's partial vapor pressure reaches the saturation level or the surface temperature reaches the dew point temperature, moisture starts to condense on the construction layers.

Considering TABS is generally installed on the ceiling side, not on the exterior construction layers, the mechanism of liquid flow caused by gravity or an air pressure difference can be neglected for surface condensation problems of the TABS. Therefore, capillary suction through porous materials, air movement, and vapor diffusion are the three mechanisms of moisture movement that need to be controlled to prevent surface condensation while the TABS is in operation.

Table 4. Three mechanisms of moisture movement can occur while TABS operation

Moisture transfer pathways	Description
Capillary suction	
	Capillary suction is a combined effect from the pore size in building construction layers and condensation existence nearby. If the pore size in the construction layers is small, like concrete material, the capillary suction effect can be significant.
Air movement	
	The moisture can also penetrate the construction layers via air movement. When a crack or gap exists in the construction layers, the air can bring moisture deep into the layers, which can cause severe damage to the construction material.
Vapor diffusion	
	Vapor diffusion is the movement of moisture in the vapor state through construction layers.

Capillary suction moves moisture into porous materials mainly. If pore size in a material is small enough (e.g., concrete, silty clay, etc.), the capillary suction occurs. Capillary suction does not happen in the material without pores (e.g., glass, steel, plastics, etc.). Capillary suction can be extremely critical where the building construction layers are below grade.

In general, the capillary suction can be controlled by blocking the capillary moisture or selecting the pore size of the building construction materials carefully. Capillary suction can also be prevented by sealing the connections between materials using caulking joints or providing the links wide enough not to bring capillary effect. Also, a receptor for capillary moisture can be delivered to prevent the capillary suction.

Air movement mechanism can transport moisture into building construction layers both from the conditioned space and the exterior. Following three conditions should be met to bring moisture into the building construction layers with air movement mechanism: 1) moist air should exist, 2) a gap or an opening exists in the building construction layers, and 3) an air pressure difference occurs across the hole or space in the building construction layers.

Even if the moisture enters the building construction layers, it does not necessarily deposit along with the building construction layers; the air movement's velocity should be slow enough for the moist air to be cooled down to the dew point temperature turn leads to the surface condensation development. Otherwise, the fast-flowing moist air can be maintained above the dew point. Making the building envelope airtight is one of the most effective strategies to deal with moisture transfer through air movement mechanism.

Vapor diffusion is the moisture movement process in the vapor state through materials. As far as the vapor pressure difference exists between two spaces, the vapor diffusion occurs. In a cold climate where a building is mainly heated, vapor diffusion typically moves moisture from the conditioned room into building construction layers. In contrast, in warm weather, the vapor diffusion naturally moves water from the exterior into the building construction layers.

The vapor diffusion mechanism can be controlled by installing the vapor retarders in the interior side of building construction layers in cold climates. In contrast, the instrument can be controlled by installing the vapor retarders on the exterior side of building construction layers in warm temperatures.

Considering these three potential moisture transfer pathways together, the amount of moisture transferred from the indoor space or the exterior into the building construction layers can be computed, thus enabling the prediction in the surface condensation occurrence. With this

information, the potential risk of developing surface condensation needs to be controlled to prevent the construction material's damage.

2.2. Surface Condensation Control with a Vapor Retarder

Attempts to introduce vapor retarders for preventing interstitial condensation were not expected until the 2000s. In the 1940s, polyethylene sheets were first introduced to control the vapor diffusion from interior space into building construction layers [19]. Then, in 2003, as part of its extensive proposal to the International Energy Conservation Code (IECC), the U.S. Department of Energy proposed vapor retarder recommendation based on the IECC climate zones classification [21] as a significant solution for interstitial condensation problems,

The IECC climate zones are classified with similar climatic conditions within the U.S., based on the massive database (e.g., heating degree days, cooling degree days, and wet-bulb temperature) that have been collected over the past few decades. Each zone has a number, starting from climate zone 1 for the hottest climatic region to climate zone 8, the U.S.'s coldest areas. Each numbered zone is then subdivided into A (Moist), B (Dry), and C (Marine), which specifies the humidity level of the climate zone (Figure 11). The IECC climate zones have been the significant climate zone classifications for the U.S. building code that have been used by local jurisdictions, and ASHRAE has developed several standards. The vapor retarder recommendation was also developed in alignment with the effort to establish the guidelines to control heat transfer through building envelopes because there was a hope that the IECC climate zones classification could also be used as the basis for measures designed to prevent the vapor moisture transfer through building envelopes, even though the bulk of the data were not explicitly related to moisture transfer.

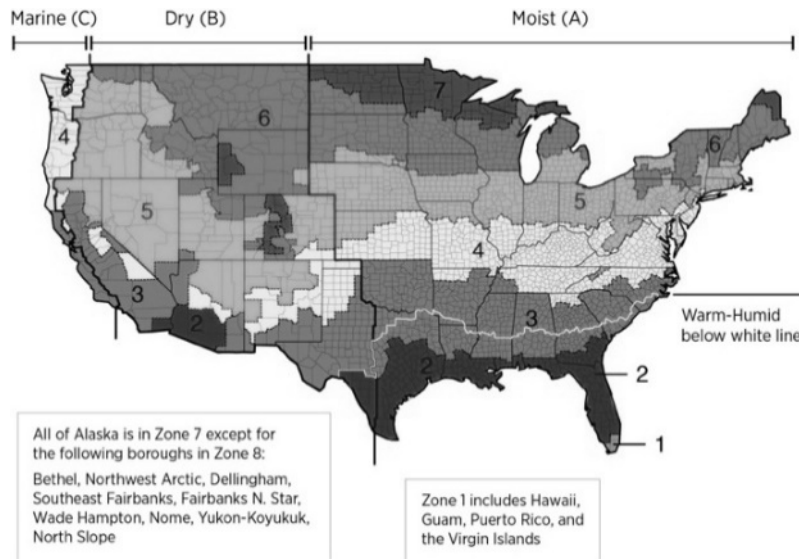


Figure 11. IECC climate zone map

Table 5. Vapor retarder classifications

Class	Vapor permeance level [$\text{kg}/\text{m}^2 \text{ s Pa}$]
Class I	Vapor permeance $\leq 5.7 \times 10^{-12}$
Class II	$5.7 \times 10^{-12} < \text{Vapor permeance} \leq 5.7 \times 10^{-11}$
Class III	$5.7 \times 10^{-11} < \text{Vapor permeance} \leq 5.7 \times 10^{-10}$

The basic principle of the vapor retarder recommendation was blocking warm and humid air penetrating building envelopes while allowing the moisture to escape through the opposite side of building envelopes to keep dry conditions of the building envelopes. The vapor retarder classes are determined depending on the vapor permeance level, which specifies the vapor diffusion permeability through porous materials (Table 5). Table 6 shows the vapor retarder class recommendation depending on the IECC climate zones. Because the moisture-driven problems

mainly occur in the Moist (A) and the Marine (C) zones, Dry (B) zones are not considered in the vapor retarder recommendation. For the climate zones 1-2 and climate zones 6-8, where the outdoor temperature is either extremely hot or cold, there was a consensus that climate zones 1-2 (hot) do not require vapor retarder (to avoid vapor trapped in building envelopes) while climate zone 6-8 involves vapor retarders in the inner side of the insulation to prevent interstitial condensation. However, regarding the intermediate climate zones, including zones 3, 4, and 5, seasonal temperature variability is more extensive than in climate zones 1-2 and zones 6-8; the vapor retarder recommendation derived from the IECC zone caused controversy among designers and builders. Some building industry segments criticized it because there was insufficient evidence to justify the request for vapor retarder guidance built based on the IECC climate zone classification, especially for the intermediate climate zones (Zone 3 through Zone 5) [19]. Because of this inconsistency, some states did not require vapor retarder recommendations as to the building codes.

To establish evidence to support the IECC vapor retarder recommendation with scientific data, in 2007, Karagiozis et al. explored the moisture risk prevention effects of vapor retarder choices in timber constructions of the zones by conducting massive heat and moisture (hygrothermal) transfer simulations [19]. The work of Karagiozis et al. presented quantitative analysis and documentation that present vapor retarder options for a selected number of wall systems depending on climatic zones in the U.S. Later, in 2015, the International Code Council published a vapor retarder recommendation amended from the former (2003) version [22].

Table 6. Vapor retarder code recommendations from International Residential Code

Climate zone	International Residential Code interior vapor retarder recommendations
Marine 4	Class I or Class II required; Class III permitted with: Vented cladding (over wood structural panels, fiberboard, or gypsum) or continuous insulation (U-value ≤ 2.27 W/m ² K over 0.05 m \times 0.1 m wall or U-value ≤ 1.51 W/m ² K over 0.05 m \times 0.15 m wall)
5	Class I or Class II required; Class III permitted with: Vented cladding (over wood structural panels, fiberboard, or gypsum) or continuous insulation (U-value ≤ 1.14 W/m ² K over 0.05 m \times 0.1 m wall or U-value ≤ 0.76 W/m ² K over 0.05 m \times 0.15 m wall)
6	Class I or Class II required; Class III permitted with: Vented cladding (over fiberboard or gypsum) or continuous insulation (U-value ≤ 0.76 W/m ² K over 0.05 m \times 0.1 m wall or U-value ≤ 0.50 W/m ² K over 0.05 m \times 0.15 m wall)
7 and 8	Class I or Class II required; Class III permitted with: Continuous insulation (U-value ≤ 0.57 W/m ² K over 0.05 m \times 0.1 m wall or U-value ≤ 0.38 W/m ² K over 0.05 m \times 0.15 m wall)
Others	Vapor retarders are not required

Besides the vapor retarder design recommendation, several researchers have explored interstitial moisture risk throughout the building construction layers. Toman et al. compared the hygrothermal performance of a masonry house before and after renovating the building and adding vapor-resisting features [23]. Four years of the experimental data were utilized for moisture risk estimation, and the result showed that interstitial condensation was not observed during the whole experiment period. Langmans et al. conducted short-term laboratory experiments to study the hygrothermal behavior of light-weight timber walls with an exterior vapor retarder [24]. The experiments' parameters included exterior vapor retarder, airtightness, moisture buffer capacity, vapor permeability, and thermal resistance. They found that using an exterior vapor retarder instead of an interior one may increase the moisture risk at the upper area of the façade as a result of

buoyancy-driven convection. Hansen et al. explored the differences in hygrothermal behavior depending on the masonry wall's position along with the building [25]. Each part's moisture risk was assessed by six months' worth of measured data with the VTT mold index model developed in [26]. Vereecken et al. adopted a probabilistic approach to estimate moisture risk for masonry construction with rigid insulation [27]. To determine the effect of the thickness of the insulation on vapor permeability, sets of rigid insulation with varied thicknesses were tested under stipulated vapor diffusion conditions. The results revealed that the moisture risk increased as the rigid insulation became thicker. Pasztory et al. compared hygrothermal performance and annual moisture risk between typical North American standard timber construction and the generally stricter European traditional timber construction [28]. Although the European standard timber constructions show better thermal performance than North American standard timber construction, buildings constructed under European standards can be more vulnerable to mold growth and fungal decay due to water deposits within the thicker rigid insulation layers. Chang et al. explored how moisture risk changed when cross-laminated timber (CLT) construction was added on top of the typical timber construction [29]. They conducted chamber tests to figure out the hygrothermal performance of CLT and for validation. The Lowest Isopleth for Mold (LIM) curve method introduced in [30] was adopted for moisture risk assessment. They concluded that when assuming CLT walls in Korean climatic conditions, the type of insulation material, hygrothermal performance, and climate conditions should be considered to reduce the interstitial moisture risk.

To summarize, most interstitial moisture risk studies were conducted for at least a half-year period to reflect the effect of seasonal climatic condition changes on the interstitial moisture risks. Regardless of construction material (e.g., timber construction, masonry construction, etc.), vapor retarders were generally installed on the interior side (inner side of the insulation) rather than the

exterior side to prevent indoor-produced moisture from penetrating the insulation layer. Among several insulation types, rigid insulation and fiberglass insulation were tested the most frequently in the moisture risk studies; rigid insulations represent an insulation type with a low vapor permeability level, while fiberglass insulations represent insulation with a high vapor permeability level. In most cases, sheathing boundary layers (between sheathing material and insulation) show the highest risk of developing interstitial condensation across building wall layers regardless of the types and thickness of materials used.

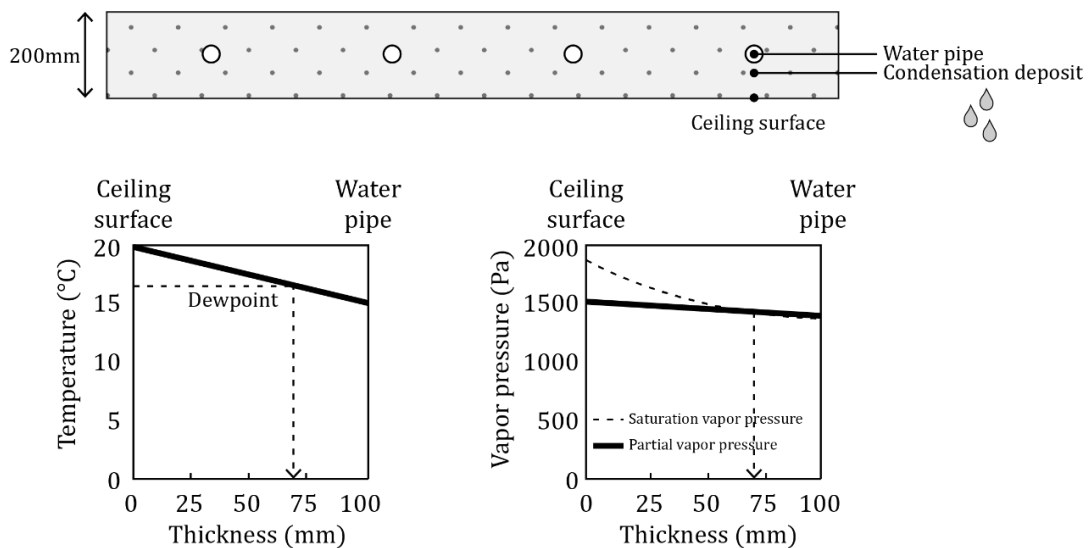


Figure 12. Dew point/temperature curve and saturation/partial vapor pressure curve in TABS

2.3 Surface Condensation Prediction Models

Since the 1930s, several studies have explored ways to predict heat and moisture (hygrothermal) transfer in building construction layers. Rodgers [31] was the first to study vapor pressure as a driving potential for moisture transfer. In the study, Rodgers presented the vapor pressure curves method, which shows the relative partial vapor pressure level across building construction layers. Rowley et al. [32, 33] then refined existing work into the prevailing theory of

vapor diffusion models by adopting heat conduction principles. Vos and Coleman [34] further developed the models by testing the combined effect of vapor diffusion and capillary suction on moisture transfer. Künzle and Grosskinsky [35] identified air transport as an additional driving potential for moisture transfer. The Luikov model [36] and the Philip and de Vries model [37] are the most widely used hygrothermal transfer models; these adopt the temperature and the moisture content as driving potentials. However, taking the moisture content as the moisture transfer potential sometimes makes the models challenging because the moisture content level is not always continuous across the building construction layers [38]. Y. Liu et al. [39] proposed the constant relative humidity instead of the moisture content as the driving potential for moisture transfer to deal with this problem. With these modifications, the researchers have developed the hygrothermal transfer models in a way that incorporates the three hygrothermal pathways in building construction layers while simplifying the solution for the models by adopting continuous parameters. The results provided by the models predict short-term condensation with reasonable accuracy in building construction layers.

Table 7. Summary of literature review in heat and moisture transfer models

References	Main findings
Rodgers [31]	Vapor pressure was studied as a driving potential for moisture transfer. The vapor pressure curves method was presented, which shows the relative partial vapor pressure level across building construction layers
Rowley et al., [32,33]	The theory of vapor diffusion models was refined by adopting the principles of heat conduction
Vos and Coleman [34]	By testing the combined effect of vapor diffusion and capillary suction on moisture transfer, the heat and moisture transfer models were further improved
Künzel and Grosskinsky [35]	Identified air transport as an additional driving potential for moisture transfer
Luikov [36] and Philip and de Vries [37]	The temperature and the moisture content were adopted as driving potentials for the heat and moisture transfer
Y. Liu et al. [39]	The continuous relative humidity was adopted as the driving potential for moisture transfer

Despite their usefulness, these models are not directly applicable for controlling surface condensation for two reasons. First, a short-term condensation prediction from the model is inadequate for dealing with dynamic indoor conditions changes. Indoor conditions do not remain stable but fluctuate according to daily weather changes [40]. Because of this fluctuation in indoor situations, the probability of surface condensation sometimes can increase rapidly, which in turn can lead to a sudden occurrence of surface condensation, even though the model has calculated the ongoing probability. Second, the model's short-term condensation estimation can sometimes cause severe estimation errors for buildings with heavy construction materials like concrete. The hygrothermal transfer rate of building construction layers is delayed significantly due to the construction materials' high density and capacity; this time-delay can sometimes extend up to almost half a day. Because of unreliable condensation prediction caused by the slow and gradual hygrothermal transfer in heavy construction materials, direct application of these models can be insufficient for enabling a system to control the surface condensation.

Therefore, given the daily fluctuation in indoor conditions and the time-delay in the hygrothermal response of heavy concrete materials, an estimation that anticipates the surface condensation at least one day ahead is required for effective surface condensation control. With a day-ahead assessment, both the indoor condition changes and the time-delay in the hygrothermal transfer can be considered together in advance, providing more accurate condensation prediction for the system to make a better decision.

2.4. Control Methods for HVAC Systems

When the following day's surface condensation prediction is provided, the control methods can determine control input (supply water temperature and flow rate) for the TABS that assures indoor thermal comfort and energy efficiency. Based on [41], several control method options are available for the controlled cooling system (Figure 13).

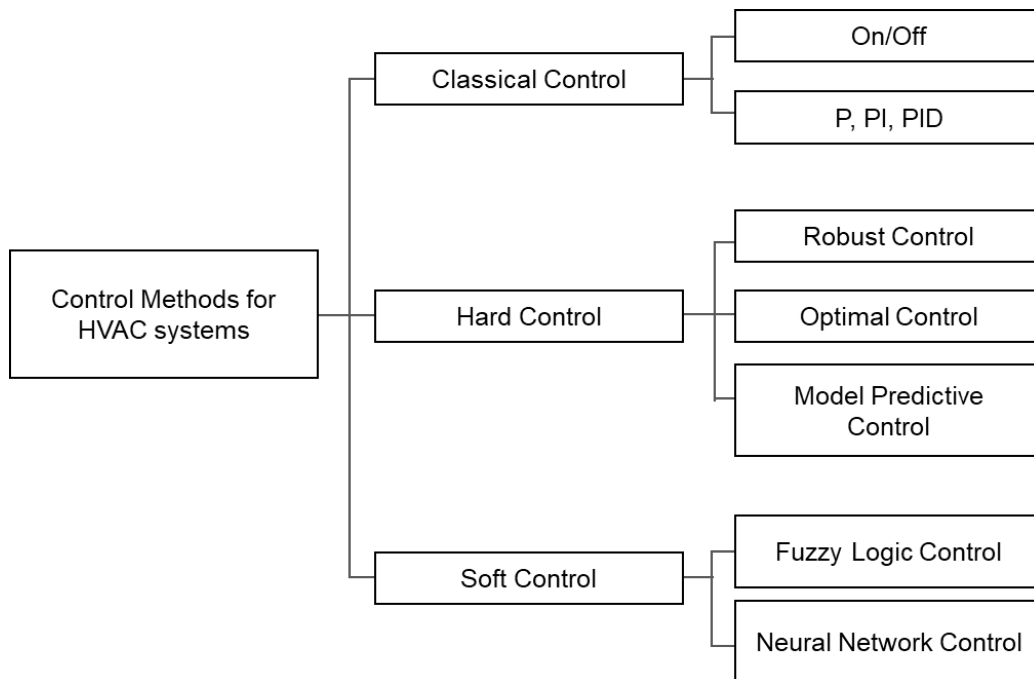


Figure 13. Classification of control methods for HVAC systems

Classical controllers consist of conventional control techniques, such as on/off control and P, PI, and PID control. The on/off controller uses an upper and lower threshold to govern the given threshold process. Although the on/off controller is the most straightforward approach to implement, it is unsuitable for dealing with time delays. The P, PI, and PID controllers use error penalization and regulate the control to achieve accurate control goals. The PID controller produces promising results, but tuning the controller parameters is cumbersome, and the

performance of the controller degrades if the operating conditions vary from the tuning conditions. Re-tuning or auto-tuning approaches for the PID controller [42] can be time-consuming. In certain applications, auto-tuning might be unacceptable because of its intrusive nature relative to normal operation [43]. Because of the high thermal inertia of TABS processes, a controlled process using an on/off controller or PID controller shows large fluctuation from the control threshold. Thus, despite their simplicity, both control methods are unsuitable for anticipatory condensation control because they use only current and previous states as the basis for system control [41].

On the other hand, soft control techniques, including fuzzy logic control and artificial neural network (ANN) control, are relatively new techniques that have been applicable after the advancement of digital controllers. In a fuzzy logic controller, control actions are implemented in the Boolean logic statements. The fuzzy logic can also be incorporated for the auto-tuning of PID controller gains where PID control represents the local control, and the fuzzy logic supervisor is often used to optimize the response of the system on the global scale. The fuzzy logic supervisor also acts as an arbiter and resolves conflicting objectives from the local level controllers by prioritizing certain controllers over others based on the common goals of reduction in energy and maintenance of thermal comfort. Alternatively, the fuzzy logic can be implemented on both the local and supervisory level of control.

The ANN, on the other hand, is built based on the measured data sets with the training process and fits a nonlinear mathematical problem. The algorithm is a black box modeling technique that does not require an understanding of the phenomenon's underlying physics. However, ANN-based control requires massive training data sets covering a wide range of operation conditions, making the approach time-consuming.

The implementation the fuzzy logic control requires comprehensive knowledge of the plant operation and its different states, whereas ANN-based control requires training data on a wide range of operating conditions, which may not be available for many systems. Additionally, industry is usually reluctant to adopt and use a black box approach.

Hard controllers are based on a theory for control systems that consist of gain scheduling control, nonlinear control, robust control, optimal control, and model predictive control (MPC). In gain scheduling control, a nonlinear system is divided into many pieces of linear parts. For each of the linear functions, a linear PI or PID controller is adopted with different approaches. Self-tuning PI or PID controllers are also presented in the literature to differentiate the controller gains based on the state of the process [44]. The control algorithm is derived from Lyapunov's stability theory, feedback linearization, and adaptive control for nonlinear controller design. The control algorithm is designed to deal with the nonlinear system while achieving the control objectives [45]. The purpose of robust control is to create a control algorithm that works under dynamic disturbances and changes within parameters [46]. The optimal control algorithm solves an optimization problem to satisfy a specific objective function. The systems' objectives are, in general, optimization between energy consumption reduction, control effort minimization, and thermal comfort satisfaction.

The nonlinear control techniques are effective but require the identification of stable states and complex mathematical analysis for controller design. For gain scheduling control design, the identification of linear regions and design of switching logic between regions is necessary, and the manual tuning of multiple PID controllers in these regions can be quite cumbersome. Optimal control and robust control are promising techniques for HVAC process control because they are capable of rejecting disturbances and time-varying parameters. In general, robustness is difficult

to guarantee in HVAC systems, which are subject to varying conditions in buildings. Many of these approaches also require the specification of additional parameters, which could be difficult and impractical for integration in HVAC systems.

A promising approach for surface condensation control is model predictive control (MPC) among the rigid control approaches. In contrast to other controllers, MPC determines the input signal for the system not based on just the current states but also on the impact the actions will have on the future conditions (Figure 14). Because MPC considers both current states and future states, it is suitable for anticipatory surface condensation control capable of dealing with dynamic indoor condition changes and the time-delay in hygrothermal transfer in advance.

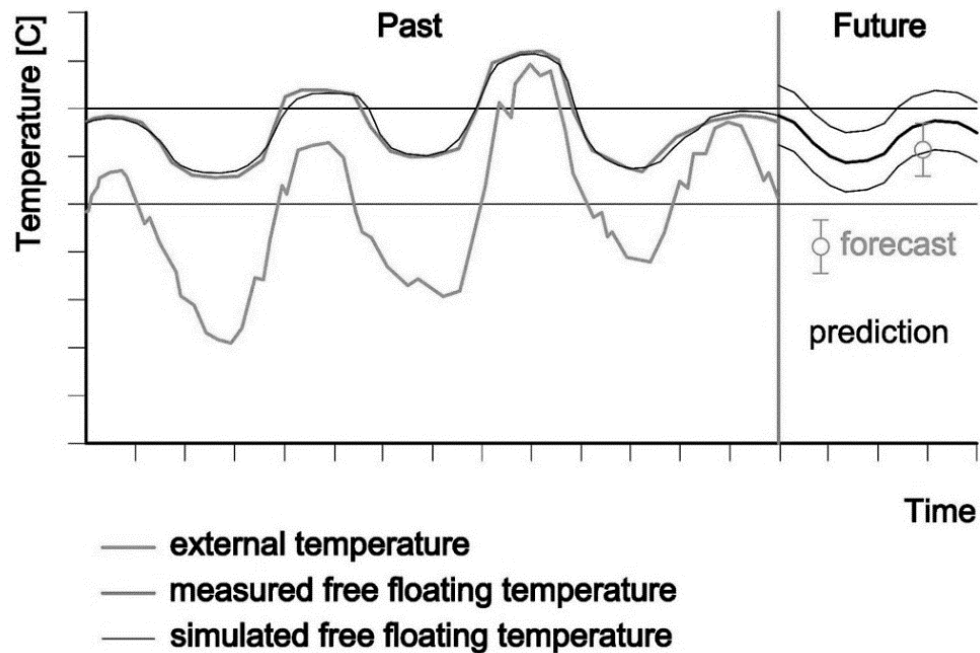


Figure 14. Schematic diagram of predictive model control for indoor temperature

2.5. Basics of Classical Model Predictive Control

The classical objective function utilized by the MPC is given as [47]:

$$J(t_k) = \sum_{i=N_1}^{N_y} \omega_y(i) [\hat{y}(t_k + i) - y_{set}(t_k + i)]^2 + \sum_{i=1}^{N_u} \omega_u(i) [u(t_k + i) - u(t_k + i - 1)]^2 \quad (1)$$

where t_k = control time-step, y_{set} = set point, \hat{y} = predicted output, u = command effort,

N_y = the prediction horizon where the output error $\hat{y} - y_{set}$ is minimized,

N_u = the control horizon where the command effort increment is minimized.

ω_y = weighting factor for prediction error

ω_u = weighting factor for command effort

In classical MPC applications, a relatively short-term control horizon (< 1hour) is preferred to deal with dynamic changes in the systems [48]. However, the short-term control horizon is not suitable for the surface condensation control because hygrothermal transfer through the construction layers is much slower and gradual. Instead, a longer control horizon is essential to deal with both the time-delay in hygrothermal transfer and the indoor condition changes in advance.

An initial application of the MPC started in the late 1970s in the process industries in chemical plants and oil refineries [49]. Since then, the MPC has been adopted in autoclave composite processing, wastewater treatment, automotive industry, etc. In autoclave composite processing, the MPC is assumed to define an optimal input to determine a bagging procedure and a cure cycle that assures a cost efficiency [50]. For the wastewater treatment process, input parameters of aeration rate, dilution rate, and recycled ratio are adjusted to achieve a specific concentration level of dissolved oxygen by repeatedly rejecting the water's substrate concentration [50].

Recently, MPC has been studied widely in the built environment because of significant time and cost reduction in the data processing. The majority of MPC research is primarily focused on HVAC system control [51-54], building thermal behavior predictions [55, 56], or indoor thermal comfort control [57-59]. However, to the best of the author's knowledge, there are few studies in which MPC was applied for controlling the surface condensation on building construction layers.

2.6. Model Predictive Control for Surface Condensation

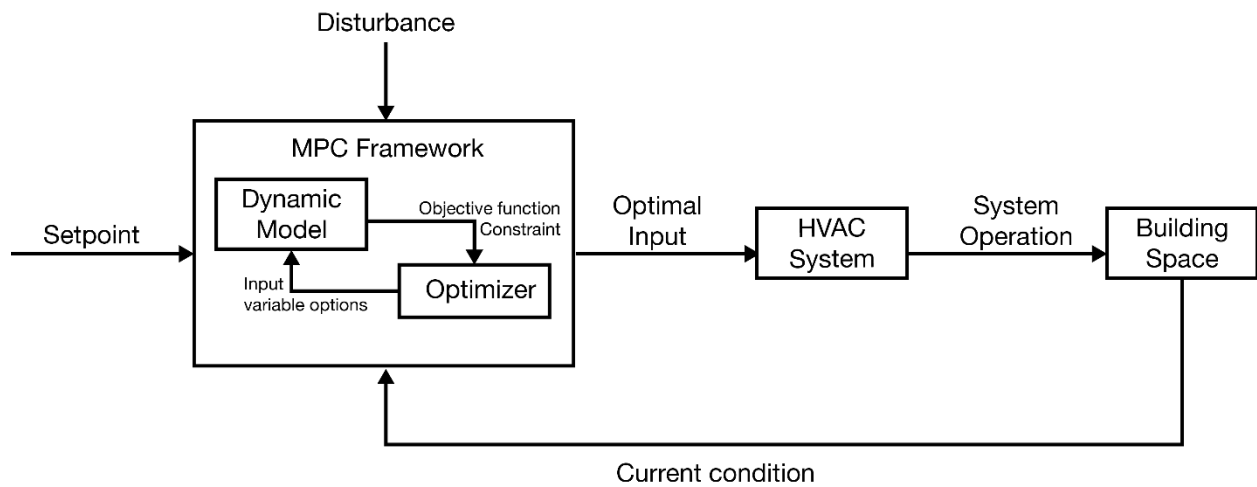


Figure 15. The basic framework of model predictive Control for HVAC systems

The basic framework of MPC for HVAC systems is shown in Figure 15. It is a closed-loop cycle consisting of a dynamic model and optimizer [60]. The dynamic model simulates several potential future states using adjustments in the control inputs. The best control input that minimizes an objective function without penalizing the constraints is found using the optimizer [61]. When

the best control input is determined, it is fed back into the HVAC system operation. This process is repeated for every control horizon [16].

The MPC objective function that ensures thermal comfort with minimum cooling energy is [47]:

$$\text{minimize: } J(t_k) = \sum_{i=1}^{N_u} u(t_k + i) \quad \text{Objective function (2)}$$

$$\text{subject to: } 0 \leq u(t_k + i) \leq u_{max}, \quad i = 1 \dots N_u \quad \text{Constraints}$$

$$\hat{y}(t_k + i|t_k) \leq y_{max}(t_k + i), \quad i = 1 \dots N_y$$

where, t_k = control time-steps, N_u = the number of steps in the future horizon, $u(t)$ = system inputs, u_{max} = the maximum cooling system input, $\hat{y}(t)$ = system outputs, and $y_{max}(t)$ = upper indoor temperature threshold for thermal comfort.

After the dynamic model predicts several potential future states, MPC determines the best control scenario under the objective function and the constraints [62]. At every control time-step, the control problem for MPC is formulated and solved to meet the objective without violating the control horizon's restrictions. When the best control input is determined under the control horizon, the best control input is fed back into the system operation and moves forward to the next control time-step.

2.7. Dynamic Modeling for Model Predictive Control

A dynamic model that enables future state prediction is an essential part of MPC [60]. The dynamic models simulate several potential future states using adjustments in the control inputs, and the best control scenario is chosen from these predictions [61]. Because numerous simulations

need to be done within a limited time frame, relatively fast and sturdy dynamic models are preferred in the MPC framework [47].

ASHRAE [6] classifies two major dynamic modeling approaches based on how the model has been built: a forward model and a data-driven model. The forward modeling approach, also known as the white box model (or theoretical model), is made based on the phenomenon's detailed physical knowledge. In contrast, the data-driven modeling approach is built based on the measured data. The data-driven modeling approach is useful when there are disturbances that are inexplicable with the white box model. The data-driven modeling approach is further classified into black box models and grey box models, depending on the degree of the physical knowledge that has been adopted for the modeling process. The black box models are built based on massively collected data and do not require any biological understanding of the phenomenon.

On the other hand, the grey box models (or partial theoretical model) exploit advantages of both the white box model and the black box models, the sturdiness of white box models, and the black box models' speediness [63]. The grey box models (partial theoretical models) adopt a lumped parameter approach (e.g., Resistance-Capacitance model) as the models' main structure. Unknown parameter values in the model are found in the model calibration method, like curve fitting. Table 8 compares basic features of dynamic modeling types for MPC.

Table 8. Comparison of dynamic modeling approaches for MPC

	Theoretical model (white box model)	Data-driven model (black box model)	Partial theoretical model (grey box model)
Requires theoretical knowledge	Detailed	No	Partly
Requires numerous data sets	No	Numerous	Partly
Calibration process	Lengthy	Very fast	Fast
Flexibility	Less flexible to non-existing knowledge	Flexible to uncertainties	Can be improve by model calibration process

2.7.1 Theoretical Model (White Box Model)

The theoretical models are built based on the detailed physical knowledge of the phenomenon. Because the theoretical models are created based on a physical numerical correlation between various physical interactions, the building scientists and engineers consider the theoretical models to be the most reliable dynamic modeling approach. However, when some disturbances or noises are inexplicable with the physical knowledge, the accuracy of the theoretical model's results will suffer significantly. Furthermore, the theoretical model's lengthy calculation time makes it an unsuitable dynamic model type for the MPC.

2.7.2 Data-driven Model (Black Box Model)

The data-driven models can help to solve more complicated problems without knowing any physical background of the phenomenon. The data-driven models have been built based on the pairs of inputs and outputs of gathered data. When these data are put into the learning algorithm, specific correlations are found that can produce the desired outcome from the information.

However, the prediction accuracy of the data-driven model highly depends on the quantity and quality of the collected data.

There are several data-driven modeling approaches available for MPC framework development. A K-nearest neighbor (KNN) algorithm is suitable when you only have small data sets. It is easy to understand, fast, and showing a good performance without adjustments. However, the KNN does not perform well on the data with too many features. For data sets with many features, a linear model can be a solution. The linear model is high-speed for training the dynamic model. However, it is often unclear why coefficients are the way they are, and hard to interpret the coefficients. Decision trees are a widely used data-driven modeling approach.

They learn a hierarchy of the Boolean logic questions, and the decision is made based on the system's learning. The decision tree can easily visualize how they derive the prediction, and the algorithms are entirely invariant for scaling the data. However, they tend to over-fit and provide poor generalization performance. A random forest is ensembles of decision trees, where each tree is slightly different from the others. The main drawback of decision trees is that they tend to over-fit the training data. If we build many trees, all of which work well and over-fit in different ways, we can reduce the amount of overfitting by averaging their results. A support vector machine is a robust algorithm for medium-sized data sets of features with similar meaning. However, this approach requires scaling of data, and the performance is sensitive to parameters. An artificial neural network (ANN) is an algorithm that is inspired by the biological neural network. They mimic a human neuron system's learning ability. The networks adjust the weighting factors among the neurons to find correlations between input and output data sets from measured data. ANN can build very complex models, particularly for large data sets. Because the ANN is trained with numerous data sets, it takes a long time to make a model.

Numerous studies adopted the data-driven models as their primary dynamic modeling approach to predict indoor condition change. X. Xu et al., [64] developed a novel method to measure an evaporator's inlet humidity based on dry-bulb temperatures using the artificial neural network model (ANN) way helped to simplify and accelerate the complex derivation process. When compared to experimental results, the prediction errors were less than 5%. L. Mba et al. [65] applied the ANN for an advanced hourly prediction of indoor air temperature and relative humidity in buildings. The measured data from the hollow block experiments were used to construct and validate the ANN model. M. Taki et al. [66] compared the ANN model with the white box model to predict heat transfer accuracy through building envelopes. The results reveal that the ANN method is more accurate in predicting heat transfer in building envelopes than the white box model. H. Huang et al. [67] presented an ANN-based system identification method to model multi-zone buildings. The proposed model dealt with cooling, ventilation, dynamic weather change, and the convective heat transfer coefficient. The temperature measurements reveal that the proposed ANN model reflects the heat transfer behavior along the zones well, therefore achieving more accurate predictions than a single-zone model.

The data-driven models can further be utilized for predicting the energy demand of buildings. Y. T. Chae et al. [68] presented a data-driven forecasting model for day-ahead electricity usage of facilities. The model was built based on the ANN model with Bayesian regularization algorithm. The results demonstrate that the proposed model with adaptive training approaches can predict the energy consumption with 15 minutes time intervals and the daily peak energy usage well in a tested building. C. Deb et al. [69] presented a methodology to forecast diurnal cooling load energy consumption using data-driven ANN techniques. The results show that the ANN can

train and predict the next day's energy consumption based on five previous days' data with reasonable accuracy.

Advance in central processor led the data-driven models to be applicable in building system operations. J. W. Moon et al. [70] proposed an ANN-based thermal control method for double skin facade buildings. Considering the predicted future indoor air temperature, the control logic predetermines the double-skin façade system's operation action. G. Ge et al. [71] utilized the ANN model to predict condensation risk and the optimal pre-dehumidification time in chilled ceiling systems. Two ANN models were developed to predict the temperature on the surface of the chilled ceiling and indoor air dewpoint temperature at the startup moment to evaluate condensation risk. V. Congradac et al. [72] presented chillers operation optimization using the ANN and genetic algorithms. The ANN model was trained and validated with collected data from the actual chiller operation. Based on the results, the ANN model contributes to the electricity savings by 2% during summer days and up to 13% during the transition period.

In summary, the majority of studies in data-driven models utilized the Artificial Neural Network (ANN) approach as their primary learning algorithm. However, it should be noted that the accuracy of the data-driven models, including the ANN model, highly depends on the number and quality of collected data.

2.7.3 Partial Theoretical Model (Grey Box Model)

The grey box models (or partial theoretical models) are an alternative to the white box and the black box models. The partial theoretical models take advantage of both the sturdiness of white box models and the flexibility of black box models [63]. The partial theoretical models are built with the simplified or lumped parameters approach to representing the physical phenomenon

theoretically. Unknown parameter values are then found with the model calibration method, such as curve fitting. As presumed parameter values of the partial theoretical models reach actual parameter values, the model's prediction accuracy will increase.

The partial theoretical models offer relatively fast and robust calculations for predicting indoor condition change. Ion Hazyuk et al. [73] proposed a partial theoretical dynamic modeling approach consists of two stages: first, physical knowledge is used to determine the structure of a low-order model, then least squares identification method is adopted to find the parameter values. This approach allows the model to acquire desired input parameters and to eliminate disturbance sources. Thomas Berthou et al. [74] utilized a comparative design approach to find the best model structure and a suitable methodology for improving the partial theoretical models' prediction accuracy. Different forms for the partial theoretical models are compared in predicting indoor thermal behavior. B. Lehmann et al. [75] presented a resistance-capacitance (RC) building modeling approach adjusted for MPC. The model was found to show accurate results. Also, the proposed modeling approach can be flexibly restructured to represent various building types and active systems.

Moreover, the partial theoretical models can be utilized for optimizing energy usage in buildings. H. Burak Gunay et al., [76] explored the uncertainty introduced by an occupant's behavior. This effect was calculated using the lumped RC model. Results indicate that modest yet robust to occupant behavior, energy savings can be achieved by limiting the prediction time horizon to one hour in zone level MPC implementations. Choice of this prediction time horizon also eliminated the need for importing weather forecasts. Y. Zhao et al., [77] proposed a model predictive control (MPC)-based strategy using nonlinear programming (NLP) algorithm to optimize the scheduling of the energy systems under day-ahead electricity pricing. Results show

that the proposed optimal scheduling strategy can significantly reduce carbon dioxide emission, primary energy consumptions, and operation cost. M. Schmela et al. [78] presented a novel predictive method based on multiple linear regression (MLR), including a lumped RC model for TABS control. With the proposed method, no parameterization of curves is necessary, thanks to the self-learning process. The proposed predictive control strategy can save a pump-running time of up to 81% while increasing thermal comfort. R. De Coninck et al., [79] presented a model predictive control (MPC) applied in a medium-sized office building in Brussels, Belgium. The lumped RC model was used for building the MPC framework. The results show that the model predictive controller can provide a similar or better thermal comfort than the rule-based controller while reducing the energy costs by more than 30%.

In summary, it should be noted that the reduced-order RC models are the basic structure for the partial theoretical models. The key to success in the partial theoretical models depends on defining the calculations' required parameter values. The RC models need to be calibrated with the measured data; the most suitable parameter values are then derived from the calibrated results.

According to the literature review on the dynamic modeling approach, either data-driven models or partial theoretical models are mainly utilized to build dynamic modeling of MPC. The data-driven models are favorable when too complex physical phenomenon needs to be modeled or when disturbances are dominant in the prediction problems. Although the data-driven modeling approach can deal with both situations, massive data are essential to building a reliable model. On the other hand, the partial theoretical models are preferred when the lumped parameter models can predict general trends but need a model calibration with some measure data. The main advantage of the partial theoretical models is that they do not require massive data sets for model calibration. Also, the partial theoretical models are considered more sturdy than the data-driven models

because the basic structure of the partial theoretical model is broadly equivalent to that of the theoretical model.

2.8. Long-term Model Predictive Control

Depending on the length of the control horizon, MPC can be classified into short-term (0-1hour), mid-term (1hour-24hours), and long-term (24hours-) MPC [48]. As addressed in Section 2.3, most of classical MPC-related research is classified into short-term MPC with a shorter control horizon than an hour.

However, when it comes to the surface condensation control problem of the TABS, the short-term MPC cannot be utilized because the heat and moisture transfer rate of the building construction layers is delayed significantly due to the high density and capacity of the construction materials. Considering this slow and gradual hygrothermal response of the heavy concrete materials of the TABS, a relatively longer time-step and control horizon (compared to the short-term time-step and control horizon of the classical MPC) is essential to control surface condensation when the TABS is in operation.

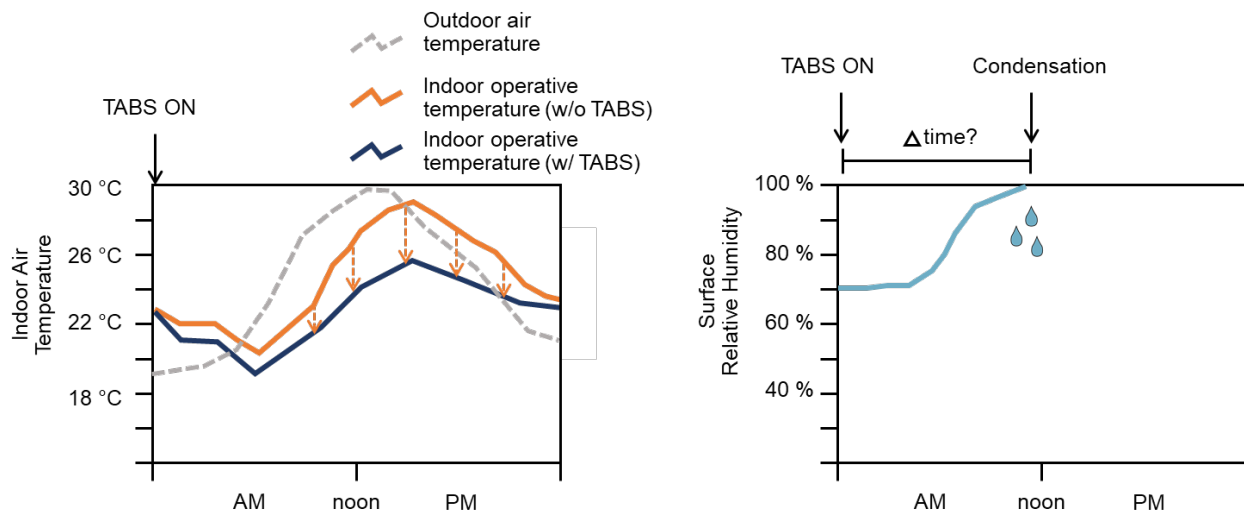


Figure 16. Slow and gradual hygrothermal response time of heavy construction layer

Thus, instead of utilizing the classical MPC that adopts short-term control time-steps, a long-term MPC framework is suitable for the surface condensation control problem. The more extended control time-steps for the MPC will allow the system to optimally operate the TABS without developing the surface condensation and causing too much fatigue. By controlling the potential risk of surface condensation development while the TABS is in operation, the operable periods of the TABS can be extended, which leads to the extended use of the TABS to an area in which climate conditions had made them infeasible.

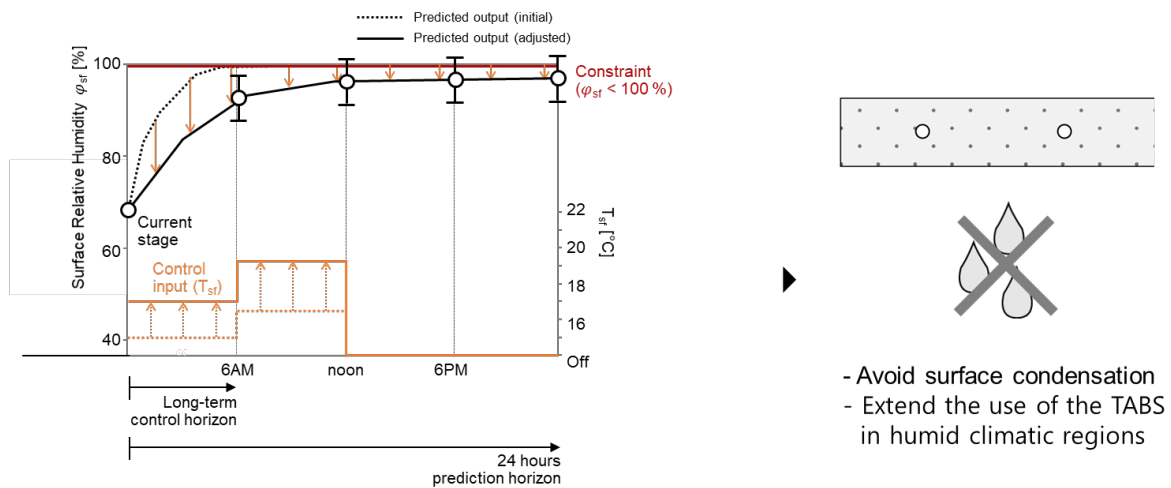


Figure 17. Surface condensation control with long-term MPC

Based on the above literature review, a model predictive control is one of the most promising approaches to deal with slow and gradual heat and moisture transfer through building construction layers which in turn leads to accurately predict and prevent the risk of developing the surface condensation on the TABS. A dynamic model which helps to predict future state is an essential part of MPC and three types of dynamic modeling approaches were identified. Among them, the partial theoretical modeling approach is most preferable because this approach does not require massive data for model calibration and is considered sturdy than the data-driven models.

Furthermore, regarding the length of control time horizon for the MPC, a relatively longer time-step and control horizon are essential to control surface condensation when the TABS is in operation.

CHAPTER 3. Research Purpose

To address above mentioned research problems and gaps, this dissertation study presents a novel MPC-based surface condensation prevention framework that permits extended use of the TABS operation even in warm and humid climate regions. The proposed MPC framework will thus achieve cooling energy savings by extending the operable periods for the TABS.

The dissertation's outline is as follows (Figure 18): in Chapter 4, the methodology of developing the MPC-based surface condensation prevention framework is addressed. In Chapter 5, the results from the calibrated dynamic model are discussed. Then, the MPC-based surface condensation prevention framework is developed using this calibrated dynamic model. Moreover, the applicability and the cooling energy savings potential of the MPC-based surface condensation prevention framework concerning the climate zones are discussed. Finally, Chapter 6 summarizes the conclusions.

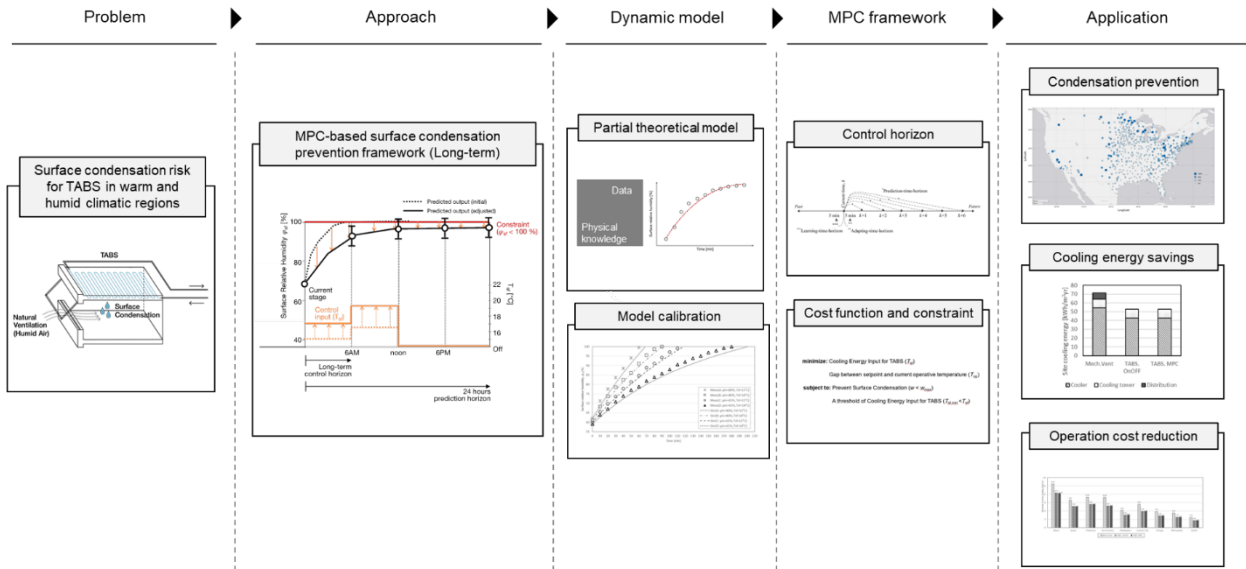


Figure 18. Outline of the dissertation

3.1. Research Question

This study will explore the following research questions:

- 1) How much can energy savings be achieved with TABS operation governed by the proposed MPC framework?
- 2) How accurate is the proposed MPC framework in preventing surface condensation when the TABS is in operation?
- 3) How well does the proposed MPC framework maintain the thermal satisfaction of occupants?
- 4) How can the proposed MPC framework broaden the TABS application even in warm and humid climate regions, especially in the US?
- 5) How does the broadened TABS application contribute to design practice in warm and humid climate regions?

3.2. Research Importance

Regardless of the dynamic modeling approach, the proposed MPC-based surface condensation prevention framework is expected to reduce the surface condensation occurrence risk even when the TABS is in operation under warm and humid climate regions. Thus, the proposed MPC framework will achieve cooling energy savings by extending the operable periods for the TABS.

Because the MPC framework will continually control the surface condensation when the TABS is in operation, the potential damage to the building construction layers like corrosion of the building fabric or deterioration of insulation can be avoided. With the avoidance of injuries in building envelopes, a repair cycle for each building construction layer will be extended, leading to the overall maintenance cost savings for building material.

Also, condensation-driven health problems like allergic rhinitis can be avoided by continuous surface condensation control by the MPC framework. The mold starts to grow in the building construction layers if condensation remains more than 24 hours under the 25°C condition [18]. With the one day ahead surface condensation prediction by the MPC framework, the potential risk of failing to detect surface condensation can be eliminated, contributing to complete avoidance of mold growth in building construction layers.

The proposed MPC-based surface condensation prevention framework will broaden the use of the TABS even in warm and humid climate regions. Based on the global radiant heating and cooling systems market reports, analysts forecast the global market for radiant cooling systems, including TABS, to grow at a compound annual growth rate of 7.14%, contributing to 1.63 billion dollars incremental growth during the period 2018-2022 [80]. Under the growing demand for the

TABS, the proposed MPC framework can enhance TABS applicability even in the humid area by controlling the potential risk of surface condensation development.

Furthermore, the broadened TABS application in warm and humid climate regions will allow more freedom in architectural design practice. As discussed in Section 1.2., many architects could have preserved the buildings' integrity or have maintained their initial design ideas thanks to the TABS. Without the TABS, Crown Hall's HVAC distribution system would have been exposed to the indoor space, which may not be a delightful situation for architectural aesthetic integrity.

In the following section, a step-by-step process of developing the MPC-based surface condensation prevention framework will be addressed.

CHAPTER 4. Methodology

An MPC-based surface condensation prevention framework was developed in the following order. First, the heat and moisture transfer dynamic model was built. Second, the progress of the surface condensation development on concrete material was tested in a chamber. Third, the hygrothermal transfer model was calibrated with the measured data and uncertain parameter values were derived from the calibrated model. Fourth, the MPC-based surface condensation prevention framework was developed based on the calibrated hygrothermal transfer model.

As shown in Figure 19, the proposed MPC-based surface condensation prevention framework will provide the right surface cooling temperature input for the TABS operation that maintains indoor thermal comfort and energy efficiency without developing the surface condensation even in warm and humid climate regions.

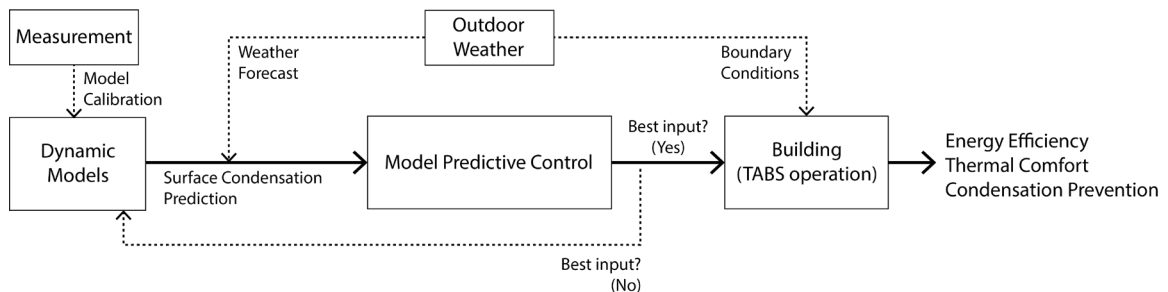


Figure 19. Overview of the proposed MPC-based TABS operation

After developing the MPC-based surface condensation prevention framework, the performances of preventing surface condensation while the TABS operation was estimated for each climatic site in the United States.

4.1. Dynamic Modeling with the Partial Theoretical Model

One of the main challenges in developing dynamic models is to find a suitable model type for a given MPC problem [79]. These models need to be accurate enough to achieve satisfactory hygrothermal behavior predictions. Simultaneously, the models need to be concise so that the MPC framework can test and run numerous potential control scenarios within a limited control horizon [80]. Thus, the partial theoretical model approach was adopted for the MPC framework development. The TABS performance governed by the process will be estimated in terms of condensation prevention, energy savings potential, maintaining thermal comfort, and calculation time.

For the partial theoretical modeling approach, two models need to be developed for surface condensation prediction: dynamic modeling of construction layers and buildings' dynamic modeling. The surface temperature was calculated with the heat transfer model, and the humidity level was calculated with the moisture transfer model. Coupling the heat transfer model and the moisture transfer model enables the surface condensation prediction.

4.1.1. Dynamic Modeling of Heat and Moisture Transfer in Building Construction

Fourier's law is a basis for the heat transfer model, while Fick's law and Darcy's Law are used for the moisture transfer model and liquid flow model, respectively [81].

Fourier's law (for heat transfer):

$$\dot{q} = -k \frac{\partial T}{\partial x} \quad (3)$$

where \dot{q} is the heat flux, k is the thermal conductivity of the material, T is temperature, and x is the length of material.

Fick's law (for vapor diffusion):

$$\dot{m}_v = -\mu \frac{\partial P_v}{\partial x} \quad (4)$$

where \dot{m}_v is the mass flux for vapor, μ is the vapor permeability, and P_v is the water vapor pressure.

Darcy's law:

$$\dot{m}_l = K \frac{\partial P_l}{\partial x} \quad (5)$$

where \dot{m}_l is the mass flux for liquid water, K is the hydraulic conductivity, and P_l is the capillary pressure.

The overall moisture balance is given by

$$\frac{\partial}{\partial x} \left(\mu \frac{\partial P_v}{\partial x} \right) - \frac{\partial}{\partial x} \left(K \frac{\partial P_l}{\partial x} \right) = \rho \frac{\partial w}{\partial t} \quad (6)$$

Because there is no energy generation in the system, the significant energy flows are heat conductivity and enthalpy flow via liquid water transfer and vapor transfer. Thus, the mass and energy conservations are obtained by using Fick's law, Darcy's law, and Fourier's law:

$$\frac{\partial}{\partial x} \left(k \frac{\partial T}{\partial x} \right) + h(T) \frac{\partial}{\partial x} \left(\mu \frac{\partial P_v}{\partial x} \right) = \frac{\partial T}{\partial t} \rho (C_{p,d} + w C_{p,l}) \quad (7)$$

Eq. (6) and Eq. (7) are the governing equations; they need to be solved to predict heat and moisture transfer in building construction layers. For a numerical solution, vapor diffusion and capillary transfer equations need to be decoupled and are given as:

$$\frac{\partial}{\partial x} \left(\mu \frac{\partial P_v}{\partial x} \right) = - \frac{\partial \dot{m}_v}{\partial x} = \rho \frac{\partial w_v}{\partial t} \quad (8. a)$$

$$\frac{\partial}{\partial x} \left(K \frac{\partial P_l}{\partial x} \right) = - \frac{\partial \dot{m}_l}{\partial x} = \rho \frac{\partial w_l}{\partial t} \quad (8. b)$$

$$w = w_v + w_l \quad (8. c)$$

$$\frac{\partial}{\partial x} \left(k \frac{\partial T}{\partial x} \right) + h(T) \frac{\partial}{\partial x} \left(\mu \frac{\partial P_v}{\partial x} \right) = \rho (C_{p,d} + w C_{p,l}) \frac{\partial T}{\partial t} \quad (8. d)$$

The last step for dynamic modeling of building construction layers is identifying a correlation between the surface temperature of the concrete layer and supply water temperature for the TABS. The surface temperature for concrete materials can be calculated from a supply water temperature using equations 8 and 9 [82]. When the thickness of the slab is two L , and its initial temperature of T_1 is cooled with the fluid temperature of T_∞ , a numerical solution is available for the temperature T at a location and time t [82].

$$Y = Y_0 f(b_1 n) \quad (9)$$

where,

$$Y = \frac{T - T_\infty}{T_1 - T_\infty}$$

$$Y_0 = \frac{T_0 - T_\infty}{T_1 - T_\infty} = c_1 \exp(-b_1^2 F_o)$$

$n = x/L$, x = a distance from the midplane of the slab of thickness $2L$ cooled on both sides,

b_1, c_1 = the coefficients that are functions of the Biot number, $F_o = at/L^2$, $a = k/\rho C_p$

$$f(b_1 n) = \cos(b_1 n) \quad c_1 = \frac{4 \sin(b_1)}{2b_1 + \sin(2b_1)} \quad (10)$$

Therefore, if we set $x = L$ and $T = T_{sf}$, we can calculate the surface temperature of the TABS concerning the fluid temperature. In our study, the above dynamic modeling of building construction layers was developed using the MATLAB.

4.1.2. Dynamic Modeling of Buildings

Besides the hygrothermal dynamic modeling of building construction layers, the heat and moisture transfer between outdoor and indoor spaces was modeled to obtain indoor conditions. The heat transfer caused by moisture transport in the wall is far smaller than the heat transfer caused by temperature differences. These terms involving the humidity ratio were neglected. Thus, the general governing equation to describe the energy stored in moist air within the room was simplified to [83]

$$\begin{aligned}
& \rho_a V_{a,in} C_{p,a} \frac{dT_{a,in}}{dt} \\
&= \sum_{i=1}^{N_{walls}} h_{c,i} A_i (T_{wall,i} - T_{a,in}) + \dot{m}_{a,o} C_{p,a} (T_{a,o} - T_{a,in}) \\
&+ \sum_{i=1}^{N_{zones}} \dot{m}_{zone,i} C_{p,a} (T_{zone,i} - T_{a,in}) + \dot{m}_{ground} h(T_{ground}) + \sum_{i=1}^N \dot{Q}_i \quad (11)
\end{aligned}$$

where ρ , V , C_p , T , h_c , A , \dot{m} , and \dot{Q} are density, volume, specific heat, temperature, heat transfer coefficient, area, mass flow rate, and internal heat source, respectively. The subscripts in , and o refer to the indoor and outdoor. The internal heat source, \dot{Q} , is the sum of all the internal heat gains, including heat from occupants, electrical appliances, and cooling effect from the TABS.

For moisture transport in indoor air, the transient humidity ratio of room air is balanced by the moisture transport from indoor latent loads, moisture convection between the room air and wall surfaces, moisture exchange through airflows between multi-zones, and moisture transfer due to infiltration/ventilation with the outdoor air

$$\begin{aligned}
& \rho_a V_{a,in} C_m \frac{dw_{a,in}}{dt} \\
&= \dot{L}_{in} + \sum_{i=1}^{N_{walls}} h_{m,i} A_i (P_{v,i} - P_{v,a,in}) + \sum_{i=1}^{N_{zones}} \dot{m}_i (w_{zone,i} - w_{a,in}) \\
&+ \dot{m}_{a,o} (w_{a,o} - w_{a,in}) \quad (12)
\end{aligned}$$

where C_m is the humidity capacity multiplier, commonly taking the value of 1 [84], \dot{L}_{in} is internal moisture source, and h_m is the convective moisture coefficient, respectively.

The humidity ratio, w , can be expressed by the relative humidity in the air, φ_a ,

$$\varphi_a = \frac{P_v}{P_{v,sat}} = \frac{w_a}{w_{a,sat}} \quad (13)$$

where $P_{v,sat}$ is the saturated vapor pressure, and the saturated humidity ratio, $w_{a,sat}$, is a function of temperature. Therefore, Equation (11) can be rewritten as

$$\begin{aligned} & \rho_a V_{a,in} C_m \left(w_{sat|T_{a,in}} \frac{d\varphi_{a,in}}{dt} + \varphi_{a,in} \frac{dw_{sat}}{dT} \frac{dT_{a,in}}{dt} \right) \\ &= \dot{L}_{in} + \sum_{i=1}^{N_{walls}} h_{m,i} A_i (\varphi_{wall,i} P_{v,sat|T_{wall,i}} - \varphi_a P_{v,sat|T_{a,in}}) \\ &+ \sum_{i=1}^{N_{zones}} \dot{m}_i (\varphi_{zone,i} w_{sat|T_{zone,i}} - \varphi_{a,in} w_{sat|T_{a,in}}) \\ &+ \dot{m}_{a,o} (\varphi_{a,o} w_{sat|T_{a,o}} - \varphi_{a,in} w_{sat|T_{a,in}}) \end{aligned} \quad (14)$$

In summary, Equations (11) and (14) provide the heat and moisture transfer relationships of room air and wall surface in a building, thus enabling the surface condensation prediction in advance.

4.1.3. Solar Heat Flux

Using the dynamic models in Section 4.1.1 and 4.1.2, indoor hygrothermal condition changes can be predicted in relation to weather forecast data. However, besides heat and moisture flux calculated by the dynamic models in Section 4.1.1 and 4.1.2, solar heat flux through the building envelope has a significant impact on indoor condition change, thus for the indoor thermal comfort. Therefore, solar heat flux estimation should be incorporated for more accurate dynamic modeling. According to I. Hazyuk et al., [71], to estimate solar heat flux, Φ_{solar} , the radiation on each façade should be determined in relation to the corresponding surface area and add all the estimation for each façade. Considering an isotropic model of the sky, the solar radiation on a tilted surface is calculated by [85]

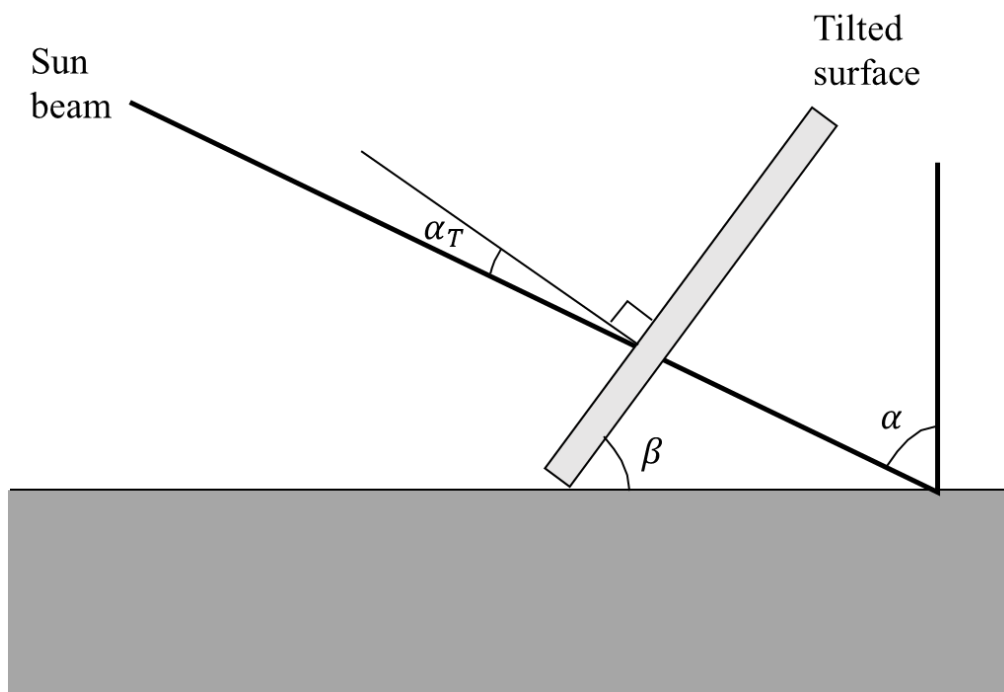


Figure 20. Solar radiation on a tilted surface

$$I_T = I_{beam}R_{beam} + I_{diffuse} \frac{1 + \cos(\beta)}{2} + (I_{beam} + I_{diffuse})\rho_g \frac{1 - \cos(\beta)}{2} \quad (15)$$

where the ground albedo ρ_g is generally 0.2 and the ratio of beam radiation on a tilted surface to that on a horizontal surface is calculated by

$$R_{beam} = \frac{\cos(\alpha_T)}{\cos(\alpha)} \quad (16)$$

the angles α_T and α are the incidence angles of the beam radiation on the tilted surfaces and the horizontal surface respectively, which can be estimated by

$$\begin{aligned} \cos(\alpha) &= \sin(\delta) \sin(\phi) + \cos(\delta) \cos(\phi) \cos(\theta) \\ \cos(\alpha_T) &= \sin(\delta) \sin(\phi) \cos(\beta) - \sin(\delta) \cos(\phi) \sin(\beta) \cos(\gamma) \\ &\quad + \cos(\delta) \cos(\phi) \cos(\beta) \cos(\theta) + \cos(\delta) \sin(\phi) \sin(\beta) \cos(\gamma) \cos(\theta) \\ &\quad + \cos(\delta) \sin(\beta) \sin(\gamma) \sin(\theta) \end{aligned} \quad (17)$$

with

$$\delta = 23.45 \sin\left(\frac{360(284 + n)}{365}\right) - \text{solar declination in the } n\text{th day of the year}$$

ϕ – geographical latitude of the location where the building is

γ – azimuth angle of the surface, zero for south, negative for west, positive for east

$\theta = 15(t - 12)$ – solar hour angle at the moment t

β – the angle between the tilted surface and the horizontal plane

Assuming that all facades are perpendicular to the horizontal plane, the incidence angle of beam radiation on the façade wall is

$$\cos(\alpha_T) = -\sin(\delta) \cos(\phi) \cos(\gamma) + \cos(\delta) \sin(\phi) \cos(\gamma) \cos(\theta) + \cos(\delta) \sin(\gamma) \sin(\theta) \quad (18)$$

and total solar radiation on a wall is

$$I_T = I_{beam} \left(R_{beam} + \frac{\rho_g}{2} \right) + I_{diffuse} \frac{1 + \rho_g}{2} \quad (19)$$

After solar radiation on each façade is estimated, total solar heat flux on building façade can be estimated by

$$\Phi_{solar} = \sum_{i=1}^n I_{Ti} S_i \quad (20)$$

When there is fenestration on each façade, windows to wall ratio and solar heat gain coefficient (SHGC) are multiplied to the solar heat flux to estimate internal solar heat gain.

4.2. Experimental Setup and Instrumentation

A series of experiments were conducted in a test chamber (Figure 21-a) to measure the surface condensation's progress on concrete material. As shown in Figure 21-a, the space in the chamber was vertically divided into an upper space (2m×2m×1m) and a lower room (2m×2m×1m); a test concrete sample (area: 350mm×470mm, thickness: 25mm) was installed in between the two spaces.

Based on Friembichler et al., [86], the surface temperature needs to be within the 15 °C - 22 °C range to generate the desirable indoor condition with radiant cooling systems. On the other hand, Pfafferott et al., [87] recommend creating a surface temperature higher than 18 °C to provide indoor thermal comfort. Therefore, 15 °C and 18 °C are chosen as the surface temperature settings for the experiments. For the indoor relative humidity settings, 65 % and 80 % levels are selected for the experiments.

Thus, in the upper space, the relative humidity level is kept constant using a dehumidifier and cold air (13°C - 16°C) is supplied from a cooling unit to produce the ceiling surface temperature range (15°C - 18°C) of the TABS. In the lower space, the indoor relative humidity is kept at a relatively high level (65% - 80%) to generate the surface condensation intentionally. The air temperature in the lower space is always remained at 25 °C to provide a generally accepted indoor air temperature condition.

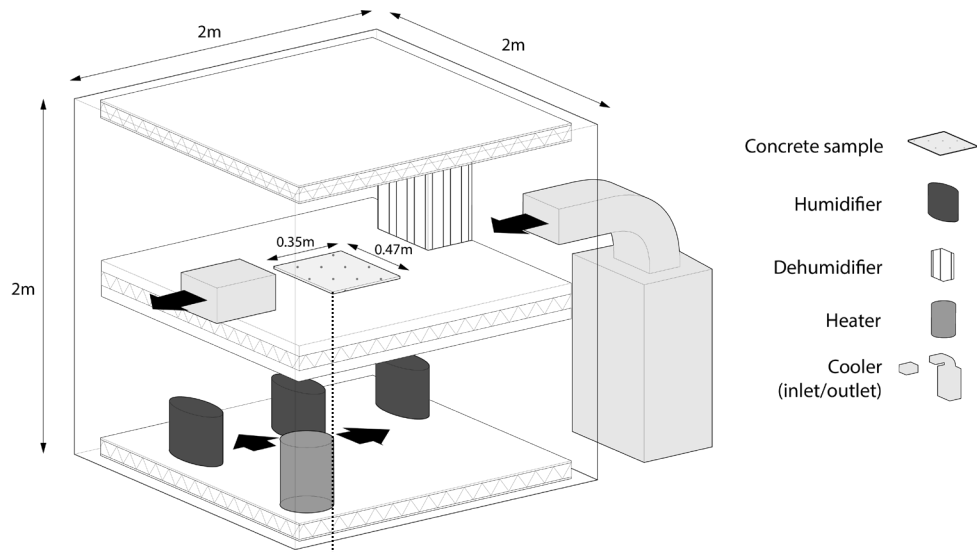


Figure 21-a. Experimental equipment settings of the chamber

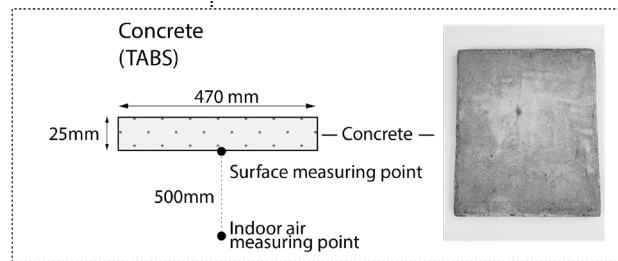


Figure 21-b. Measuring points inside the chamber



Figure 22. Measuring equipment setting

Table 9. Test condition settings

Combinations	Surface temperature (T_{sf})	Indoor air relative humidity (φ_{in})	Indoor air temperature (T_{in})
	[°C]	[%]	[°C]
A	15	80	25
B	18	80	25
C	15	65	25
D	18	65	25

Under the four different temperature and relative humidity settings (Table 9), a concrete material was tested. Surface temperature and relative humidity change of the concrete sample were measured at 10-minute intervals. Each test was continued until the surface condensation occurred. Figure 21-a shows the chamber's experimental equipment setting, and Figure 21-b shows measuring points inside the chamber. K-type wire thermocouple sensors (accuracy of $\pm 2^{\circ}\text{C}$) were used for temperature measurement, and HIH-4000 sensors (accuracy of $\pm 3.5\%$) were used for relative humidity measurement. K-type wire thermocouple sensors were always calibrated with ice water before being placed on the measuring points. Both temperature and relative humidity measurement data were validated with the Michell Instruments PCMini52 humidity mini probes (accuracy of relative humidity: $\pm 2.0\%$ / temperature: $\pm 0.2^{\circ}\text{C}$).

As a result of these choices shown in Table 9, the cold air (13°C or 16°C) was supplied continuously from a cooling unit to produce the ceiling surface temperature (15°C or 18°C) of the TABS. In the lower space, the indoor relative humidity was kept at a relatively high level (65% or 80%) to intentionally generate the surface condensation. The air temperature in the lower space was always remained at 25°C to provide a generally accepted indoor air temperature condition with TABS operation.

A condensation sensor (HDS10) was installed adjacent to the relative humidity sensor to verify the actual surface condensation occurrence. Figure 23-a shows the initial test results of surface relative humidity change. The indoor air temperature was maintained at 25°C and the relative humidity level was kept at 80%. Then, starting from a surface temperature of 15°C , the cooling unit was intentionally turned on/off to mimic the TABS operation under humid conditions. As shown in Figure 23-a, the surface relative humidity level increases as surface temperature drops (Figure 23-b). As the surface relative humidity plot demonstrates, the saturation level was reached

approximately 70 minutes after dropping the surface temperature to 15°C. However, based on the condensation sensor (HDS10), actual condensation occurred after 80 minutes.

Initial test results reveal a specific time gap between the indication of surface condensation shown by the humidity sensor and the condensation sensor. As demonstrated by G.P. Vasilyev et al. [90], the surface condensation development is governed by the moisture content (w [%]) and the maximum hygroscopic moisture content of a given material rather than by the relative humidity level. Therefore, volumetric moisture contents (Figure 23-c) were further plotted using the correlation between the volumetric moisture content and the concrete material's relative humidity levels [90]. As shown in Figure 23-c, the actual condensation (80 minutes after dropping the surface temperature to 15°C) matches the time when the volumetric moisture content reaches the maximum hygroscopic moisture content of approximately 1.40%. These initial test results demonstrate that the surface condensation occurs only after the volumetric moisture content exceeds the concrete material's maximum hygroscopic moisture content.

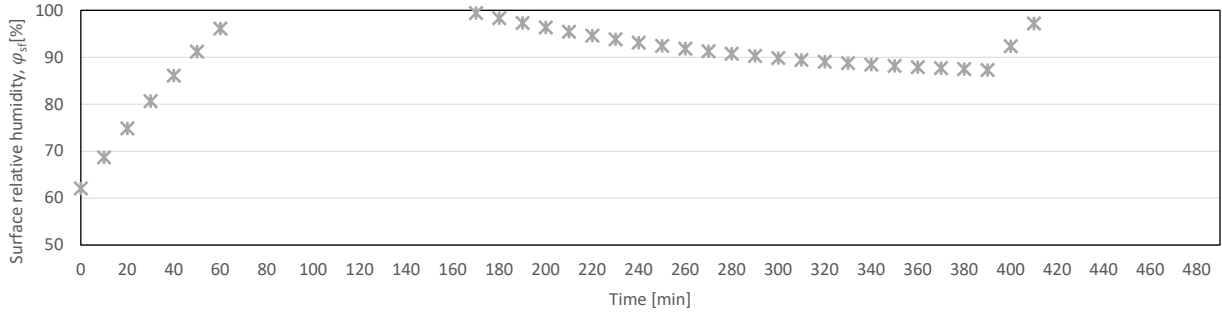


Figure 23-a. Initial test results: surface relative humidity, φ_{sf}

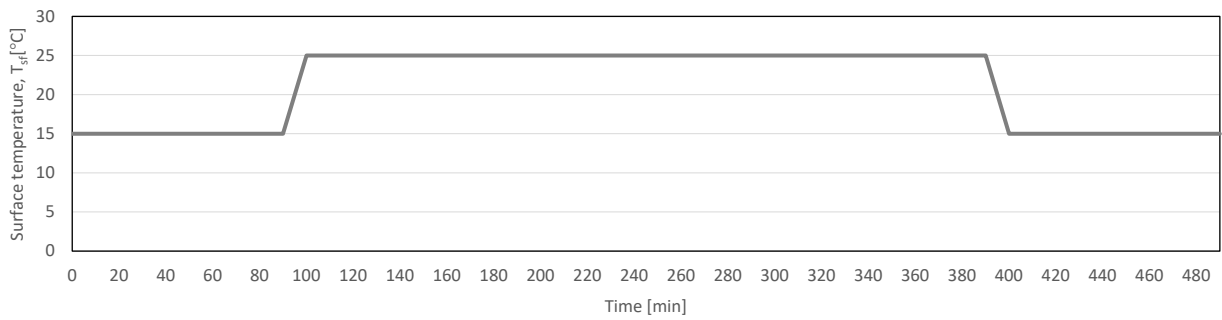


Figure 23-b. Initial test results: surface temperature, T_{sf}

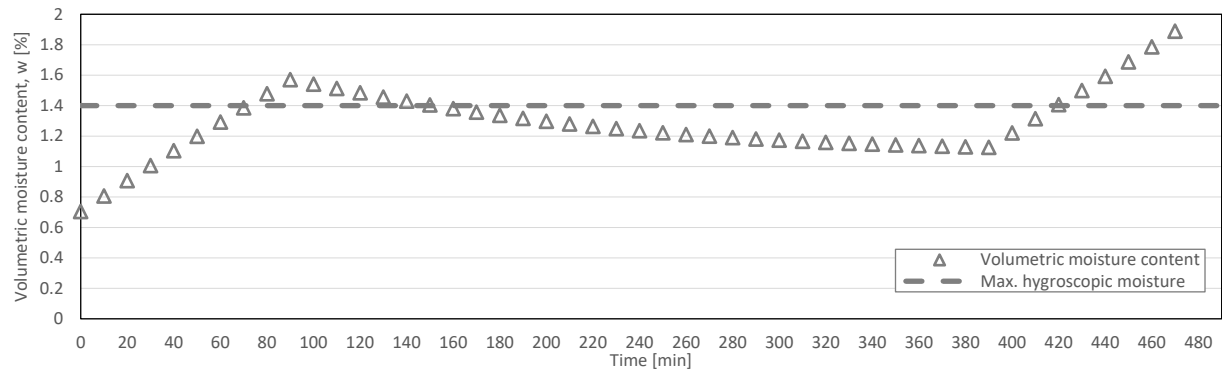


Figure 23-c. Initial test results: volumetric moisture content, w

Thus, for the current condensation prediction model, the volumetric moisture content was chosen as an indicator for surface condensation development. When the moisture content is adopted as the condensation indicator, the moisture diffusion process can be considered both past and present stages, therefore enabling a more accurate surface condensation prediction.

4.3. Model Calibration Using a Curve-fitting Process

Although the volumetric moisture content is chosen as an indicator for surface condensation development, validation in relative humidity prediction is still essential because the volumetric moisture content level is computed from the surface relative humidity levels. When a gap exists between the dynamic model results and the measurement, severe errors can occur in the surface condensation prediction. This discrepancy can arise from uncertain physical property values of building materials (e.g., heat conductivity, specific heat capacity, vapor permeability, etc.) or an inappropriate convective heat transfer coefficient [91]. Thus, reliable physical property values and the convective heat transfer coefficient need to be identified with a model calibration approach.

For the current study, a curve-fitting process was utilized as the model calibration method. The goal of the curve-fitting process was to find a simulated curve that best fit the measured data. The physical property values and the convective heat transfer coefficient in the dynamic model were adjusted to minimize the difference between the simulated data and the measured data. This best-fit curve searching process was iterated until the gap between the simulated data and the measured data falls to an acceptable error. When the best fit curve was found, the most feasible physical property values and heat transfer coefficient were derived from the curve.

Table 10 shows the physical parameters to be adjusted with the curve-fitting process. A total of five physical parameters were selected: the heat conductivity, the density, the specific heat capacity, the vapor permeability, and the convective heat transfer coefficient. The range of each physical parameter was chosen from the references [90, 92]. However, the literature provides different recommendations for the convective heat transfer coefficient; the uniform, a range of 2.5-5 W/m² was selected from common values [93–95]. Numerous combinations are possible when

you want to pick the values from each physical parameter value range randomly; testing all possible combinations will take too much time and effort.

Table 10. Physical parameters and their ranges for the curve-fitting process

	Heat conductivity (k) W/m K	Density (ρ) kg/m ³	Specific heat capacity (C_p) J/kg K	Vapor permeability (μ) kg/m s Pa	Convective heat transfer coefficient ($h_{c,in}$) W/m ² K
Concrete	0.5–2.0	1800–2500	500–1000	1×10^{-12} – 1×10^{-11}	2.5–5

The combinations for physical parameters were chosen deliberately rather than randomly to save time searching for the most possible physical property values and the convective heat transfer coefficient. An optimization solver narrows the number of combinations by adopting a specific algorithm. In this study, a genetic algorithm, which takes the principle of evolution by natural selection [96], was utilized as the optimization solver. With the genetic algorithm, the number of combinations to be tested was reduced rapidly, which led to significant time savings in the curve-fitting process. The current curve-fitting process’s fitness function was the mean squared error (MSE) between the simulated relative humidity data and the measured comparable humidity data. A smaller MSE indicated a better fit of the data.

Four curves under each test condition setting (Table 9) were fitted at once to obtain reliable physical property values of the concrete material and the convective heat transfer coefficient from the experimental settings. When the overall MSE between simulated data and measured data fell to the acceptable range, we presume that the physical parameter values and the convective heat transfer coefficient were feasible for the current physical condition setting.

4.4. An MPC-based Surface Condensation Prevention Framework Development

When the dynamic model predicts the future state, the MPC framework determines whether the control input is appropriate or not for the system operation. An objective function and constraints are the criteria for evaluating the suitable control input. These criteria need to be established for the MPC-based framework. A goal of the current MPC framework is to provide thermal comfort for occupant with minimum energy input. To simplify the MPC design, the surface temperature for the TABS was used for the cooling energy input parameter. For the thermal comfort parameter, operative temperature which consider both air temperature and mean radiant temperature, was used to accurately reflect the surface radiant cooling effect from the TABS.

Below are the objective function and regulations that are set for the MPC-based TABS operation:

$$\begin{aligned} &\text{minimize: cooling energy input for TABS } (T_{sf}) \\ &\quad \text{gap between setpoint and current operative temperature } (T_{op}) \quad (21) \\ &\text{subject to: prevent surface condensation } (w < w_{max}) \\ &\quad \text{a threshold of cooling energy input for TABS } (T_{sf,min} < T_{sf}) \end{aligned}$$

Here we define both minimizing the cooling energy input for TABS (T_{sf}) and minimizing a gap between setpoint ($T_{op} = 26^\circ\text{C}$) and current operative temperature (T_{op}) as the objective function; the volumetric moisture content (w) of the concrete construction layers less than the maximum hygroscopic level (w_{max}) is set as the first constraint to prevent the surface condensation; maximum cooling energy input for the TABS ($T_{sf,min} = 15^\circ\text{C}$) is set as the second constraint. Minimizing a gap between the setpoint and current operative temperature (T_{op}) was set

ten times higher weighting factor than minimizing the cooling energy input for TABS (T_{sf}) because indoor thermal comfort should not be compromised to reduce cooling energy. When the volumetric moisture content is predicted to exceed the maximum hygroscopic moisture content, the MPC framework will increase the surface temperature of the TABS or turn off the TABS to avoid surface condensation.

The operative temperature of 26°C is set as the setpoint to ensure the thermal comfort level. Numerically, the operative temperature can be computed from [4]:

$$T_{op} = \frac{h_r T_{mr} + h_c T_{in}}{h_r + h_c} \quad (22)$$

where, T_{op} = operative temperature, h_r = radiant heat transfer coefficient, T_{mr} = mean radiant temperature, h_c = convective heat transfer coefficient, and T_{in} = indoor air temperature. Based on Equation (22), operative temperature T_{op} can be defined as the average of the mean radiant temperatures and indoor air temperatures, weighted by their respective heat transfer coefficient [4]. In most conditions where the indoor air velocity is less than 0.2 m/s and the difference between mean radiant temperature and indoor air temperature is relatively small, the operative temperature can be simplified to [4]:

$$T_{op} = 0.5 T_{in} + 0.5 T_{mr} \quad (23)$$

In this study, above Eq. (23) was utilized to calculate operative temperature. While T_{in} can be derived from the dynamic model of buildings, T_{mr} , the area weighted mean surface radiant temperature of interior surface can be calculated by,

$$MRT_A = \frac{\sum T_{sf} \cdot \theta}{360} = \frac{T_{sf1} \cdot \theta_1 + T_{sf2} \cdot \theta_2 + T_{sf3} \cdot \theta_3 + \dots}{360} \quad (24)$$

where MRT_A indicates mean radiant temperature for point A, T_{sf} denotes surface temperature of interiors, and θ denotes exposure angle of a surface from the point being considered. In the current study, point A was assumed to be the occupant's eye level who is seated in the middle of the space. However, when occupants are not sitting in the middle of the space but standing at the corner of the space, the surface radiant cooling effect from the TABS would be completely different (Figure 24), which in turn leads to the different estimation of the mean radiant temperature. For future works, the MPC framework will include the mean radiant temperature estimation that considers both the volume of the space and exact positioning of occupants, so that more accurate operative temperature can be computed.

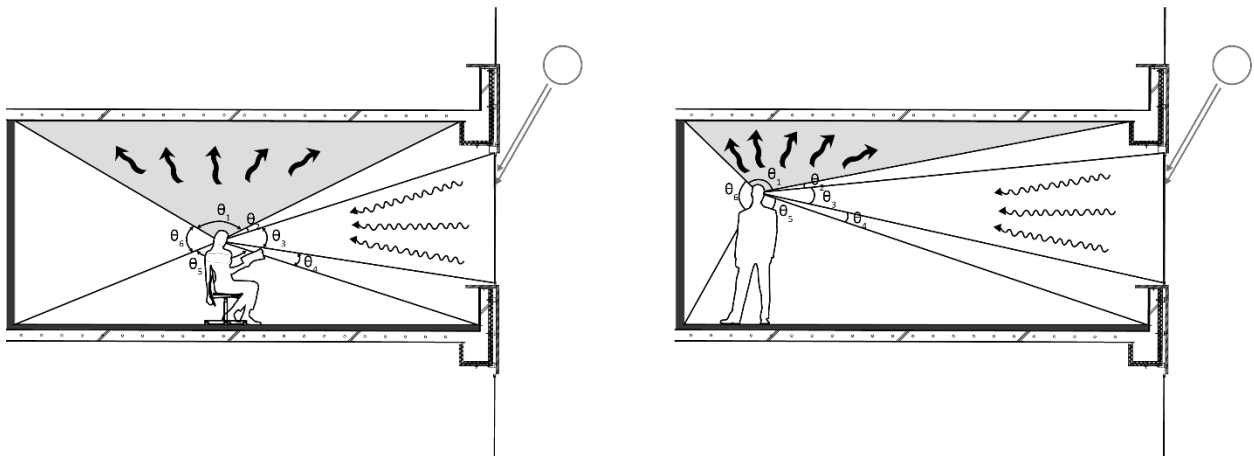


Figure 24. Mean radiant temperature change according to the position of occupants

Finally, the space-state for each control time-step can be derived from the partial theoretical model [47]:

$$\mathbf{x}(k + 1) = \mathbf{A}\mathbf{x}(k) + \mathbf{B}_1\mathbf{u}(k) + \mathbf{B}_2\mathbf{w}(k) \quad (25)$$

$$\mathbf{y}(k) = \mathbf{C}\mathbf{x}(k) + \mathbf{D}_1\mathbf{u}(k) + \mathbf{D}_2\mathbf{w}(k) \quad (26)$$

where \mathbf{u} denotes the controllable input (the heat flux from the TABS), and \mathbf{w} denotes known uncontrollable inputs (weather data). \mathbf{D}_1 and \mathbf{D}_2 from the above model are usually null and thus can be omitted. The whole process of solving the MPC problem can be found in Appendix A.

In most cases, the TABS is coupled with sub-mechanical ventilation cooling systems [8]; the majority of sensible cooling loads are covered with the TABS while the rest of the cooling load and ventilation demand is controlled by the sub-mechanical ventilation cooling systems. In this coupled system, the surface condensation risk can be prevented either by the dehumidification process or simply turning off the TABS and operating the air-based cooling system [97–99]. However, in warm and humid climate regions, these two control approaches will only narrow the operable periods for the TABS, leading to heavy dependence on the air-based cooling systems.

If these TABS are governed by the proposed MPC-based surface condensation prevention framework, the correct surface cooling temperature for the TABS operation can be identified from the dynamic models; therefore, the operable chances for the TABS are increased without developing the surface condensation even in warm and humid climate regions.

4.5. Site-specific Surface Condensation Prevention Performance Analysis

As addressed in Section 2.2, based on the IECC's classification, the climatic regions in the U.S. are simply classified into eight climate zones, and subdivided into A (Moist), B (Dry), and C (Marine), which specifies the humidity level of the climate zone. Even if the IECC climate zone classification has been widely accepted for the basis of the U.S. building code, when it comes to site-specific microclimatic conditions, strict reliance on the IECC map (Figure 11) can result in a discrepancy between actual sites' climatic conditions and the conditions that are categorized and defined by the IECC climate classification. This broad and general classification by the IECC climate zone map can misdirect designers' or builders' utilization of the proposed MPC framework. The building sites adjacent to each other can sometimes experience significantly different weather conditions, although they are within the same IECC climate zone. Thus, site-specific estimation should help the designers and builders make better utilization of the proposed MPC framework and justify their application of the proposed MPC framework for the TABS operation for their project.

Total 845 annual weather data (TMY, TMY2, and TMY3) of each site were collected from the U.S. Department of Energy website. These data were utilized for 1) annual surface condensation risk estimation while the TABS operation and 2) surface condensation prevention performance using the proposed MPC framework. Here, I present "*MPC condensation prevention performance index*" shown in Eq. (27) for the surface condensation prevention performance analysis. The estimation results were then visualized with geographic plots that can help designers and builders to examine the impact of their proposed MPC framework choices while the TABS operation for their projects. Figure 25 shows the analyzed United States sites in this study. The lists of analyzed sites are addressed in Appendix B.

MPC condensation prevention performance index [%] =

$$\frac{\text{Hours of surface condensation on TABS (on/off)} - \text{Hours of surface condensation on TABS (MPC)}}{\text{Hours of surface condensation on TABS (on/off)}}$$

(27)

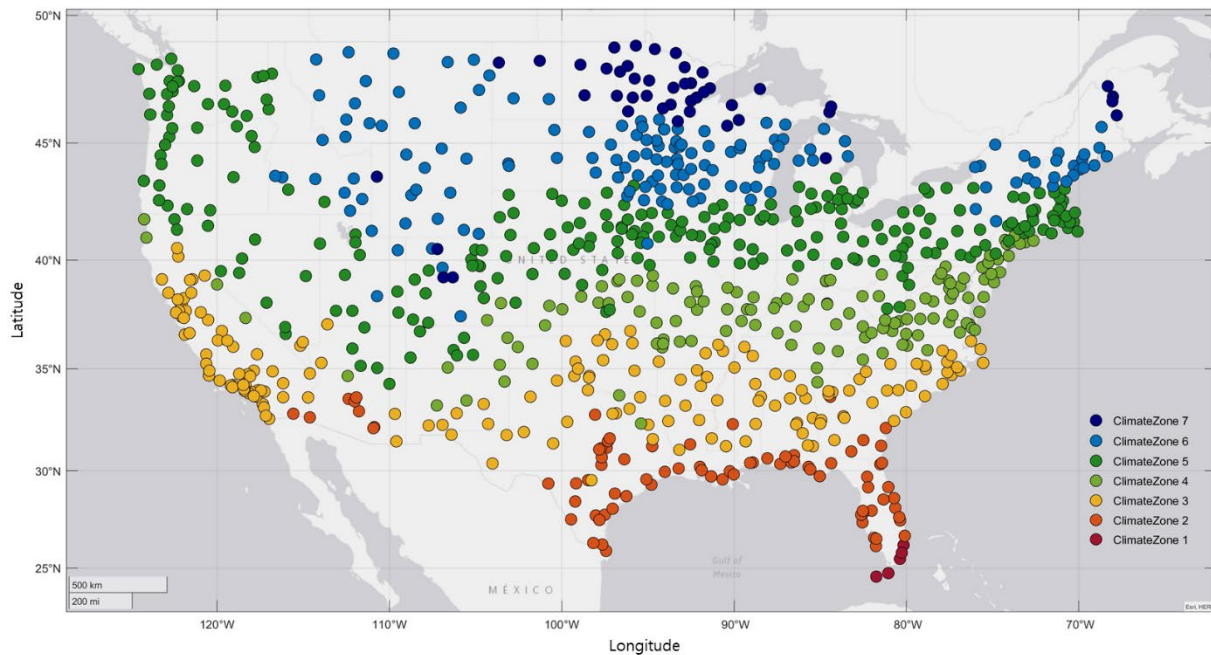


Figure 25. Analyzed U.S. sites in this study (based on the IECC climate zone classification)

4.6. Energy Savings and Cost Reduction by the MPC-based TABS Operation

Based on the site-specific surface condensation prevention performance analysis from Section 4.5, applicability of the proposed MPC framework (extended operable period with the MPC framework, compared to the on/off control) for each site can be determined.

Table 11. The selected site for each climate zone (Energy savings and cost reduction analysis)

Climate zone	Subdivision	State	City	The average price of electricity to ultimate customers by end-use sector, commercial [¢/kWh]
1	A (Moist)	FL	Miami	9.47
2	A (Moist)	TX	Austin	7.93
3	A (Moist)	SC	Charleston	9.94
3	C (Marine)	CA	San Francisco	17.64
4	A (Moist)	PA	Philadelphia	8.65
4	C (Marine)	CA	Crescent City	17.64
5	A (Moist)	IL	Chicago	9.14
6	A (Moist)	MN	Minneapolis	10.04
7	A (Moist)	MN	Duluth	10.04

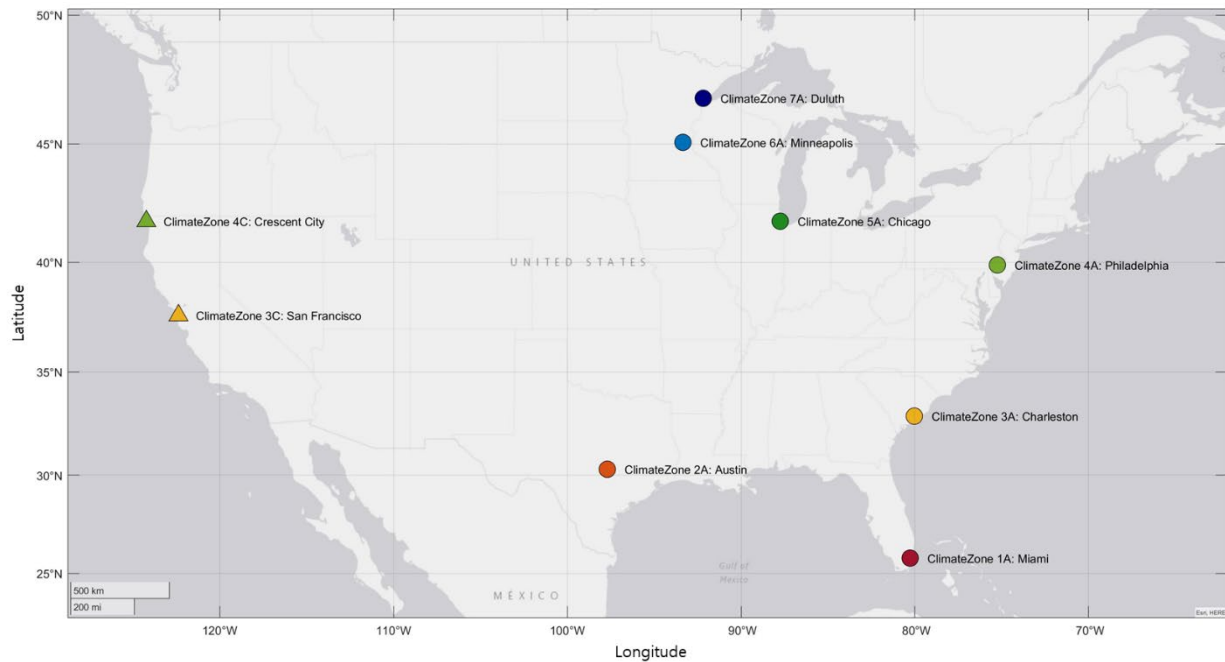


Figure 26. Location of the selected sites for each climate zone (Energy savings and cost reduction analysis)

The above sites shown in Table 11 and Figure 26, were chosen from the total 845 climatic regions collected from the U.S. Department of Energy website to estimate the proposed MPC-based surface condensation prevention framework’s energy savings potential and operational cost reduction. Each site represents typical zone climatic conditions categorized by the IECC. Under each site, three cooling modes (mechanical ventilation cooling, TABS with on/off control, and TABS with MPC) were tested in a room of medium-size office building defined by the Building

Energy Code program (Figure 27) [100]. The thermal performance of building envelopes was based on the requirement of the ASHRAE 90.1 [101] specification (Table 12), and the infiltration rate was kept constant at 0.25 air changes per hour. The medium-size office building's total floor area was 1,650 m² (50m × 33m). A configuration of the simulated room was 39.5m (width) × 10m (depth) × 4m (height), facing south façade with 33% windows to wall ratio.

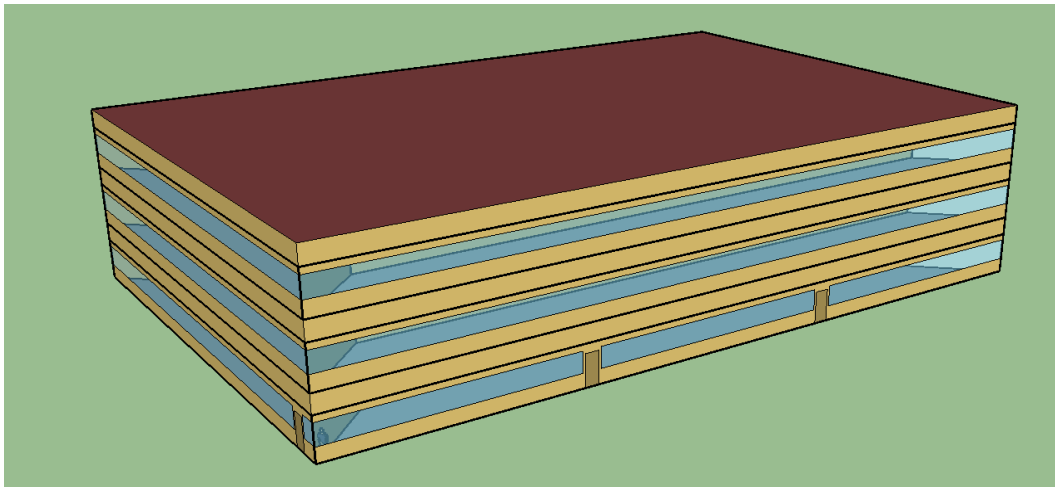


Figure 27. Prototype medium-size office building defined by the Building Energy Code Program

The baseline mechanical ventilation cooling mode denotes a minimum outdoor air supply with recirculation air operation mode without using the TABS. The TABS using the on/off control refers to a minimum new air supply from sub-mechanical ventilation system with simple TABS operation that is governed by the on/off control algorithm. When the surface temperature of TABS reaches dewpoint temperature, the system turns off the TABS until the surface condensation risk gets smaller. Then, the plan depends on the sub-mechanical ventilation cooling system. The TABS with MPC cooling mode denotes a minimum outdoor air supply from sub-mechanical ventilation system with the TABS operated based on a developed surface condensation prevention framework.

When the surface condensation is predicted, the system increases the surface temperature to keep the TABS operation while preventing the surface condensation development.

Table 12. The building envelope requirements for each climate zone (ASHRAE 90.1 [101])

Climate zone 1	Roofs	Walls	Floors	Slab-on-Grade	Fenestration
Max. U-value [W/m ² K]	0.273	0.704	1.987	4.145	2.839
Min. R-value [m ² K/W]	3.522	2.289	-	-	-
SHGC	-	-	-	-	0.230
VT	-	-	-	-	0.253
Climate zone 2	Roofs	Walls	Floors	Slab-on-Grade	Fenestration
Max. U-value [W/m ² K]	0.221	0.477	0.216	4.145	2.555
Min. R-value [m ² K/W]	4.403	2.959	5.283	-	-
SHGC	-	-	-	-	0.250
VT	-	-	-	-	0.275
Climate zone 3	Roofs	Walls	Floors	Slab-on-Grade	Fenestration
Max. U-value [W/m ² K]	0.221	0.437	0.216	4.145	2.385
Min. R-value [m ² K/W]	4.403	3.170	5.283	-	-
SHGC	-	-	-	-	0.250
VT	-	-	-	-	0.275
Climate zone 4	Roofs	Walls	Floors	Slab-on-Grade	Fenestration
Max. U-value [W/m ² K]	0.182	0.363	0.216	2.953	2.044
Min. R-value [m ² K/W]	5.283	3.610	5.283	2.642	-
SHGC	-	-	-	-	0.360
VT	-	-	-	-	0.396
Climate zone 5	Roofs	Walls	Floors	Slab-on-Grade	Fenestration
Max. U-value [W/m ² K]	0.182	0.312	0.216	2.953	2.044
Min. R-value [m ² K/W]	5.283	4.051	5.283	2.642	-
SHGC	-	-	-	-	0.380
VT	-	-	-	-	0.418
Climate zone 6	Roofs	Walls	Floors	Slab-on-Grade	Fenestration
Max. U-value [W/m ² K]	0.182	0.278	0.182	2.896	1.931
Min. R-value [m ² K/W]	5.283	4.491	6.692	3.522	-
SHGC	-	-	-	-	0.380
VT	-	-	-	-	0.418
Climate zone 7	Roofs	Walls	Floors	Slab-on-Grade	Fenestration
Max. U-value [W/m ² K]	0.159	0.278	0.182	2.896	1.647
Min. R-value [m ² K/W]	6.164	4.491	6.692	3.522	-
SHGC	-	-	-	-	0.400
VT	-	-	-	-	0.440

At first, user sensible and latent cooling energy demands were calculated under each climatic region. The dynamic modeling from 4.1 was used for user cooling energy demand calculation and the calculation results were validated with EnergyPlus. The annual weather data from the Department of Energy were adopted for the calculation. At the same time, I estimated the TABS's operable periods by both the on/off control logic and the model predictive control. To simplify the calculation process, the annual weather data from the Department of Energy were utilized for both current weather conditions and weather forecast data. The estimated TABS operable periods by each cooling mode were being used for the site distribution energy calculation.

Then, the site cooling energy for different cooling modes was calculated. To be complete with the site cooling energy calculation, cooling energy from compression chiller, energy for cooling tower, and distribution energy were calculated under each climatic condition for three different cooling modes: mechanical ventilation cooling, TABS with on/off control, and TABS with MPC.

Finally, annual operational costs for the cooling operation under each climatic region were calculated from the "*average price of electricity to ultimate customers by end-use sector, commercial*" provided by the U.S. Energy Information Administration (EIA) [102] shown in Table 11.

In the following section, accuracy and reliability of the developed dynamic models are improved with the curve-fitting process. Based on the calibrated dynamic models, an MPC-based surface condensation prevention framework is developed. Then, using the proposed MPC framework, site-specific condensation prevention performances throughout the climatic regions in the U.S. were analyzed and visualized in geographical plot. Finally, compared to the conventional

mechanical ventilation cooling systems, the energy savings and cost reduction with the MPC-based TABS operation are estimated.

CHAPTER 5. Results and Discussion

5.1. Experiment Results

The surface relative humidity data obtained from the experiments are shown as scattered plots in Figure 28. As shown in Figure 28, under combination A ($\varphi_{in}=80\%$ and $T_{sf}=15^{\circ}\text{C}$ conditions) shown in Table 9, the surface relative humidity reached 100% after 70 minutes. Under combination B, it took 30 minutes additionally (i.e., total 90 minutes) to reach 100% surface relative humidity. In contrast, under combination C, it took 110–120 minutes for the concrete sample to reach 100% surface relative humidity. Under combination D, it took 180 minutes for the concrete sample to reach 100% surface relative humidity.

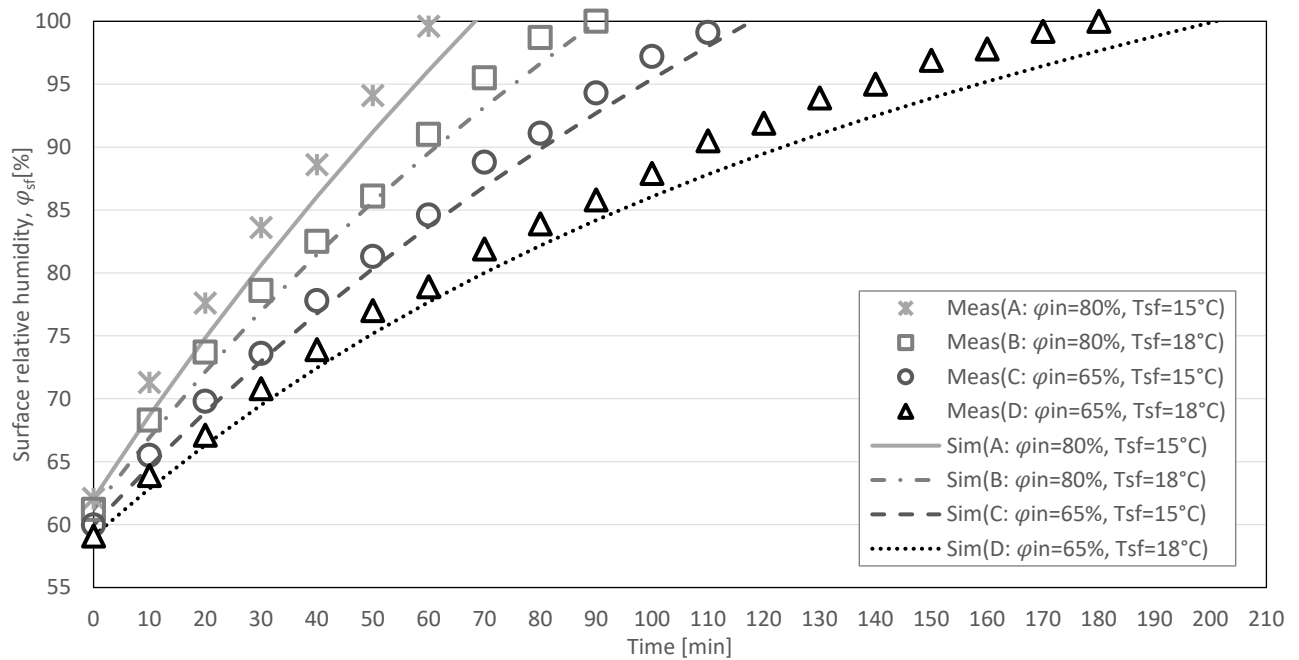


Figure 28. Measured data and simulation data after the curve-fitting process

Under combination A ($\varphi_{in}=80\%$ and $T_{sf}=15^{\circ}\text{C}$ settings), the surface relative humidity reached 100% the most rapidly. On the other hand, the combination D setting took the longest time to reach 100% surface relative humidity of the concrete sample. When comparing the required times to reach 100% surface relative humidity between combination B and combination C, it is apparent that combination B ($\varphi_{in}=80\%$ and $T_{sf}=18^{\circ}\text{C}$) setting takes less time to reach 100%.

5.2. Model calibration Results

The surface relative humidity curves generated from the dynamic model were calibrated with the measured data using the curve-fitting process. For the initial dynamic simulation run (without the curve-fitting process), the mid-range value from Table 10 in Section 4.3 were chosen for each physical parameter. To estimate the model calibration performance, the mean squared errors (MSE) of the dynamic model were calculated with and without the curve-fitting process (Table 13). The overall MSE between the simulated data and measurement was reduced by 47.2% after the curve-fitting process. When we split the MSE into each condition setting, the largest MSE was under $\varphi_{in}=80\%$ and $T_{sf}=15^{\circ}\text{C}$ setting. This largest MSE may result from the relatively small number of samples. In general, the overall MSE between the simulated data and measured data shows good agreement after the curve-fitting process has been conducted (Figure 28).

Table 13. MSE change with curve-fitting process

Material	Curve- fitting process	MSE	MSE	MSE	MSE	MSE Total
		$\varphi_{in} = 80\%$ $T_{sf} = 15^{\circ}\text{C}$	$\varphi_{in} = 80\%$ $T_{sf} = 18^{\circ}\text{C}$	$\varphi_{in} = 65\%$ $T_{sf} = 15^{\circ}\text{C}$	$\varphi_{in} = 65\%$ $T_{sf} = 18^{\circ}\text{C}$	
Concrete	w/o	9.667	5.031	2.808	10.997	7.388
	w/	7.879 (↓18.5%)	3.291 (↓34.6%)	1.428 (↓49.1%)	4.383 (↓60.1%)	3.904 (↓47.2%)

Table 14 shows the resultant physical property values and the convective heat transfer coefficient obtained after the curve-fitting process.

Table 14. The physical property values and the convective heat transfer coefficient obtained after the curve-fitting process

Material	k [W/m K]	ρ [kg/m ³]	C_p [J/kg K]	μ [kg/m s Pa]	$h_{c,in}$ [W/m ² K]
Concrete	1.5	2500	600	3×10^{-12}	3.5

5.3. Required Time Charts of Surface Condensation Development

Although the dynamic model was calibrated and showed reduced MSE (Table 13), these errors still have a risk of incorrectly predicting the surface condensation. To address this uncertainty, a safety factor approach was adopted for complete surface condensation control. Prior research [103, 104] introduce the safety factor approach for surface condensation control, and both references recommend subtracting surface temperature by 1–2 K before inputting it to the surface condensation prediction. The risk of failing to predict the surface condensation accurately can thus be almost completely eliminated with the safety factor approach. In this study, surface temperature was subtracted by 2 K before inputting it to the surface condensation prediction to bring safety factor approach.

In general, the TABS are coupled with sub-mechanical ventilation cooling systems for the purpose of cooling rooms; the majority of sensible cooling load is covered with the TABS while the rest of the cooling load and ventilation demand are controlled by the sub-mechanical ventilation cooling systems. When occupants are in sedentary physical activity under air-conditioned environment with a negligible air movement (< 0.2 m/s), the thermal comfort is mainly determined by the mean radiant temperature and air temperature [6]. In these conditions, indoor air temperature can be remained closer or even higher than the generally accepted thermal comfort

threshold of 25°C, because the majority of sensible cooling load can be covered by the radiant cooling effect from the TABS.

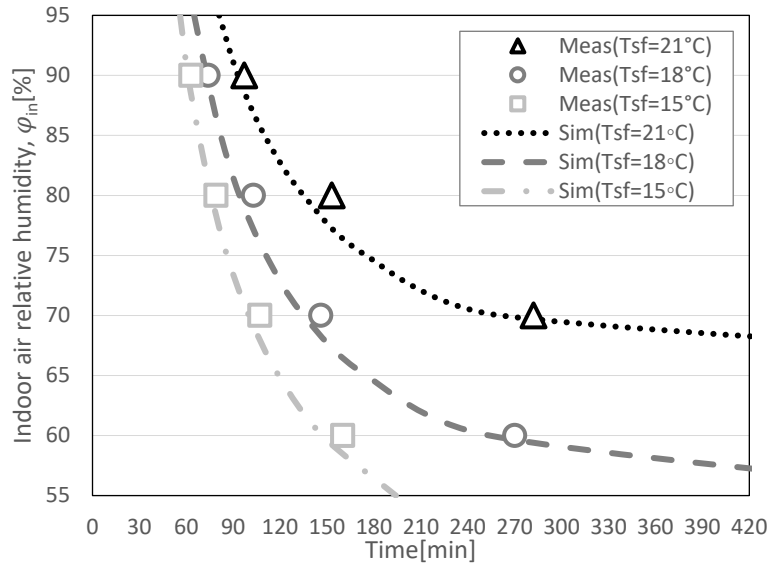


Figure 29. Validation results for the required time of surface condensation development on the concrete

Based on the above-mentioned cooling system operation scenario, I propose a simple model predictive control method for the surface condensation on the TABS. The plotted curves in Figure 29 show the time required to develop the surface condensation for the current concrete sample under $T_{in}=25^{\circ}\text{C}$ with a specific boundary condition (surface temperature and indoor relative humidity level). Numerous simulations were conducted after shifting boundary conditions and the simulation results were interpolated to generate the curves shown in Figure 29. The required time to develop the surface condensation under each boundary condition was estimated based on the time frame within which the volumetric moisture content of the concrete material reached maximum hygroscopic moisture content (1.40%).

To validate these curves, the chamber tests were conducted again. For these tests, surface temperature of 21°C was included in addition to the formal test condition settings (Table 9); indoor air relative humidity settings were in a range from 60% to 90% at 10% intervals, under 25°C indoor air temperature. As shown in Figure 29. and Table 15, regardless of boundary condition settings, the simulation results had always slightly shorter time frames than the measurement results. Thus, the risk of incorrect prediction of the surface condensation decreases during the cooling periods when the TABS is in operation.

Table 15. Required time to develop surface condensation from measurement and simulation

T_{sf}	Method	$\varphi_{in} = 90\%$	$\varphi_{in} = 80\%$	$\varphi_{in} = 70\%$	$\varphi_{in} = 60\%$
15°C	Measurement	63 [min]	79 [min]	107 [min]	160 [min]
	Simulation	61 [min]	76 [min]	100 [min]	147 [min]
18°C	Measurement	74 [min]	103 [min]	146 [min]	270 [min]
	Simulation	73 [min]	94 [min]	135 [min]	254 [min]
21°C	Measurement	97 [min]	153 [min]	282 [min]	-
	Simulation	93 [min]	135 [min]	261 [min]	-

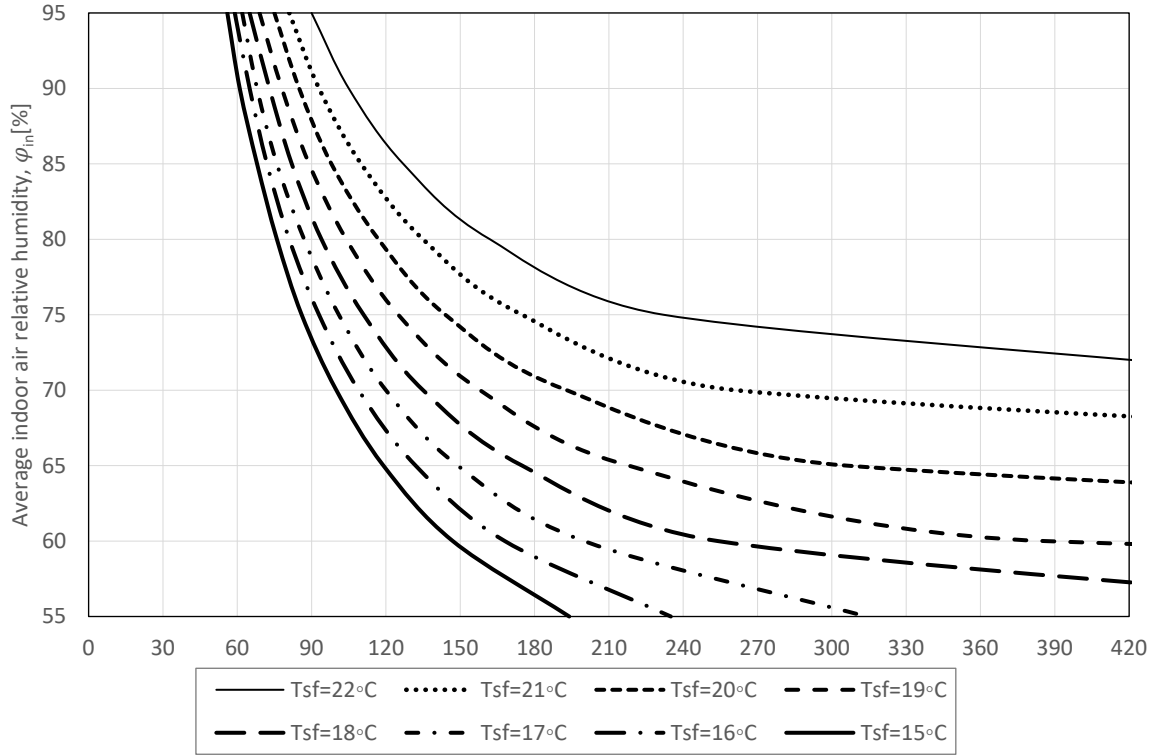


Figure 30. The required time charts of surface condensation development on the concrete layer

Figure 30 is the outcome of required time chart of surface condensation development. This chart can be utilized for air-conditioned space where the sensible cooling load is mainly covered by the TABS. For example, when predicting the required time of surface condensation development ($t_{required}$) under $T_{sf}=18^{\circ}\text{C}$ and $\varphi_{in}=65\%$, the chart indicates that approximately $t_{required}=175$ minutes for the concrete sample to develop the surface condensation. Based on the required time to develop surface condensation, the model predictive control framework can determine whether to operate the TABS or not, or to adjust the control input for the TABS (T_{sf}) for the following control horizon.

It should be noted that the average values of indoor conditions (average relative humidity under approximately 25°C indoor air temperature) are acceptable when referring to the above

charts, because the indoor air conditions are rarely constant in reality. The required time charts of surface condensation development are recommended for users who want brief understanding in time factor for the surface condensation development under specific indoor conditions, and thus to help them to control the surface condensation while TABS operation with relatively simple approach. When there is a significant fluctuation in indoor conditions that cannot be averaged, the dynamic simulation models should be utilized for the surface condensation prediction instead.

5.4. An MPC-based Surface Condensation Prevention Framework

As verified in Section 2.8, a longer control horizon ($>$ one hour) is essential to deal with both the time-delay in hygrothermal transfer and the indoor condition changes in advance. However, as the control horizon gets longer, the more significant prediction error it gets. Based on A. Afram et al. [41], choices of sampling time interval, control horizon, and prediction horizon affect the prediction accuracy, computational cost, and response time of model predictive control. Thus, sampling time interval, control horizon, and prediction horizon should be chosen considering all the performance aspects of model predictive control.

According to A. Afram et al. [41], the prediction horizon is defined by the length of time for which system output is computed by the dynamic models of MPC, whereas the control horizon refers to the length of time for which the control signal is computed. The sampling time interval is the time during which the control signal remains unchanged. In general, for slow processes in HVAC systems, the prediction horizon ranges between 5–48 hours, the control horizon ranges between 4–5 hours, and the sampling time interval ranges between 1–3 hours [61, 105, 106]. The control horizon is generally smaller than or equal to the prediction horizon while longer than or

equal to the sampling time interval. In most cases, the slow dynamics can be controlled typically by a longer prediction horizon of 24 hours and a slow sampling time interval of one hour.

To find the optimal control horizon for the proposed MPC-based surface condensation prevention framework, a sensitivity study was conducted. The cumulative probability of prediction error was plotted over the two weeks of simulation data with alternations of the control horizon (Figure 31). As shown in Figure 31, in general, the longer the control horizon, the bigger the absolute mean prediction error it gets. However, when we expand the absolute mean prediction error range up to 2 K, the differences in cumulative probability among control horizon options are reduced significantly. As addressed in Section 5.3, the safety factor approach was applied in the current MPC framework, which subtract surface temperature by 2 K before inputting it to the surface condensation prediction; this will allow even six hours to be acceptable (cumulative probability > 84.5%) as the control horizon for the current MPC framework. By having relatively longer control horizon of six hours, the proposed MPC-based surface condensation prevention framework can cope with slow and gradual hygrothermal response of concrete material measured

and verified in Section 5.3. As a result of the sensitivity study, one hour, six hours, and 24 hours were set to the sampling time interval, the control horizon, and the prediction horizon, respectively.

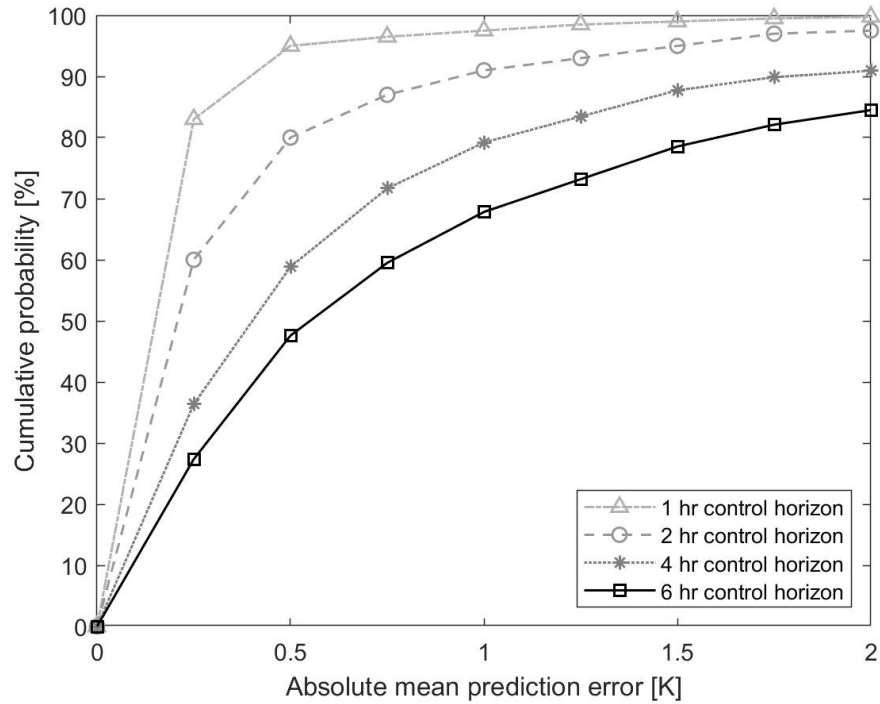


Figure 31. Sensitivity study of control horizon

Figure 32 shows a schematic MPC-based TABS operation for 24 hours under Atlanta, where has warm and partly humid climate conditions in summer. The sample time was set as one hour, the control horizon was set as six hours, and the prediction horizon was set as 24 hours; the objective function was solved over the entire prediction horizon of 24 hours until it finds the best control input for the TABS (T_{sf}) without violating any constraint. When the optimal control input is found, the MPC framework sends the input signal to the TABS for operation and steps forward six hours and repeats the searching process for the next control horizon.

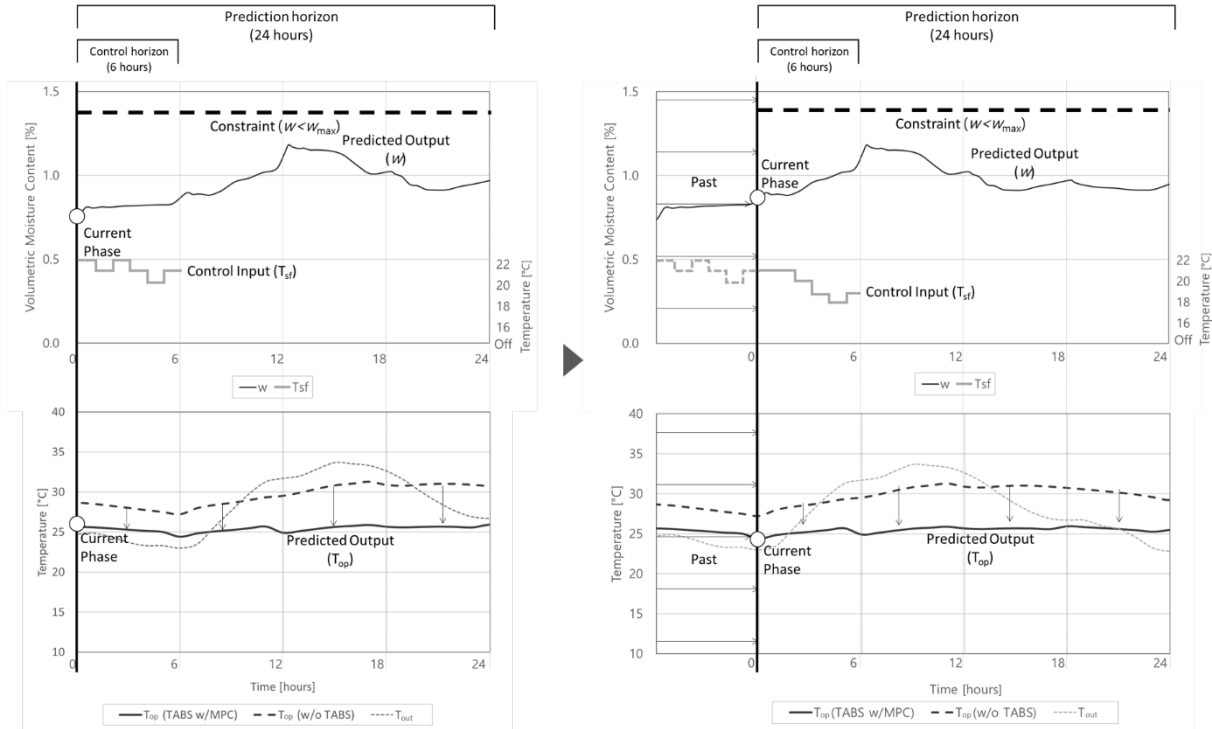


Figure 32. Schematic MPC-based TABS operation over the time horizon

The whole TABS operation procedure in conjunction with the MPC-based surface condensation prevention framework is shown in Figure 33. First, temperature and relative humidity changes in the construction layers are measured. Second, the dynamic model of construction layers is calibrated with the measured data to find the physical property values and the convective heat transfer coefficient. Third, the most feasible physical property values and the convective heat transfer coefficient are input to the dynamic model. Fourth, once the dynamic model of construction layers and buildings are coupled, the volumetric moisture content change in the construction layer is predicted in accordance with outdoor weather changes. Fifth, when the coupled dynamic model indicates a potential risk of developing surface condensation, the MPC framework will raise the surface temperature for the TABS to avoid the surface condensation.

Finally, this MPC-based TABS operation is iterated until it finds the best surface temperature to ensure not only condensation prevention but also thermal comfort and energy efficiency.

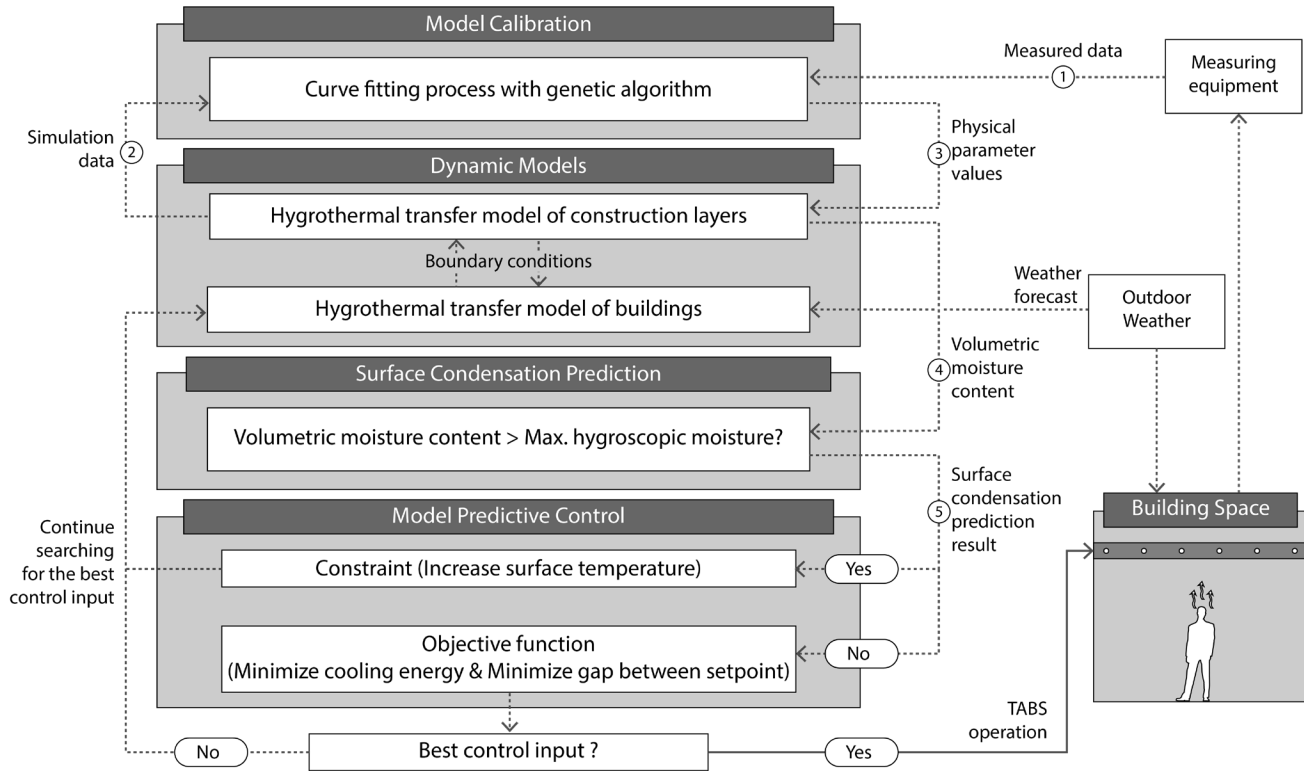


Figure 33. MPC-based TABS operation procedure

5.5. Site-specific Surface Condensation Prevention Performance

As presented in Section 4.5, the site-specific surface condensation prevention performances were estimated for total 845 regions in the U.S. based on “MPC condensation prevention performance index” (Eq. 27).

MPC condensation prevention performance index [%] =

$$\frac{\text{Hours of surface condensation on TABS (on/off)} - \text{Hours of surface condensation on TABS (MPC)}}{\text{Hours of surface condensation on TABS (on/off)}}$$

(27)

The estimation results of surface condensation prevention performances at each site in the United States were generated as geographic plot (Figure 34) using MATLAB. The size and opacity of the bubbles on the chart represent the extended TABS operable periods using the proposed MPC framework over the TABS operable periods using the on/off control. That is, the bigger and opaque bubbles denote that the proposed MPC-based surface condensation prevention framework is more effective in given locations, regarding surface condensation prevention while TABS is in operation.

As shown in Figure 34, in general, the proposed MPC-based surface condensation prevention framework is more effective in the climatic regions where has a partly warm and humid summer (Climate zone 3 –7 under Moist A or Marine C); however, the MPC framework gets less effective as climatic conditions are getting significantly warm and humid (Climate zone 1 –3 under Moist A). This is because the risk of developing surface condensation, while the TABS is in operation, is increasing significantly under such hot and humid climate regions where has relatively longer cooling period with less daily temperature fluctuation. Under these high risky conditions of developing surface condensation, the MPC framework will likely turning off the TABS to avoid surface condensation development and operates the sub-mechanical cooling system instead to control indoor hygrothermal conditions.

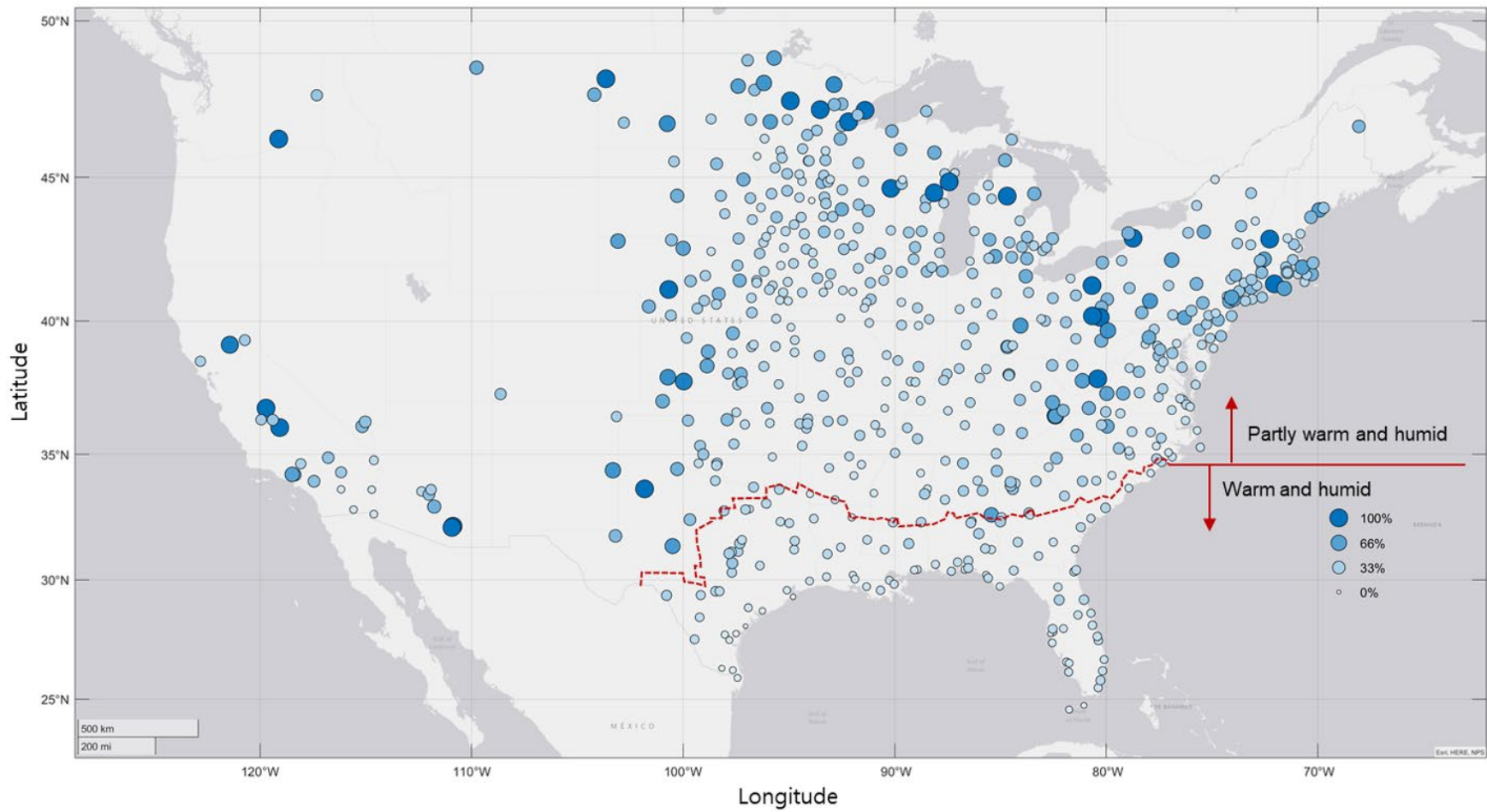


Figure 34. Geographic plot: surface condensation prevention performance using the MPC framework in the U.S.

5.6. Energy Savings and Cost Reduction by the MPC-based TABS Operation

Nine climate regions that have partly warm or hot, and humid summer (Table 11 in Section 4.6) were chosen from the IECC climate zones classification to test the performance of the proposed MPC-based surface condensation prevention framework. Under each climate zone condition, three cooling modes (mechanical ventilation cooling, TABS with on/off control, and TABS with MPC) were tested in a room of medium-size office building [100].

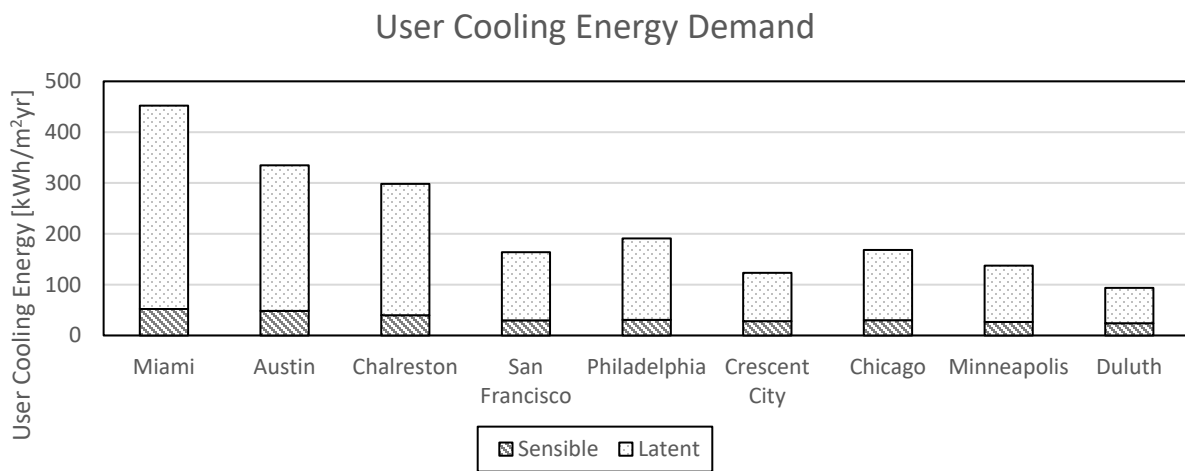


Figure 35. Annual user cooling energy demand for different climatic regions

Table 16. Annual user cooling energy demand for different climatic regions

IECC Climate Zone	Location	User sensible cooling energy [kWh/m ² yr]	User latent cooling energy [kWh/m ² yr]	Total user cooling energy [kWh/m ² yr]
1A	Miami	52.04	400.11	452.15
2A	Austin	48.31	286.48	334.79
3A	Charleston	39.92	258.19	298.10
3C	San Francisco	29.63	134.10	163.73
4A	Philadelphia	30.65	160.20	190.85
4C	Crescent City	28.27	95.05	123.32
5A	Chicago	30.01	138.10	168.11
6A	Minneapolis	26.66	110.67	137.33
7A	Duluth	23.91	69.64	93.55

At first, user sensible and latent cooling energy demands were calculated under each climatic region (Figure 35,). The dynamic modeling from 4.1 was used for user cooling energy demand calculation and the calculation results were validated with EnergyPlus results.

As shown in Figure 35, both sensible and latent cooling energy are getting greater as climatic conditions shift to warmer and more humid. As it can be seen from the chart, latent cooling energy demands for Miami (1A), Austin (2A), and Charleston (3A) account for more than 85 % of total annual user cooling energy demand. These three climatic regions are categorized as “Warm-Humid” area according to the IECC climate zone classification. Presumably, within these climatic zones, application of TABS will be challenging due to the high risk of developing surface condensation derived from the relatively high moisture content in ambient air. In contrast, Philadelphia (4A), Chicago (5A), Minneapolis (6A), and Duluth (7A), where has partly warm and humid climatic conditions during summer season, the operable periods for the TABS in such regions are expected to be extended governed by the proposed MPC-based surface condensation prevention framework. Besides, San Francisco (3C) and Crescent City (4C), where are defined as “Marine” area according to the IECC climate zone classification, are expected to show lower risk of developing surface condensation while operating the TABS for cooling.

Based on the annual user cooling energy demand, the site cooling energy for different cooling modes were calculated and the results are shown in Figure 36 a–b. To be complete with the site cooling energy calculation, cooling energy from compression chiller, energy for cooling tower, and distribution energy were calculated under each climatic condition for three different cooling modes: mechanical ventilation cooling, TABS with on/off control, and TABS with MPC. For the compression chiller cooling energy calculation, the user cooling energy demands (Figure 35) were divided by the coefficient of performance (COP) value of the compression chiller.

According to the references [107–110], the COP values for the conventional water-to-water compression chiller within medium-size office buildings were range from 3.5–4. For this study, the COP value of 3.5 water-to-water compression chillers was adopted for mechanical ventilation cooling mode while the COP value of 4.5 water-to-water compression chillers was applied for TABS cooling modes.

For the cooling tower energy calculation, we referred to the calculation procedure from the reference [111–113]. For the distribution energy calculation, different parameter values (e.g., specific heat capacity, density, efficiency, total pressure drop, etc.) were adopted for air-based mechanical ventilation cooling systems and water-based TABS cooling systems [8, 10, 112, 114]. Basically, the TABS were coupled with a sub-mechanical ventilation cooling system to be provided with the minimum required outdoor air and supplemental cooling when the TABS were inoperable due to the surface condensation risk. Then, based on the estimated TABS operable periods by each cooling mode (TABS with on/off control and TABS with MPC), the distribution energy for the TABS were determined. The parameter values adopted for the site cooling energy calculation can be found in Appendix D (Table 19).

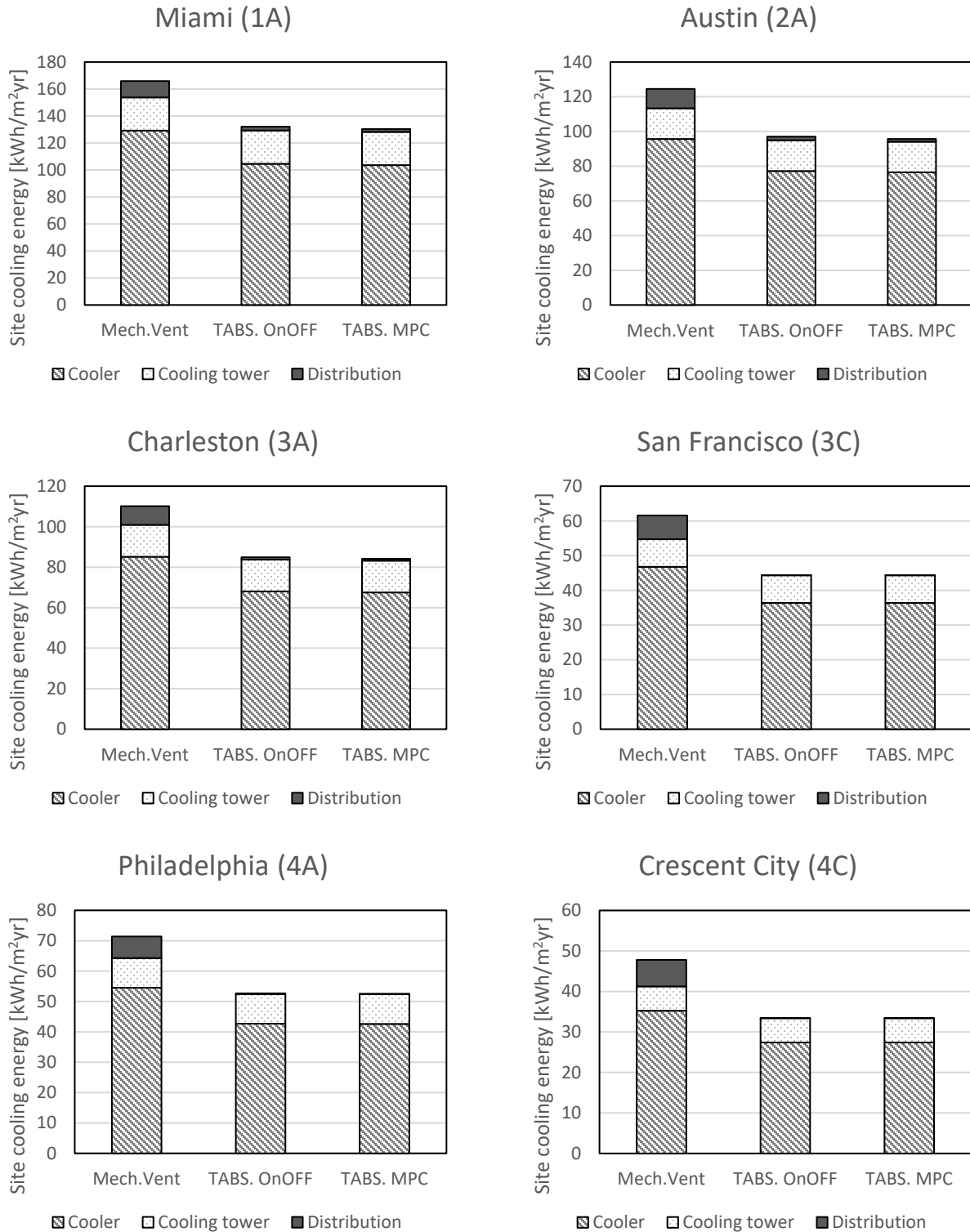


Figure 36-a. Annual site cooling energy for different climate regions (1A–4C)

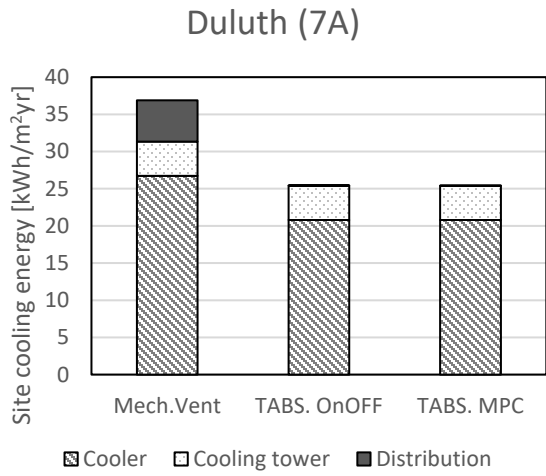
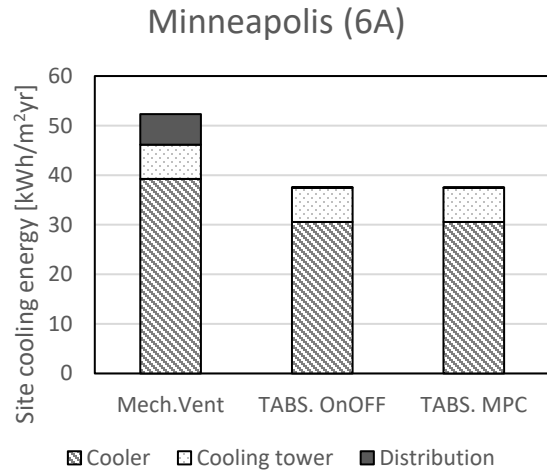
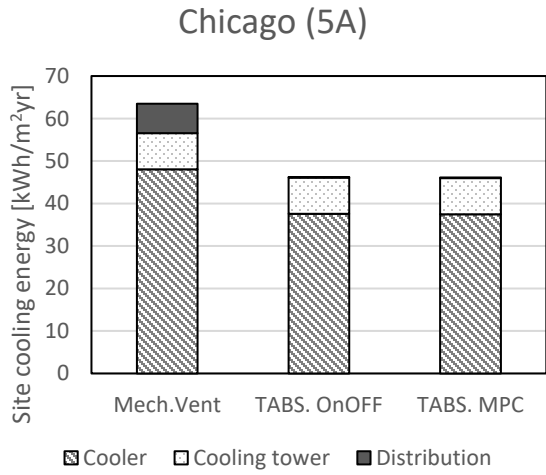


Figure 36-b. Annual site cooling energy for different climate regions (5A–7A)

Table 17. Annual site cooling energy for different climate regions and cooling modes

Mechanical ventilation cooling site energy				
Location	Cooler energy	Cooling tower	Distribution	Total
1A. Miami	129.18	24.62	12.06	165.86
2A. Austin	95.65	17.67	11.20	124.52
3A. Charleston	85.17	15.71	9.25	110.13
3C. San Francisco	46.78	7.94	6.87	61.59
4A. Philadelphia	54.53	9.79	7.10	71.42
4C. Crescent City	35.23	6.01	6.55	47.79
5A. Chicago	48.03	8.51	6.96	63.50
6A. Minneapolis	39.24	6.90	6.18	52.32
7A. Duluth	26.73	4.61	5.54	36.88
TABS with on/off control				
Location	Cooler energy	Cooling tower	Distribution	Total
1A. Miami	104.62	24.62	2.84	132.08
2A. Austin	77.22	17.67	2.14	97.03
3A. Charleston	68.02	15.71	1.18	84.92
3C. San Francisco	36.39	7.94	0.02	44.35
4A. Philadelphia	42.69	9.79	0.21	52.68
4C. Crescent City	27.40	6.01	0.02	33.43
5A. Chicago	37.57	8.51	0.17	46.25
6A. Minneapolis	30.58	6.90	0.08	37.56
7A. Duluth	20.80	4.61	0.02	25.43
TABS with MPC				
Location	Cooler energy	Cooling tower	Distribution	Total
1A. Miami	103.58	24.62	2.18	130.38
2A. Austin	76.42	17.67	1.57	95.66
3A. Charleston	67.53	15.71	0.90	84.15
3C. San Francisco	36.39	7.94	0.02	44.35
4A. Philadelphia	42.60	9.79	0.15	52.53
4C. Crescent City	27.40	6.01	0.02	33.43
5A. Chicago	37.48	8.51	0.12	46.11
6A. Minneapolis	30.56	6.90	0.06	37.52
7A. Duluth	20.79	4.61	0.02	25.42

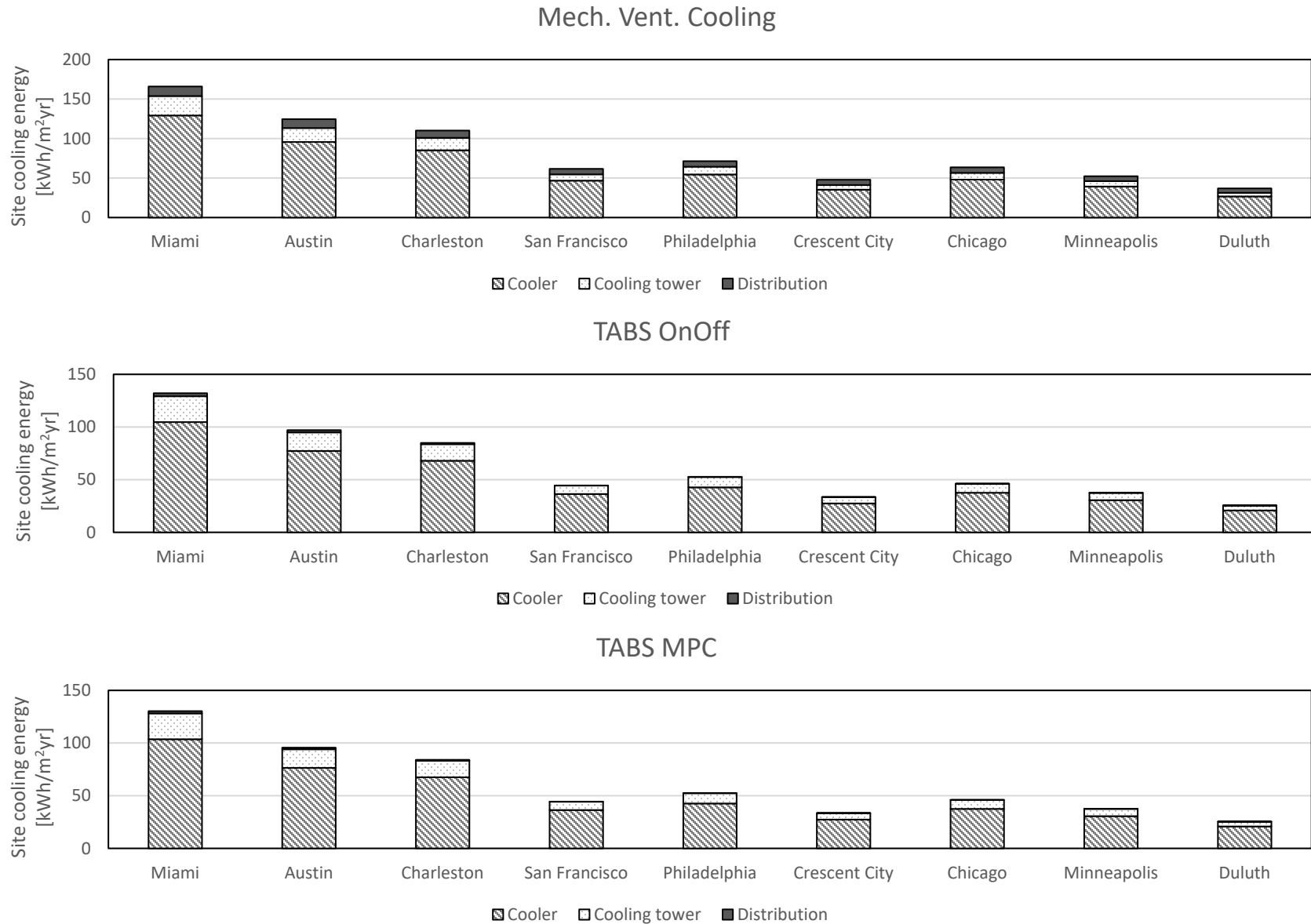


Figure 37. Annual site cooling energy for different cooling modes

As shown in Figure 35–36, regardless of climate zone, the TABS show notable cooling energy savings in comparison to the conventional mechanical ventilation cooling system. These energy savings were mainly derived from two factors: 1) the higher COP value of the TABS than that of the mechanical ventilation cooling system and 2) the type of distribution system. The higher COP value of the TABS was mainly derived from the effective ways of exchanging heat through the radiant cooling systems [8]. Thanks to this highly efficient heat exchange through the radiation [8], a supply water temperature for the radiant cooling systems can be higher than a supply air temperature for the forced air-based system to bring the same cooling effect to the occupants; having the supply water temperature (from the evaporator) close to the temperature of the condenser where waste heat is emitted, a coefficient of performance (COP) for the chillers can be increased [11]. Furthermore, if the condenser side is connected to a ground source loop or a cooling tower, the COP for the chillers can be increased significantly.

Additionally, because of much greater specific heat and density of water than air, the water-based cooling systems required much less distribution energy than the air-based cooling system. This lesser distribution energy demand for water-based cooling systems contributed to the overall energy savings for the TABS than the mechanical ventilation cooling systems.

Specifically, the MPC-based TABS operation achieved 21.4–31.1% cooling distribution energy savings over the mechanical ventilation cooling systems and achieved 15.0–33.0% cooling distribution energy savings over the on/off control depending on the climatic regions (except for the Marine climatic regions). Especially, under weather condition where has partly warm and humid summer (3C. San Francisco, 4A. Philadelphia, 4C. Crescent City, 5A. Chicago, 6A. Minneapolis, and 7A. Duluth), cooling energy savings with the TABS were greater than the other three cities with significantly warm and humid summer (1A. Miami, 2A. Austin, and 3A.

Charleston). These notable energy savings were derived from the longer extended operable periods for the TABS with guidance from the MPC framework (Appendix C. Figure 45–80).

As shown in Figure 38, the trends in cooling operational cost between the cooling modes were similar to the site cooling energy results (Figure 37). However, based on the Table 11, cheaper electricity cost for Austin (7.93 ¢/kWh) and Philadelphia (8.65 ¢/kWh) compared to the other cities (Miami: 9.47 ¢/kWh, Charleston 9.94 ¢/kWh, San Francisco 17.64 ¢/kWh, Crescent City 17.64 ¢/kWh, Chicago 9.14 ¢/kWh, Minneapolis 10.04 ¢/kWh, and Duluth 10.04 ¢/kWh) led to smaller cost savings. In general, the longer the operable periods for TABS, the lower the cooling energy and the electricity cost it took than the conventional mechanical ventilation cooling systems. Under partly warm and humid climatic conditions, the on/off control systems tended to turn off the TABS as long as the surface condensation risk was detected. In contrast, MPC adjusted the right amount of energy input in a gradient manner that can maintain indoor thermal comfort without developing surface condensation. Thus, MPC could extend the overall operable periods for the TABS more than the on/off control, which in turn leads to an additional cooling energy and electricity cost saving for each city.

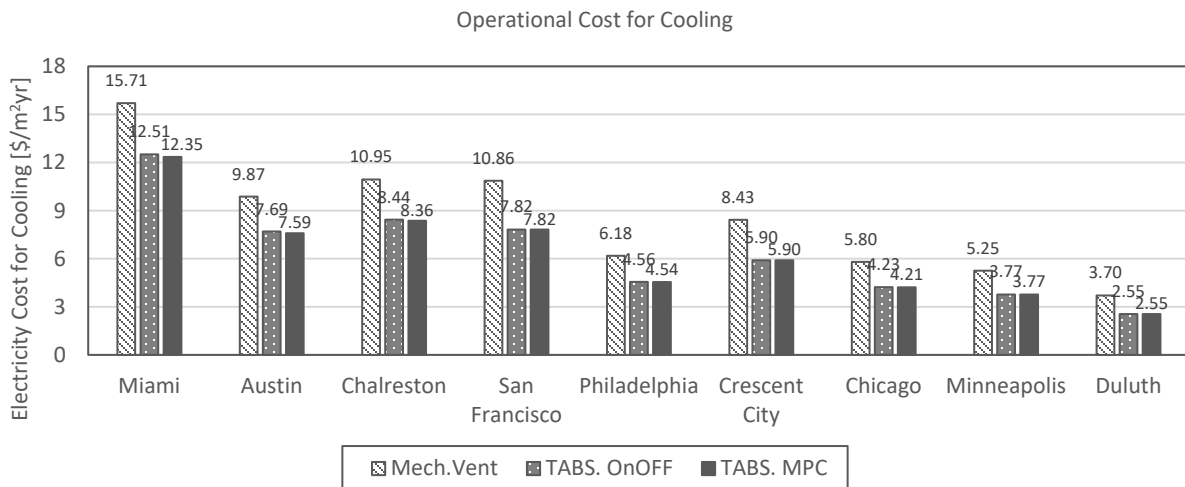


Figure 38. Annual cooling operational cost for different climate regions and cooling modes

Table 18. Annual cooling operational cost for different climate regions and cooling modes

Location	Mechanical ventilation cooling operational cost [\$/m ² yr]	TABS with on/off control operational cost [\$/m ² yr]	TABS with MPC operational cost [\$/m ² yr]
1A. Miami	15.71	12.51	12.35
2A. Austin	9.87	7.69	7.59
3A. Charleston	10.95	8.44	8.36
3C. San Francisco	10.86	7.82	7.82
4A. Philadelphia	6.18	4.56	4.54
4C. Crescent City	8.43	5.90	5.90
5A. Chicago	5.80	4.23	4.21
6A. Minneapolis	5.25	3.77	3.77
7A. Duluth	3.70	2.55	2.55

In this section, step-by-step model predictive control-based surface condensation prevention framework development was addressed and efficacy of the proposed MPC framework for the TABS operation was estimated in terms of surface condensation prevention performance, energy savings potential, and operational cost. The results show that the proposed MPC-based surface condensation prevention framework was more effective in partly warm and humid climatic regions while the MPC framework gets less effective as climatic conditions are getting significantly warm and humid. Regardless of climate zone, the TABS showed notable cooling energy savings when it is compared to the conventional mechanical ventilation cooling system. The MPC-based TABS operation achieved 21.4–31.1% cooling distribution energy savings over the mechanical ventilation cooling systems and saved 15.0–33.0% cooling distribution energy over the on/off control depending on the climatic regions. When it comes to operational cost, the longer the operable periods for TABS, the lower the cooling energy and the electricity cost it took than the conventional mechanical ventilation cooling systems.

CHAPTER 6. Conclusion

6.1. Highlights

- This study proposes Model Predictive Control (MPC)-based surface condensation prevention framework that reduces the surface condensation occurrence risk even when the thermo-active building system is in operation under warm and humid climate regions.
- Development procedure of the MPC framework presents integration between numerical hygrothermal transfer dynamic models and physical measurements, which allows for more accurate surface condensation prediction.
- This study demonstrates the proposed framework's site-specific surface condensation prevention performance for the thermo-active building system under most climate regions in the U.S., by which designers and planners can determine the applicability of the proposed framework to their projects.
- The results of this study show energy savings potential and operational cost reduction (without compromising occupants' thermal comfort) with thermo-active building system over conventional mechanical ventilation cooling system; additional energy savings potential and operational cost reduction were analyzed by extending the operable periods for the thermo-active building systems using the proposed MPC-based surface condensation prevention framework.

6.2. Conclusions

This study proposes a novel model predictive control (MPC)-based surface condensation prevention framework that can accurately predict the occurrence of surface condensation for TABS. In contrast to the classical MPC that adopts short-term control horizon, we propose a longer control horizon in order to deal with both the time-delay in hygrothermal transfer and the indoor condition changes in advance.

In the process of dynamic model development, heat and moisture transfer behaviors in the concrete sample were tested in a chamber, and the measured data were used for dynamic model calibration. The prediction accuracy of the dynamic model was improved (the MSE dropped by 47.2%) after the model calibration, and the most feasible physical property values and heat transfer coefficient for the concrete sample were derived via the curve fitting process.

Our results show that when the calibrated dynamic model of construction layers and dynamic model of buildings are coupled, the risk of surface condensation development can be predicted in relation to surface temperature of the TABS and indoor condition change. Adopting the volumetric moisture content as the condensation risk indicator instead of the surface relative humidity level allows the moisture diffusion process from the past to the current stage to be considered, thus enabling more accurate surface condensation prediction.

For the surface condensation prevention performance (Figure 39–40), in general, the proposed MPC framework is more effective in climatic regions where has a partly warm and humid summer. In contrast, the MPC framework gets less effective as climatic conditions are getting significantly hot and humid. This is because the risk of developing surface condensation is increasing significantly under such hot and humid climate regions where has a relatively longer cooling period with less daily temperature fluctuation.

As shown in the charts (Figure 41–42), the MPC-based TABS operation achieved 15.0–33.0% cooling distribution energy savings over the on/off control depending on the climatic regions (except for the Marine climatic regions). These distribution energy savings were mainly derived from the extended operable periods for the TABS by the MPC framework. However, too short cooling periods of Minneapolis and Duluth led to smaller energy savings.

The operational cost reductions by the MPC-based TABS operation (Figure 43–44) were plotted for each city. As shown in these figures, the trends in cooling operational cost between the two cooling modes were similar to the site cooling energy results. In general, the longer the operable periods for the TABS, the lower the cooling energy and the electricity cost they use than the conventional mechanical ventilation cooling systems. However, the cheaper electricity cost for Austin (7.93 ¢/kWh) and Philadelphia (8.65 ¢/kWh) compared to the other cities led to smaller cost savings than expected.

Because the MPC-based surface condensation prevention framework continually controls the surface condensation when the TABS is in operation, potential damage to the building construction layers, such as corrosion of the building fabric or deterioration of insulation can be avoided. Avoidance of damages in building envelopes will extend the repair cycle for each building construction layer, which in turn leads to total maintenance cost savings for buildings.

Moreover, the mold growth-driven health problems like allergic rhinitis can be avoided by continuous surface condensation control by the MPC framework. With the one day ahead surface condensation prediction by the MPC framework, the potential risk of failing to detect surface condensation can be eliminated, which will contribute to the prevention of mold growth in building construction layers.

In addition, the proposed MPC-based surface condensation prevention framework will broaden the use of the TABS even in warm and humid climate regions. Based on the global radiant heating and cooling systems market reports [80], analysts forecast the global market for radiant cooling systems, including TABS, to grow at a compound annual growth rate of 7.14%, which contributes to 1.63 billion dollars in incremental growth during the period 2018–2022. Given the growing demand for the TABS, the proposed MPC framework clearly meets an important need.

By controlling the potential risk of surface condensation development, it can extend the use of the TABS to areas in which climate conditions had made them infeasible.

Furthermore, the broadened TABS application in warm and humid climate regions will provide more freedom for architectural designers. As I mentioned in Section 1.2., many great architectures could have been preserved their integrity or have maintained their initial design intention thanks to the TABS or the surface radiant cooling systems.

Warm and humid

Partly warm and humid

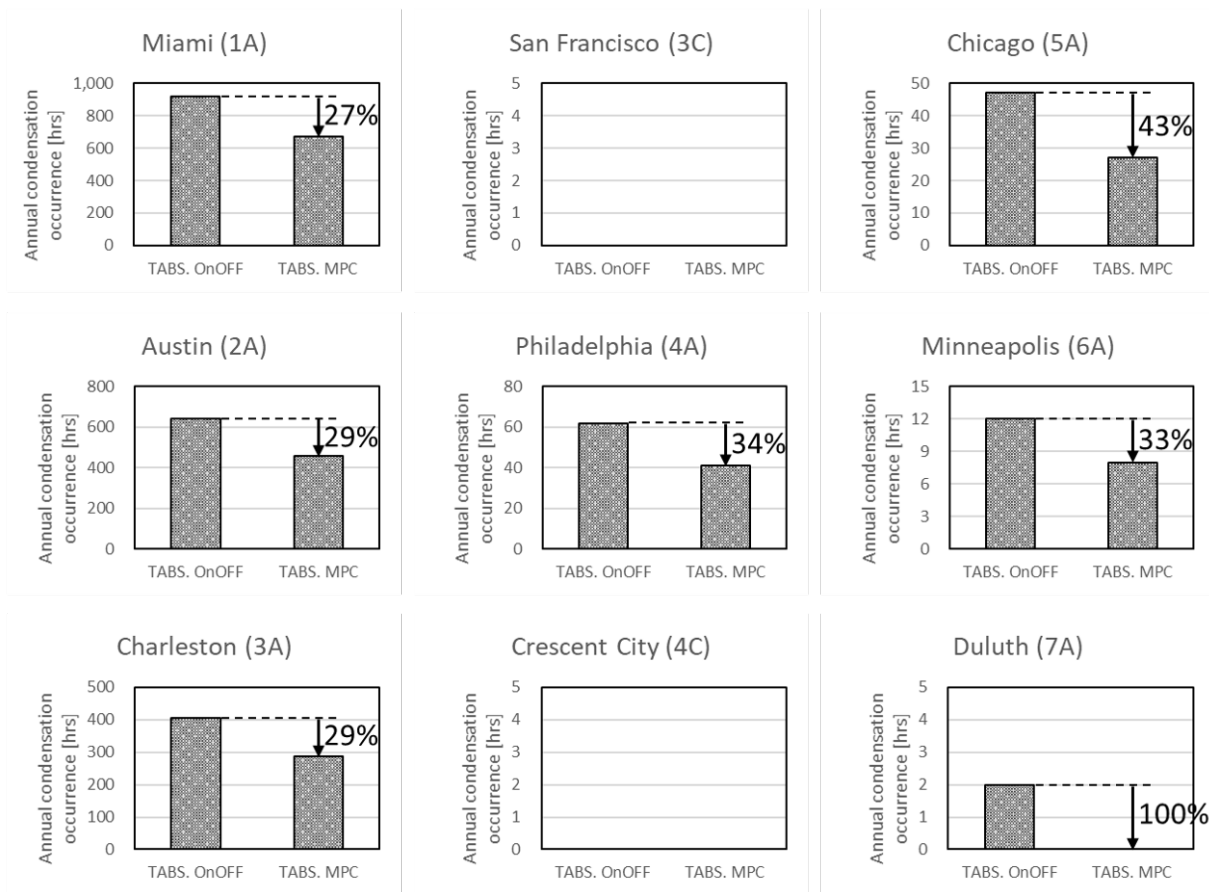


Figure 39. Site-specific surface condensation prevention performance



Figure 40. Site-specific surface condensation prevention performance (Geographic plot)

Warm and humid

Partly warm and humid

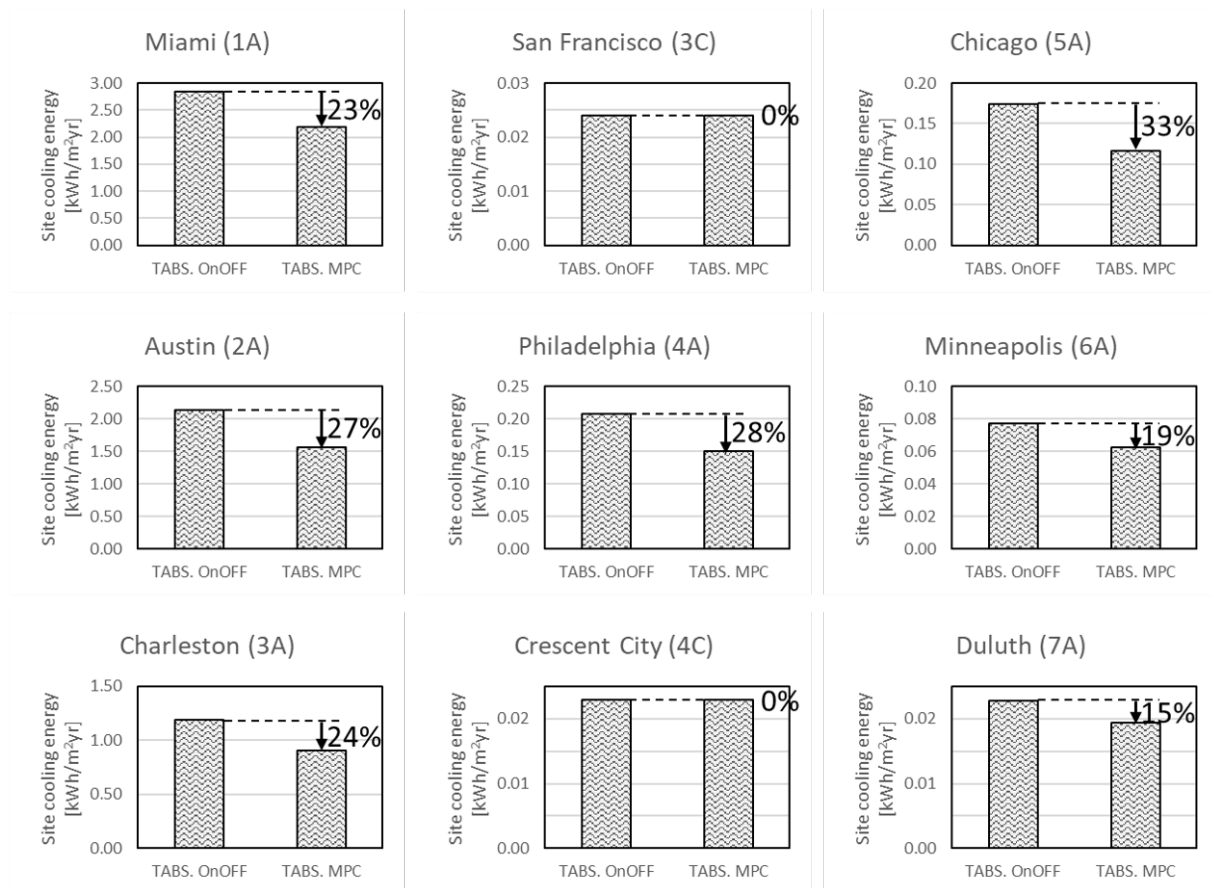


Figure 41. Site-specific distribution energy savings potential

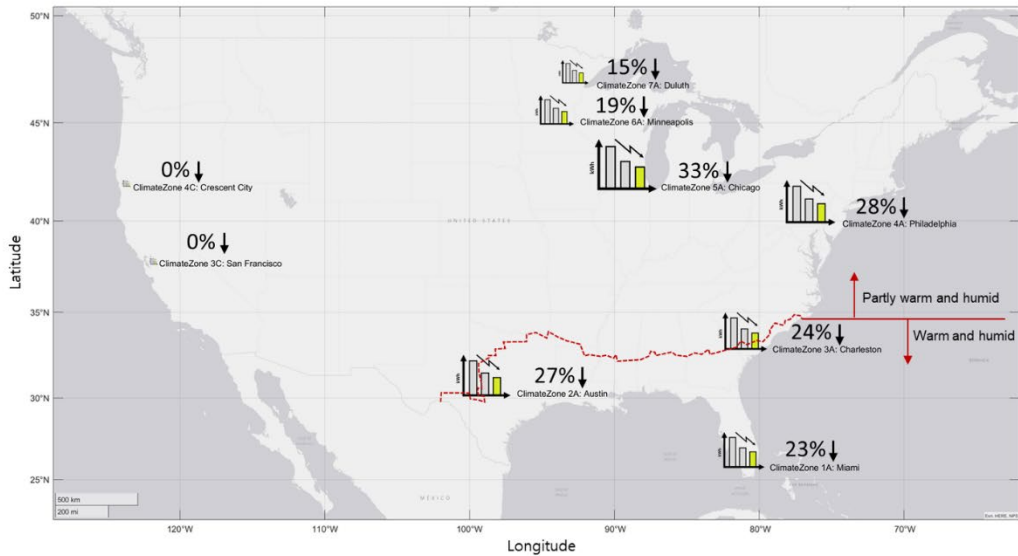


Figure 42. Site-specific distribution energy savings potential (Geographic plot)

Warm and humid

Partly warm and humid

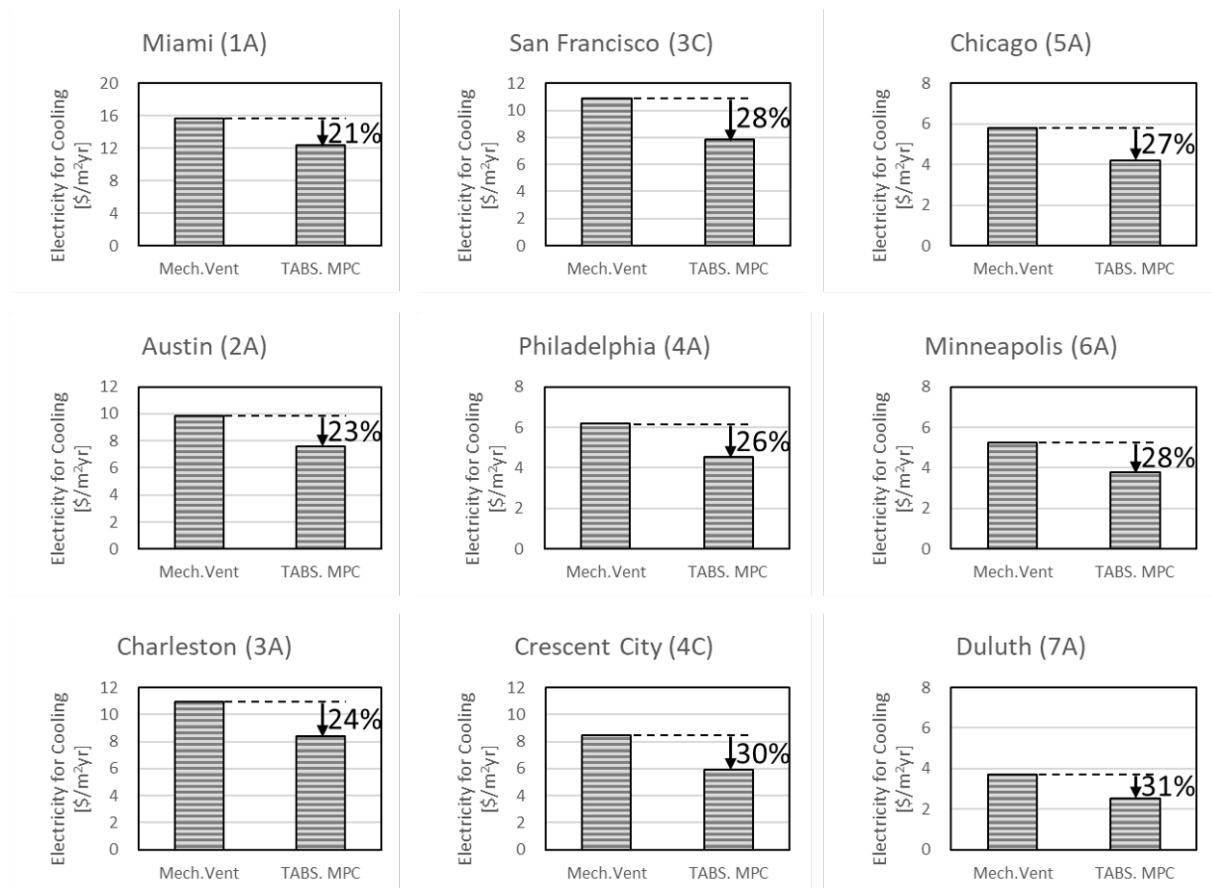


Figure 43. Site-specific operational cost reduction



Figure 44. Site-specific operational cost reduction (Geographic plot)

6.3. Limitations

First, the applicability of the proposed MPC-based surface condensation prevention framework on the TABS needs to be validated in a real building. Given an actual mid-size office building that adopts the TABS as its major cooling systems, I can test the proposed MPC framework in everyday working indoor conditions with partly warm and humid climatic weather. Also, the site cooling energy use and the total operational cost to maintain indoor thermal comfort without developing the surface condensation can be estimated with sensors and metering systems.

Second, the current dynamic models in the proposed MPC framework do not provide precise mean radiant temperature estimation in relation to the occupant's position. When we cool indoor space with the TABS, not only indoor air temperature but also the mean radiant temperature is influential for occupants' thermal comfort. Because of this combined effect of operative temperature on occupants' thermal comfort, we set operative temperature as an indicator for thermal comfort rather than the indoor air temperature in the current study. As I addressed in Section 4.4, the measuring point for the mean radiant temperature was always assumed to be the occupant's eye level who is seated in the middle of the space. However, when occupants are not sitting in the middle of the space but standing at the corner of the space, the surface radiant cooling effect from the TABS would be completely different, which in turn leads to the different estimation of the mean radiant temperature. Thus, for more precise operative temperature estimation, the MPC framework may include the mean radiant temperature calculation that considers both the volume of the space and the exact positioning of occupants.

6.4. Future Works

Besides the partial theoretical model approach, data-driven models are also widely used for the dynamic model of MPC. Several months' data sets are required for training the data-driven model. In general, 60 % of collected data is utilized for the training and the rest are used for the validation. After the data-driven model has been trained and validated with the massive data sets, the model can be adopted as a dynamic model for MPC. With the developed data-driven model, the surface condensation risk can be predicted during the TABS operation, thus the MPC framework can determine the best control input for the TABS. These two different dynamic modeling approaches (partial theoretical model and data-driven model) are then applied in the TABS operation to compare the performance in surface condensation prevention, energy savings potential, maintaining thermal comfort, and calculation time.

Also, I envision applying the proposed MPC framework for preventing surface condensation in large spaces, such as the airport. Suppose that a large space of the airport is covered by a fiberglass membrane. When the indoor moist air is floated by buoyancy effect and suddenly meets the cold surface of the roof membrane, there is a high risk of developing surface condensation. Currently, many airports run high-speed fans constantly on roof membranes to prevent surface condensation development. This redundant fan energy can be saved with the proposed MPC framework.

Furthermore, I envision expanding the applicability of the proposed MPC framework in harsher climate regions like East Asia, where has much more humid and warm conditions. Recently, hydronic-based surface radiant cooling systems have a focus of much attention from the planners and designers in East Asia. The application of the proposed MPC framework in such climatic regions might be challenging but worth exploring.

REFERENCES

- [1] Y. Saheb, Building energy efficiency policies: a pillar for past and future low-carbon development, Rio+20 conf. (2012)
- [2] O. Edenhofer, R. Pichs-Madruga, Y. Sokona, E. Farahani, S. Kadner, K. Seyboth, A. Adler, I. Baum, S. Brunner, P. Eickemeier, B. Kriemann, J. Savolainen, S. Schlömer, C. von Stechow, T. Zwickel, J.C. Minx, Climate Change 2014: Mitigation of Climate Change. Cambridge University Press. (2014)
- [3] M. Erlandsson, M. Borg, Generic LCA-methodology applicable for building, construction and operation services-today practice and development needs, *Build. Environ.* 38 (7) (2003) 919–938
- [4] ASHRAE, ANSI/ASHRAE Standard 55–2010 Thermal Environmental Conditions for Human Occupancy
- [5] H. Shi, Q. Chen, Building energy management decision-making in the real world: A comparative study of HVAC cooling strategies, *Journal of Build. Engineer.* 33 (2021) 101869
- [6] ASHRAE. 2017 ASHRAE Handbook – Fundamentals
- [7] R.A. Meierhans, Room air conditioning by means of overnight cooling of the concrete ceiling, *ASHRAE Trans.* 102 (1996) 693–697
- [8] Uponor, Radiant Cooling Design Manual, Embedded Systems for Commercial Applications (2013)
- [9] M. Schmelas, T. Feldmann, E. Bollin, Adaptive predictive control of thermo-active building systems (TABS) based on a multiple regression algorithm, *Energy Build.* 103 (2015) 14–28
- [10] ASHRAE, ANSI/ASHRAE Standard 62.1–2016 Ventilation for Acceptable Indoor Air Quality
- [11] B. Olesen, Thermo active building systems using building mass to heat and cool, *ASHRAE Journal.* 54 (2012) 44–52
- [12] J. Babiak, B.W. Olesen, D. Petráš, Low-temperature heating and high-temperature cooling, REHVA, Brussels (2009)
- [13] J. Romani, A. de Gracia, L.F. Cabeza, Simulation and control of thermally activated building systems (TABS), *Energy Build.* 127 (2016) 22-42.
- [14] S.A. Kalogirou, G. Florides, S. Tassou, Energy analysis of building employing thermal mass in Cyprus. *Renew. Energy.* 27 (2002) 353-368.
- [15] K. Moe, *Thermally Active Surfaces in Architecture.* Princeton Architectural Press (2010)
- [16] D. Woo, L. Junghans, Framework for model predictive control (MPC)-based surface condensation prevention for thermo-active building systems (TABS), *Energy. Build.* (2020) 109898
- [17] U.S. Department of Homeland Security FEMA, Dealing with mold and mildew in your flood-damaged home

- [18] L. Bellia, F. Minichiello, A simple evaluator of building envelope moisture condensation according to a European Standard, *Build. Environ.* 38 (2003) 457–468.
- [19] A.N. Karagiozis, J. Lstiburek, A. Desjarlais, Scientific Analysis of Vapor Retarder Recommendations for Wall Systems Constructed in North America, *ASHRAE Journal* (2007)
- [20] T. Arends, P. Ruijten, L. Pel, Moisture-induced bending of an oak board exposed to bilateral humidity fluctuations, *Journal of Build. Engineer.* 27 (2020) 100957
- [21] U.S. Department of Energy, 5.C.2.1 Vapor Barrier Journal Paper
- [22] International Code Council, Vapor Retarders: Reducing Moisture Risk in Frame Walls, (2015)
- [23] J. Toman, A. Vimrova, R. Cerny, Long-term on-site assessment of the hygrothermal performance of interior thermal insulation system without a water vapor barrier, *Energy. Build.* 41 (2009) 51–55
- [24] J. Langmans, R. Klein, S. Roels, Hygrothermal risks of using exterior air barrier systems for highly insulated lightweight walls: A laboratory investigation, *Build. Environ.* 56 (2012) 192–202
- [25] T. K. Hansen, S.P. Bjarløv, R.H. Peuhkuri, M. Harrestrup, Long term in situ measurements of hygrothermal conditions at critical points in four cases of internally insulated historic solid masonry walls, *Energy. Build.* 172 (2018) 235–248
- [26] T. Ojanen, H. Viitanen, R. Peuhkuri, Modeling of mold growth in building envelopes, *Annex 41* (2007)
- [27] E. Vereecken, L. Van Gelder, H. Janssen, S. Roels, Interior insulation for wall retrofitting - A probabilistic analysis of energy savings and hygrothermal risks, *Energy. Build.* 89 (2015) 231–244
- [28] Z. Pasztory, P.N. Peralta, S. Molnar, I. Peszlen, Modeling the hygrothermal performance of selected North American and comparable European wood-frame house walls, *Energy. Build.* 49 (2012) 142–147
- [29] S.J. Chang, S. Wi, S.G. Kang, S. Kim, Moisture risk assessment of cross-laminated timber walls: Perspectives on climate conditions and water vapor resistance performance of building materials, *Build. Environ* 168 (2020) 106502
- [30] K. Sedlbauer, Prediction of mold growth by hygrothermal calculation, *Journal of Thermal Env. Build.* 25 (2002) 321–336
- [31] T.S. Rodgers. Preventing condensation in insulated structures, *Arch. Rec.* 83 (1938) 109–119
- [32] F.B. Rowley, A theory covering the transfer of vapour through materials, *ASHVE trans.* (1939)
- [33] F.B. Rowley, A.B. Algren, C.E. Lund, Condensation of moisture and its relation to building construction and operation. *ASHVE Trans.* (1939)
- [34] B.H. Vos, E. Coleman, Condensation in structures. Report nr BI–67–33/23. TNO–IBBC (1967)
- [35] H.M. Künzle, Simultaneous Heat and Moisture Transport in Building Components: One- and Two-Dimensional Calculation Using Simple Parameters (1995)
- [36] A.V. Luikov, Heat and Mass Transfer in Capillary-Porous Bodies, Pergamon Press, Oxford, 1966
- [37] J.R. Philip, D.A. de Vries, Moisture movement in porous materials under temperature gradients, *Trans. Am. Geophys. Union* 38 (1957) 222–232
- [38] K.A. Antonopoulos, C. Tzivanidis, Numerical solution of unsteady three-dimensional heat transfer during space cooling using ceiling-embedded piping, *Energy* 22 (1997) 59–67
- [39] Y. Liu, Y. Wang, D. Wang, J. Liu, Effect of moisture transfer on internal surface temperature, *Energy Build.* 60 (2013) 83–91

- [40] S. Petersen, K.W. Bundgaard, The effect of weather forecast uncertainty on a predictive control concept for building systems operation, *Appl. Energy* 116 (2014) 311–321
- [41] A. Afram, F. Janabi-Sharifi, Theory and applications of HVAC control systems – A review of model predictive control (MPC), *Build. Environ.* 72 (2014) 343–355
- [42] Y.G. Wang, Z.G. Shi, W.J. Cai, PID autotuner and its application in HVAC systems. Proceedings of the 2001 American Control Conf. Arlington, Virginia, USA (2001) 2192–2196
- [43] T.I. Salsbury, A survey of control technologies in the building automation industry, Proceedings of the IFAC 16th world Congr. Prague, Czech Republic (2005) 1396
- [44] F. Tahersima, J. Stoustrup, H. Rasmussen, P.G. Nielsen, Thermal analysis of an HVAC system with TRV controlled hydronic radiator. In: *Conf Autom Sci Eng (CASE)*. Toronto, Ontario, Canada: IEEE (2010) 756–61
- [45] H. Moradi, M. Saffar-Avval, F. Bakhtiari-Nejad, Nonlinear multivariable control and performance analysis of an air-handling unit. *Energy Build* (2011) 43, 805–13
- [46] M. Anderson, P. Young, D. Hittle, C. Anderson, J. Tu, D. Hodgson, MIMO robust control for HVAC systems. *IEEE Tran Control Syst Technol* (2008) 16, 475–83
- [47] I. Hazyuk, C. Ghiaus, D. Penhouet, Optimal temperature control of intermittently heated buildings using Model Predictive Control: Part II - Control algorithm *Build. Environ.* 51 (2012) 388–394
- [48] G. Serale, M. Fiorentini, A. Capozzoli, D. Bernardini, A. Bemporad, Model Predictive Control (MPC) for Enhancing Building and HVAC System Energy Efficiency: Problem Formulation, Applications, and Opportunities. *Energies* 11 (2018), 631–665
- [49] Y. Xi, D. Li, S. Lin, Model Predictive Control-Status and Challenges, *Acta Automatica Sinica*
- [50] S. Caraman, M. Sbarciog, M. Barbu, Predictive control of a wastewater treatment process, *International Journal of Computers, Communications, and Control* (2007) 132–142
- [51] H. Huang, L. Chen, E. Hu, A new model predictive control scheme for energy and cost savings in commercial buildings: An airport terminal building case study, *Build. Environ.* 89 (2015) 203–216
- [52] Y. Yu, V. Loftness, D. Yu, Multi-structural fast nonlinear model-based predictive control of a hydronic heating system, *Build. Environ.* 69 (2013) 131–148
- [53] H.C. Spindler, L.K. Norford, Naturally ventilated and mixed-mode buildings Part II: Optimal control, *Build. Environ.* 44 (2009) 750–761
- [54] P. May-Ostendorp, G.P. Henze, C.D. Corbin, B. Rajagopalan, C. Felsmann, Model-predictive control of mixed-mode buildings with rule extraction, *Build. Environ.* 46 (2011) 428–437
- [55] X. Zhang, S. Tan, G. Li, Development of an ambient air temperature prediction model, *Energy Build.* 73 (2014) 166–170
- [56] P.D. Morosan, R. Bourdais, D. Dumur, J. Buisson, Building temperature regulation using a distributed model predictive control, *Energy Build.* 42 (2010) 1445–1452
- [57] R.Z. Freire, G.H.C. Oliveira, N. Mendes, Predictive controllers for thermal comfort optimization and energy savings, *Energy Build.* 40 (2008) 1353–1365
- [58] F. Ascione, N. Bianco, C. de Stasio, G.M. Mauro, G.P. Vanoli, Simulation-based model predictive control by the multi-objective optimization of building energy performance and thermal comfort, *Energy Build.* 111 (2016) 131–144
- [59] J.D. Álvarez, J.L. Redondo, E. Camponogara, J. Normey-Rico, M. Berenguel, P.M. Ortigosa, Optimizing building comfort temperature regulation via model predictive control, *Energy Build.* 57 (2013) 361–372

- [60] X. Li, J. Wen, Review of building energy modeling for control and operation, *Renew. Sust. Energy Rev.* 37 (2014) 517–537
- [61] J. Široky, F. Oldewurtel, J. Cigler, S. Prívará, Experimental analysis of model predictive control for an Energy efficient building heating system, *Appl. Energy* 88 (2011) 3079–3087
- [62] F. Oldewurtel, A. Parisio, C.N. Jones, D. Gyalistras, M. Gwerder, V. Stauch, B. Lehmann, M. Morari, Use of model predictive control and weather forecasts for Energy efficient building climate control, *Energy Build.* 45 (2012) 15–27
- [63] J.J. Bloem, *System Identification Applied to Building Performance Data*, Joint Research Centre (1994)
- [64] X. Xu, Z. Huang, X. Zhang, Z. Li, A novel humidity measuring method based on dry-bulb temperatures using artificial neural network, *Build. Environ.* 139 (2018) 181–188
- [65] L. Mba, P. Meukam, A. Kemajou, Application of artificial neural network for predicting hourly indoor air temperature and relative humidity in modern building in a humid region, *Energy Build.* 121 (2016) 32–42
- [66] M. Taki, Y. Ajabshirchi, S.F. Ranjbar, A. Rohani, M. Matloobi, Heat transfer and MLP neural network models to predict inside environment variables and Energy lost in a semi-solar greenhouse, *Energy Build.* 110 (2016) 314–329
- [67] H. Huang, L. Chen, E. Hu, A neural network-based multi-zone modeling approach for predictive control system design in commercial buildings, *Energy Build.* 97 (2015) 86–97
- [68] Y.T. Chae, R. Horesh, Y. Hwang, Y.M. Lee, Artificial neural network model for forecasting sub-hourly electricity usage in commercial buildings, *Energy Build.* 111 (2016) 184–194
- [69] C. Deb, L.S. Eang, J. Yang, M. Santamouris, Forecasting diurnal cooling energy load for institutional buildings using Artificial Neural Networks, *Energy Build.* 121 (2016) 284–297
- [70] J.W. Moon, S. Yoon, S. Kim, Development of an artificial neural network model based thermal control logic for double skin envelopes in winter, *Build. Environ.* 61 (2013) 149–159
- [71] G. Ge, F. Xiao, S. Wang, Neural network-based prediction method for preventing condensation in chilled ceiling systems, *Energy Build.* 45 (2012) 290–298
- [72] V. Congradac, F. Kulic, Recognition of the importance of using artificial neural networks and genetic algorithms to optimize chiller operation, *Energy Build.* 47 (2012) 651–658
- [73] I. Hazyuk, C. Ghiaus, D. Penhouet, Optimal temperature control of intermittently heated buildings using Model Predictive Control: Part I - Building modeling. *Build. Environ.* 51 (2012) 379–387
- [74] T. Berthou, P. Stabat, R. Salvazet, D. Marchio, Development and validation of a gray box model to predict thermal behavior of occupied office buildings, *Energy Build.* 74 (2014) 91–100
- [75] B. Lehmann, D. Gyalistras, M. Gwerder, K. Wirth, S. Carl, Intermediate complexity model for Model Predictive Control of Integrated Room Automation, *Energy Build.* 58 (2013) 250–262
- [76] H.B. Gunay, J. Bursill, B. Huchuk, W. O'Brien, I. Beausoleil-Morrison, Shortest-prediction-horizon model-based predictive control for individual offices, *Build. Environ.* 82 (2014) 408–419
- [77] Y. Zhao, Y. Lu, C. Yan, S. Wang, MPC-based optimal scheduling of grid-connected low energy buildings with thermal energy storages, *Energy Build.* 86 (2015) 415–426
- [78] M. Schmelas, T. Feldmann, E. Bollin, Adaptive predictive control of thermo-active building systems (TABS) based on a multiple regression algorithm, *Energy Build.* 103 (2015) 14–28

- [79] R. De Coninck, L. Helsen, Practical implementation and evaluation of predictive model control for an office building in Brussels, *Energy Build.* 111 (2016) 290–298
- [80] TechNavio, Global Radiant Heating and Cooling Systems Market 2018-2022 (2018)
- [81] P. Bacher, H. Madsen, Identifying suitable models for the heat dynamics of buildings, *Energy Build.* 43 (2011) 1511–1522
- [82] S. Privara, J. Cigler, Z. Váňa, F. Oldewurtel, C. Sagerschnig, E. Žáčková. Building modeling is a crucial part of building predictive control. *Energy Build.* 56 (2013) 8–22
- [83] Z. Zhong, J.E. Braun, Combined heat and moisture transport modeling for residential buildings, U.S. national institute of standards and technology (2008)
- [84] D.R. Croft, D.G. Lilley, *Heat Transfer Calculations Using Finite Difference Equations*, Elsevier Science and Tech (1977)
- [85] R.B. Bird, W.E. Stewart, E.N. Lightfoot, *Transport Phenomena*, John Wiley & Sons, (2006)
- [86] US Department of Energy, *Input and Output Engineering Reference of Energy- Plus*, 2012.
- [87] J.A. Duffie, W.A. Beckman, *Solar engineering of thermal processes*. 3rd ed. Hoboken, NJ: John Wiley & Sons (2006)
- [88] F. Friembichler, S. Handler, K. Krec, H. Kuster, Energy-storage concrete thermal component activation, *bmvit* (2016)
- [89] J. Pfafferoth, D. Kalz, Thermo-active building systems, BINE Informationsdienst (2007)
- [90] G.P. Vasilyev, V.A. Lichman, N.V. Peskov, N.L. Semendyaeva, Numerical modeling of heat and moisture diffusion in porous materials, *Comput. Math. Model.* 26 (2015) 501–513
- [91] P. Bacher, H. Madsen, Identifying suitable models for the heat dynamics of buildings, *Energy Build.* 43 (2011) 1511–1522
- [92] G.P. Vasilyev, V.A. Lichman, N.V. Peskov, M.M. Brodach, Y.A. Tabunshchikov, M.V. Kolesova, Simulation of heat and moisture transfer in a multiplex structure, *Energy Build.* 86 (2015) 803–807
- [93] F. Causone, S.P. Corgnati, M. Filippi, B.W. Olesen, Experimental evaluation of heat transfer coefficients between radiant ceiling and room, *Energy Build.* 41 (2009) 622–628
- [94] A. Koca, Z. Gemici, Y. Topacoglu, G. Cetin, R.C. Acet, B.B. Kanbur, Experimental investigation of heat transfer coefficients between hydronic radiant heated wall and room, *Energy Build.* 82 (2014) 211–221
- [95] T. Cholewa, M. Rosinski, Z. Spik, M.R. Dudzinska, A. Siuta-Olcha, On the heat transfer coefficients between heated/cooled radiant floor and room, *EnergyBuild.* 66 (2013) 599–606
- [96] L. Junghans, N. Bae, Influence of the uncertainties of occupant behavior on computer-based optimization processes, *Energy Build.* 116 (2016) 478–497
- [97] C. Stetiu, Energy and peak power savings potential of radiant cooling systems in U.S. commercial buildings, *Energy Build.* 30 (1999) 127–138
- [98] D. Song, T. Kim, S. Song, S. Hwang, S.B. Leigh, Performance evaluation of a radiant floor cooling system integrated with dehumidified ventilation, *Appl. Therm. Eng.* 28 (2008) 1299–1311
- [99] W. Chung, J. Lim, Cooling operation guidelines of thermally activated building system considering the condensation risk in a hot and humid climate, *Energy Build.* 193 (2019) 226–239
- [100] Pacific Northwest National Laboratory, *The ASHRAE Standard 90.1 prototype building models* (2016)
- [101] ASHRAE Standard 90.1-2019, *Energy Standard for Buildings Except Low-Rise Residential Buildings*

- [102] U.S. Energy Information Administration (EIA), Table 5.6.A. Average Price of Electricity to Ultimate Customers by End-Use Sector, commercial (https://www.eia.gov/electricity/monthly/epm_table_grapher.php?t=epmt_5_6_a)
- [103] U.S. Environmental Protection Agency, Moisture Control Guidance for Building Design, Construction and Maintenance (2013)
- [104] Condensation in Buildings Handbook, Australian Government and States and Territories of Australia (2014)
- [105] J. Rehr, M. Horn, Temperature control for HVAC systems based on exact linearization and model predictive control. In: Int Conf Control Appl (CCA). Denver, Colorado, USA: IEEE; 2011. pp. 1119–1124
- [106] J.A. Candanedo, A.K. Athienitis, Predictive control of radiant floor heating and solar-source heat pump operation in a solar house. HVAC R Res 2011;17: 235–256
- [107] K. Thu, J. Saththasivam, B.B. Saha, K.J. Chua, S.S. Murthy, K.C. Ng, Experimental investigation of a mechanical vapor compression chiller at elevated chilled water temperatures, Appl. Therm. Eng. 123 (2017) 226–233
- [108] K.O. Amoabeng, K.H. Lee, J.M. Choi, A study on the performance characteristics of a testing facility for a water-to-water heat pump, International Journal of Refrigeration 86 (2018) 113–126
- [109] K.F. Fong, C.K. Lee, T.F. Zhao, Effective design and operation strategy of renewable cooling and heating system for building an application in a hot-humid climate, Solar Energy 143 (2017) 1–9
- [110] Y.M. Li, J.Y. Wu, Energy simulation and analysis of the heat recovery variable refrigerant flow system in winter, Energy Build. 42 (2010) 1093–1099
- [111] Taschenbuch Heizung + Klimatechnik, Recknagel, Sprengler, and Schramek, Oldenburg Publisher, edition 71 (2003)
- [112] DIN 18599-7 German building code
- [113] ASHRAE Handbook, HVAC Systems and Equipment (2016) Chapter 40
- [114] DIN 18599-6 German building code

APPENDIX A. The Whole Process of Solving the MPC Problem

The space-state for each control time-step can be defined as [45]:

$$\begin{aligned}\mathbf{x}(k+1) &= \mathbf{A}\mathbf{x}(k) + \mathbf{B}_1\mathbf{u}(k) + \mathbf{B}_2\mathbf{w}(k) \\ \mathbf{y}(k) &= \mathbf{C}\mathbf{x}(k) + \mathbf{D}_1\mathbf{u}(k) + \mathbf{D}_2\mathbf{w}(k)\end{aligned}\quad (28)$$

where \mathbf{u} denotes the controllable input (the heat flux from the TABS), and \mathbf{w} denotes known uncontrollable inputs (weather data). \mathbf{D}_1 and \mathbf{D}_2 from the above model are usually null and thus can be omitted. Thus, the future N_y states, $\hat{\mathbf{x}}(k+1) \dots \hat{\mathbf{x}}(k+N_y)$, can be calculated by [45]:

$$\begin{aligned}\hat{\mathbf{x}}(k+1) &= \mathbf{A}\mathbf{x}(k) + \mathbf{B}_1\mathbf{u}(k) + \mathbf{B}_2\mathbf{w}(k) \\ \hat{\mathbf{x}}(k+2) &= \mathbf{A}\mathbf{x}(k+1) + \mathbf{B}_1\mathbf{u}(k+1) + \mathbf{B}_2\mathbf{w}(k+1) \\ &= \mathbf{A}^2\mathbf{x}(k) + \mathbf{A}\mathbf{B}_1\mathbf{u}(k) + \mathbf{B}_1\mathbf{u}(k+1) + \mathbf{A}\mathbf{B}_2\mathbf{w}(k) + \mathbf{B}_2\mathbf{w}(k+1) \\ &\quad \vdots \\ \hat{\mathbf{x}}(k+N_y) &= \mathbf{A}^{N_y}\mathbf{x}(k) + \mathbf{A}^{N_y-1}\mathbf{B}_1\mathbf{u}(k) + \mathbf{A}^{N_y-2}\mathbf{B}_1\mathbf{u}(k+1) + \dots \\ &\quad + \mathbf{A}\mathbf{B}_1\mathbf{u}(k+N_y-1) + \mathbf{A}^{N_y-1}\mathbf{B}_2\mathbf{w}(k) \\ &\quad + \mathbf{A}^{N_y-2}\mathbf{B}_2\mathbf{w}(k+1) + \dots + \mathbf{A}\mathbf{B}_2\mathbf{w}(k+N_y-1)\end{aligned}\quad (29)$$

Using the estimation of the future states ($\hat{\mathbf{x}}$), the future N_y outputs, $\hat{\mathbf{y}}(k+1) \dots \hat{\mathbf{y}}(k+N_y)$, can be estimated as [45]:

$$\begin{aligned}
\hat{\mathbf{y}}(k+1) &= \mathbf{CA}\mathbf{x}(k) + \mathbf{CB}_1\mathbf{u}(k) + \mathbf{CB}_2\mathbf{w}(k) \\
\hat{\mathbf{y}}(k+2) &= \mathbf{CA}^2\mathbf{x}(k) + \mathbf{CAB}_1\mathbf{u}(k) + \mathbf{CB}_1\mathbf{u}(k+1) + \mathbf{CAB}_2\mathbf{w}(k) + \mathbf{CB}_2\mathbf{w}(k+1) \\
&\vdots \\
\hat{\mathbf{y}}(k+N_y) &= \mathbf{CA}^{N_y}\mathbf{x}(k) + \mathbf{CA}^{N_y-1}\mathbf{B}_1\mathbf{u}(k) + \mathbf{CA}^{N_y-2}\mathbf{B}_1\mathbf{u}(k+1) + \dots \\
&\quad + \mathbf{CAB}_1\mathbf{u}(k+N_y-1) + \mathbf{CA}^{N_y-1}\mathbf{B}_2\mathbf{w}(k) \\
&\quad + \mathbf{CA}^{N_y-2}\mathbf{B}_2\mathbf{w}(k+1) + \dots + \mathbf{CAB}_2\mathbf{w}(k+N_y-1)
\end{aligned} \tag{30}$$

Because future outputs only depend on the current states, $\mathbf{x}(k)$, current inputs and future inputs, $\mathbf{u}(k)\dots\mathbf{u}(k+N_y-1)$, $\mathbf{w}(k)\dots\mathbf{w}(k+N_y-1)$, following vectors can be derived [45]:

$$\hat{\mathbf{y}} = [\hat{\mathbf{y}}^T(k+1) \quad \hat{\mathbf{y}}^T(k+2) \quad \hat{\mathbf{y}}^T(k+3) \quad \dots \quad \hat{\mathbf{y}}^T(k+N_y)]^T \tag{31}$$

$$\mathbf{u} = [\mathbf{u}^T(k) \quad \mathbf{u}^T(k+1) \quad \mathbf{u}^T(k+2) \quad \dots \quad \mathbf{u}^T(k+N_y-1)]^T \tag{32}$$

$$\mathbf{w} = [\mathbf{w}^T(k) \quad \mathbf{w}^T(k+1) \quad \mathbf{w}^T(k+2) \quad \dots \quad \mathbf{w}^T(k+N_y-1)]^T \tag{33}$$

where $\hat{\mathbf{y}}$ is the predicted output for each time-step, \mathbf{u} is the control input for each time-step, and \mathbf{w} is the uncontrollable input for each time-step. Then, the estimation of the future N_y output can be written in matrix form as [45]:

$$\hat{\mathbf{y}} = \mathbf{F}\mathbf{x}(k) + \mathbf{\Psi}_1\mathbf{u} + \mathbf{\Psi}_2\mathbf{w} \tag{34}$$

where,

$$\mathbf{F} = \begin{bmatrix} \mathbf{CA} \\ \mathbf{CA}^2 \\ \mathbf{CA}^3 \\ \vdots \\ \mathbf{CA}^{N_y} \end{bmatrix} \quad \mathbf{\Psi}_1 = \begin{bmatrix} \mathbf{CB}_1 & 0 & 0 & \dots & 0 \\ \mathbf{CAB}_1 & \mathbf{CB}_1 & 0 & \dots & 0 \\ \mathbf{CA}^2\mathbf{B}_1 & \mathbf{CAB}_1 & \mathbf{CB}_1 & \dots & 0 \\ \vdots & \vdots & \vdots & \vdots & \vdots \\ \mathbf{CA}^{N_y-1}\mathbf{B}_1 & \mathbf{CA}^{N_y-2}\mathbf{B}_1 & \mathbf{CA}^{N_y-3}\mathbf{B}_1 & \dots & \mathbf{CAB}_1 \end{bmatrix}$$

$$\Psi_2 = \begin{bmatrix} \mathbf{CB}_2 & 0 & 0 & \cdots & 0 \\ \mathbf{CAB}_2 & \mathbf{CB}_2 & 0 & \cdots & 0 \\ \mathbf{CA}^2\mathbf{B}_2 & \mathbf{CAB}_2 & \mathbf{CB}_2 & \cdots & 0 \\ \vdots & \vdots & \vdots & \vdots & \vdots \\ \mathbf{CA}^{N_y-1}\mathbf{B}_2 & \mathbf{CA}^{N_y-2}\mathbf{B}_2 & \mathbf{CA}^{N_y-3}\mathbf{B}_2 & \cdots & \mathbf{CAB}_2 \end{bmatrix}$$

The above matrices, \mathbf{F} , Ψ_1 , and Ψ_2 are functions of constant model parameters. By defining the upper limit of the temperature in vector from [45]:

$$\mathbf{y}_{max} = [T_{max}(k+1) \ T_{max}(k+2) \ T_{max}(k+3) \ \cdots \ T_{max}(k+N_y)]^T \quad (35)$$

By replacing the future outputs by the future outputs by the relation (), optimization problem can be redefined as [45]:

minimize: $\mathbf{c}^T \mathbf{u}$

$$\text{subject to: } \begin{bmatrix} -\mathbf{I} \\ \mathbf{I} \\ \Psi_1 \end{bmatrix} \mathbf{u} \leq \begin{bmatrix} 0 \\ \mathbf{cu}_{max} \\ -\mathbf{Fx}(k) - \Psi_2 \mathbf{w} + \mathbf{y}_{max} \end{bmatrix} \quad (36)$$

The vector \mathbf{c} is a unitary vector and the matrix \mathbf{I} is the identity matrix of proper size.

$$\mathbf{c} = \begin{bmatrix} \overbrace{1 \ 1 \ \cdots \ 1}^{N_y} \end{bmatrix}^T$$

APPENDIX B. The Analyzed United States Sites Lists

Climate Zone 1
USA_FL_Fort.Lauderdale.Executive.AP.722039_TMY3
USA_FL_Homestead.AFB.722026_TMY3
USA_FL_Key.West.722010_TMY2
USA_FL_Marathon.AP.722016_TMY3
USA_FL_Miami.722020_TMY2
Climate Zone 2
USA_AL_Mobile-Downtown.AP.722235_TMY3
USA_AZ_Casa.Grande.AWOS.722748_TMY3
USA_AZ_Davis-Monthan.AFB.722745_TMY3
USA_AZ_Luke.AFB.722785_TMY3
USA_AZ_Phoenix.722780_TMY2
USA_AZ_Scottsdale.Muni.AP.722789_TMY3
USA_AZ_Tucson.722740_TMY2
USA_AZ_Yuma.MCAS.699604_TMY3
USA_CA_Imperial.County.AP.747185_TMY3
USA_FL_Apalachicola.722200_TMY
USA_FL_Crestview-Bob.Sikes.AP.722215_TMY3
USA_FL_Daytona.Beach.722056_TMY2
USA_FL_Fort.Myers-Page.Field.722106_TMY3
USA_FL_Fort.Pierce-St.Lucie.County.AP.722103_TMY3
USA_FL_Fort.Walton.Beach-Hurlburt.Field.747770_TMY3
USA_FL_Gainesville.Rgnl.AP.722146_TMY3
USA_FL_Jacksonville-Craig.Field.722068_TMY3
USA_FL_Lakeland.Linder.Rgnl.AP.722119_TMY3
USA_FL_MacDill.AFB.747880_TMY3
USA_FL_Mayport.NS.722066_TMY3
USA_FL_Melbourne.Rgnl.AP.722040_TMY3
USA_FL_Naples.Muni.AP.722038_TMY3
USA_FL_NASA.Shuttle.Landing.Facility.747946_TMY3

USA_FL_Ocala.Muni.AWOS.722055_TMY3
USA_FL_Orlando.Executive.AP.722053_TMY3
USA_FL_Panama.City-Bay.County.AP.722245_TMY3
USA_FL_Pensacola-Forest.Sherman.NAS.722225_TMY3
USA_FL_Sarasota-Bradenton.Intl.AP.722115_TMY3
USA_FL_Southwest.Florida.Intl.AP.722108_TMY3
USA_FL_St.Petersburg-Albert.Whitted.Station.722104_TMY3
USA_FL_Tallahassee.722140_TMY2 (1)
USA_FL_Tampa.722110_TMY2
USA_FL_Tyndall.AFB.747750_TMY3
USA_FL_Valparaiso-Elgin.AFB.722210_TMY3
USA_FL_Vero.Beach.Muni.AP.722045_TMY3
USA_FL_West.Palm.Beach.722030_TMY2
USA_FL_Whiting.Field.NAS.722226_TMY3
USA_GA_Alma-Bacon.County.AP.722135_TMY3
USA_GA_Atlanta-Hartsfield-Jackson.Intl.AP.722190_TMY
USA_GA_Brunswick-Golden.Isles.AP.722136_TMY3
USA_GA_Savannah.722070_TMY2
USA_GA_Valdosta-Moody.AFB.747810_TMY3
USA_LA_Alexandria-England.AFB.747540_TMY3
USA_LA_Houma-Terrebonne.AP.722406_TMY3
USA_LA_Lafayette.RgnlAP.722405_TMY3
USA_LA_Lake.Charles.722400_TMY2
USA_LA_New.Iberia.722314_TMY3
USA_LA_New.Orleans.722315_TMY2
USA_LA_New.Orleans-Alvin.Callender.Field.722316_TMY3
USA_LA_Patterson.Mem.AP.722329_TMY3
USA_MS_Biloxi-Keesler.AFB.747686_TMY3
USA_MS_Gulfport-Biloxi.Intl.AP.747685_TMY3
USA_MS_Jackson.722350_TMY2
USA_TX_Alice.Intl.AP.722517_TMY3
USA_TX_Austin.722540_TMY2
USA_TX_Beaumont-Port.Arthur.722410_TMY2
USA_TX_Brownsville.722500_TMY2
USA_TX_College.Station-Easterwood.Field.722445_TMY3
USA_TX_Corpus.Christi.722510_TMY2
USA_TX_Cotulla.AP.722526_TMY3

USA_TX_Del.Rio.722610_TMY
USA_TX_Draughton-Miller.Central.Texas.AP.722577_TMY3
USA_TX_Fort.Hood.722570_TMY3
USA_TX_Galveston.722420_TMY3
USA_TX_Georgetown.AWOS.722547_TMY3
USA_TX_Harlingen-Valley.Intl.AP.722505_TMY3
USA_TX_Hondo.Muni.AP.722533_TMY3
USA_TX_Houston-Ellington.AFB.722436_TMY3
USA_TX_Killeen-Fort.Hood.Rgnl.AP.722576_TMY3
USA_TX_Kingsville.722516_TMY
USA_TX_Laredo.Intl.AP.722520_TMY
USA_TX_Lufkin.722446_TMY2
USA_TX_McAllen-Miller.Intl.AP.722506_TMY3
USA_TX_McGregor.AWOS.722563_TMY3
USA_TX_Mineral.Wells.Muni.AP.722597_TMY3
USA_TX_Palacios.Muni.AP.722555_TMY3
USA_TX_Port.Arthur-Jefferson.Co.AP.722410_TMY
USA_TX_Rockport-Aransas.Co.AP.722524_TMY3
USA_TX_San.Antonio.722536_TMY2
USA_TX_Victoria.722550_TMY2
USA_TX_Waco.722560_TMY2
Climate Zone 3
USA_AL_Anniston.Metro.AP.722287_TMY3
USA_AL_Auburn-Opelika.AP.722284_TMY3
USA_AL_Birmingham.722280_TMY2
USA_AL_Dothan.Muni.AP.722268_TMY3
USA_AL_Fort.Rucker-Cairns.Field.722269_TMY3
USA_AL_Gadsen.Muni.AWOS.722285_TMY3
USA_AL_Huntsville.723230_TMY2
USA_AL_Maxwell.AFB.722265_TMY3
USA_AL_Montgomery-Dannelly.Field.722260_TMY
USA_AL_Muscle.Shoals.Rgnl.AP.723235_TMY3
USA_AL_Troy.Air.Field.722267_TMY3
USA_AL_Tuscaloosa.Muni.AP.722286_TMY3
USA_AR_Batesville.AWOS.723448_TMY3
USA_AR_El.Dorado-Goodwin.Field.723419_TMY3
USA_AR_Fort.Smith.723440_TMY2

USA_AR_Hot.Springs.Mem.AP.723415_TMY3
USA_AR_Jonesboro.Muni.AP.723407_TMY3
USA_AR_Little.Rock-Adams.Field.723403_TMY
USA_AR_Pine.Bluff.AP.723417_TMY3
USA_AR_Stuttgart.AWOS.723416_TMY3
USA_AR_Texarkana-Webb.Field.723418_TMY3
USA_AR_Walnut.Ridge.AWOS.723406_TMY3
USA_AZ_Douglas-Bisbee.Douglas.Intl.AP.722735_TMY3
USA_AZ_Kingman.AWOS.723700_TMY3
USA_AZ_Safford.AWOS.722747_TMY3
USA_CA_Barstow-Daggett.723815_TMY2
USA_CA_Beale.AFB.724837_TMY3
USA_CA_Blue.Canyon.AP.725845_TMY3
USA_CA_Blythe-Riverside.County.AP.747188_TMY3
USA_CA_Burbank-Glendale-Pasadena.Bob.Hope.AP.722880_TMY3
USA_CA_Camarillo.AWOS.723926_TMY3
USA_CA_Camp.Pendleton.MCAS.722926_TMY3
USA_CA_Carlsbad.722927_TMY3
USA_CA_China.Lake.NAF.746120_TMY
USA_CA_Chino.AP.722899_TMY3
USA_CA_Chula.Vista-Brown.Field.Muni.AP.722904_TMY3
USA_CA_Concord-Buchanan.Field.724936_TMY3
USA_CA_Edwards.AFB.723810_TMY3
USA_CA_El.Toro.MCAS.690140_TMY
USA_CA_Fairfield-Travis.AFB.745160_TMY3
USA_CA_Fresno.723890_TMY2
USA_CA_Fullerton.Muni.AP.722976_TMY3
USA_CA_Hawthorne-Jack.Northrop.Field.722956_TMY3
USA_CA_Hayward.Air.Terminal.724935_TMY3
USA_CA_Lancaster-Gen.Wm.Fox.Field.723816_TMY3
USA_CA_Lemoore.NAS.747020_TMY3
USA_CA_Livermore.Muni.AP.724927_TMY3
USA_CA_Lompoc.AWOS.722895_TMY3
USA_CA_Long.Beach-Daugherty.Field.722970_TMY
USA_CA_Los.Angeles.722950_TMY2 (1)
USA_CA_March.AFB.722860_TMY3
USA_CA_Merced-Macready.Field.724815_TMY3

USA_CA_Modesto.Muni.AP.724926_TMY3
USA_CA_Monterey.NAF.724915_TMY3
USA_CA_Mountain.View-Moffett.Field.NAS.745090_TMY
USA_CA_Napa.County.AP.724955_TMY3
USA_CA_Needles.AP.723805_TMY3
USA_CA_Oakland.Intl.AP.724930_TMY
USA_CA_Oxnard.AP.723927_TMY3
USA_CA_Palm.Springs-Thermal.AP.747187_TMY3
USA_CA_Palmdale.AP.723820_TMY3
USA_CA_Paso.Robles.Muni.AP.723965_TMY3
USA_CA_Point.Mugu.NAS.723910_TMY
USA_CA_Porterville.AWOS.723895_TMY3
USA_CA_Red.Bluff.Muni.AP.725910_TMY
USA_CA_Redding.Muni.AP.725920_TMY3
USA_CA_Riverside.Muni.AP.722869_TMY3
USA_CA_Sacramento.724835_TMY2
USA_CA_Salinas.Muni.AP.724917_TMY3
USA_CA_San.Diego.722900_TMY2
USA_CA_San.Francisco.724940_TMY2
USA_CA_San.Jose.Intl.AP.724945_TMY3
USA_CA_San.Luis.Obispo.AP.722897_TMY3
USA_CA_Sandberg.723830_TMY3
USA_CA_Santa.Ana-John.Wayne.AP.722977_TMY3
USA_CA_Santa.Barbara.Muni.AP.723925_TMY3
USA_CA_Santa.Maria.723940_TMY2
USA_CA_Santa.Monica.Muni.AP.722885_TMY3
USA_CA_Santa.Rosa.AWOS.724957_TMY3
USA_CA_Twenty-nine.Palms.690150_TMY3
USA_CA_Ukiah.Muni.AP.725905_TMY3
USA_CA_Van.Nuys.AP.722886_TMY3
USA_CA_Visalia.Muni.AWOS.723896_TMY3
USA_CA_Yuba.County.AP.724838_TMY3
USA_GA_Albany-Dougherty.County.AP.722160_TMY3
USA_GA_Athens.723110_TMY2
USA_GA_Augusta-Bush-Field.722180_TMY
USA_GA_Columbus.722255_TMY2
USA_GA_Dekalb.Peachtree.AP.722196_TMY3

USA_GA_Fort.Benning-Lawson.Field.722250_TMY3
USA_GA_Fulton.County.AP.722195_TMY3
USA_GA_Macon-Middle.Georgia.Rgnl.AP.722170_TMY
USA_GA_Marietta-Dobbins.AFB.722270_TMY3
USA_GA_Warner.Robins.AFB.722175_TMY3
USA_LA_Fort.Polk.722390_TMY3
USA_LA_Monroe.Rgnl.AP.722486_TMY3
USA_LA_Shreveport.722480_TMY2
USA_Lenoir.MCAS.723096_TMY3
USA_MS_Columbus.AFB.723306_TMY3
USA_MS_Golden.Triangle.Rgnl.AWOS.723307_TMY3
USA_MS_Greenville.Muni.AP.722356_TMY3
USA_MS_Hattiesburg-Laurel.AP.722348_TMY3
USA_MS_McComb-Pike.Co.AP.722358_TMY3
USA_MS_Meridian.722340_TMY2
USA_MS_Meridian-Key.Field.722340_TMY
USA_MS_Natchez-Hardy.Anders.Field.722357_TMY3
USA_MS_Tupelo.Muni-C.D.Lemons.AP.723320_TMY3
USA_NC_Cape.Hatteras.723040_TMY
USA_NC_Charlotte.723140_TMY2
USA_NC_Cherry.Point.MCAS.723090_TMY
USA_NC_Elizabeth.City.CGAS.746943_TMY3
USA_NC_Fayetteville.Muni.AP.723035_TMY3
USA_NC_Fort.Bragg-Simmons.AAF.746930_TMY3
USA_NC_Jacksonville.AWOS.723069_TMY3
USA_NC_Kinston.Stallings.AFB.723067_TMY3
USA_NC_Manteo-Dare.County.Rgnl.AP.723046_TMY3
USA_NC_New.Bern-Craven.County.Rgnl.AP.723095_TMY3
USA_NC_Pitt.Greenville.AP.723065_TMY3
USA_NC_Rocky.Mount-Wilson.AP.723068_TMY3
USA_NC_Southern.Pines-Moore.County.AP.723143_TMY3
USA_NC_Wilmington.723013_TMY2
USA_NM_Carlsbad.Cavern.City.Air.Terminal.722687_TMY3
USA_NM_Deming.Muni.AP.722725_TMY3
USA_NM_Holloman.AFB.747320_TMY3
USA_NM_Las.Cruces.Intl.AP.722695_TMY3
USA_NM_Roswell.Industrial.Air.Park.722680_TMY

USA_NV_Las.Vegas.723860_TMY2
USA_NV_Nellis.AFB.723865_TMY3
USA_OK_Altus.AFB.723520_TMY3
USA_OK_Bartlesville-Phillips.Field.723565_TMY3
USA_OK_Clinton.Sherman.AP.723526_TMY3
USA_OK_Fort.Sill-Henry.Post.AAF.723550_TMY3
USA_OK_Gage.AP.723527_TMY3
USA_OK_Hobart.Muni.AP.723525_TMY3
USA_OK_Lawton.Muni.AP.723575_TMY3
USA_OK_McAlester.Rgnl.AP.723566_TMY3
USA_OK_Oklahoma.City.723530_TMY2
USA_OK_Ponca.City.Muni.AP.723546_TMY3
USA_OK_Stillwater.Rgnl.AP.723545_TMY3
USA_OK_Tulsa.723560_TMY2
USA_OK_Vance.AFB.723535_TMY3
USA_SC_Anderson.County.AP.723125_TMY3
USA_SC_Beaufort.MCAS.722085_TMY3
USA_SC_Charleston.722080_TMY2 (1)
USA_SC_Columbia.723100_TMY2
USA_SC_Florence.Rgnl.AP.723106_TMY3
USA_SC_Greenville-Downtown.AP.723119_TMY3
USA_SC_Myrtle.Beach.AFB.747910_TMY3
USA_SC_Shaw.AFB.747900_TMY3
USA_TN_Dyersburg.Muni.AP.723347_TMY3
USA_TN_Jackson-McKellar.Sipes.Rgnl.AP.723346_TMY3
USA_TN_Memphis.723340_TMY2
USA_TX_Abilene.722660_TMY2
USA_TX_Childress.Muni.AP.723604_TMY3
USA_TX_Cox.Field.722587_TMY3
USA_TX_Dallas-Love.Field.722583_TMY3
USA_TX_El.Paso.722700_TMY2
USA_TX_Fort.Worth.722596_TMY2
USA_TX_Greenville.Muni.AP.722588_TMY3
USA_TX_Longview-Gregg.County.AP.722470_TMY3
USA_TX_Lubbock.722670_TMY2
USA_TX_Marfa.AP.722640_TMY3
USA_TX_Midland-Odessa.722650_TMY2

USA_TX_Nacogdoches.AWOS.722499_TMY3
USA_TX_Randolph.AFB.722536_TMY3
USA_TX_San.Angelo.722630_TMY2
USA_TX_Wichita.Falls.723510_TMY2
USA_TX_Wink-Winkler.County.AP.722656_TMY3
USA_UT_Saint.George.AWOS.724754_TMY3
Climate Zone 4
USA_AR_Fayetteville-Drake.Field.723445_TMY3
USA_AR_Flippin.AWOS.723447_TMY3
USA_AR_Harrison.AP.723446_TMY3
USA_AR_Rogers.AWOS.723449_TMY3
USA_AR_Siloam.Spring.AWOS.723443_TMY3
USA_AR_Springdale.Muni.AP.723434_TMY3
USA_AZ_Prescott-Love.Field.723723_TMY
USA_CA_Arcata.725945_TMY2
USA_CA_Bishop.AP.724800_TMY3
USA_CA_Crescent.City-Jack.McNamara.Field.725946_TMY3
USA_CA_South.Lake.Tahoe-Lake.Tahoe.AP.725847_TMY3
USA_CO_La.Junta.Muni.AP.724635_TMY3
USA_CO_Trinidad-Las.Animas.County.AP.724645_TMY3
USA_DE_Dover.AFB.724088_TMY3
USA_DE_Wilmington.724089_TMY2
USA_DE_Wilmington-New.Castle.County.AP.724089_TMY
USA_DE_Wilmington-New.Castle.County.AP.724089_TMY3
USA_GA_Rome-Richard.B.Russell.AP.723200_TMY3
USA_IL_Belleville-Scott.AFB.724338_TMY3
USA_IL_Carbondale-Southern.Illinois.AP.724336_TMY3
USA_IL_Marion-Williamson.County.Rgnl.AP.724339_TMY3
USA_IL_Mount.Vernon.AWOS.724335_TMY3
USA_IN_Evansville.724320_TMY2
USA_IN_Huntingburg.Muni.AP.724365_TMY3
USA_IN_Monroe.County.AP.724375_TMY3
USA_KS_Chanute-Martin.Johnson.AP.724507_TMY3
USA_KS_Dodge.City.Rgnl.AP.724510_TMY3
USA_KS_Emporia.Muni.AP.724556_TMY3
USA_KS_Fort.Riley-Marshall.AAF.724550_TMY3
USA_KS_Garden.City.Muni.AP.724515_TMY3

USA_KS_Great.Bend.AWOS.724517_TMY3
USA_KS_Hutchinson.Muni.AP.724506_TMY3
USA_KS_Liberal.Muni.AP.724516_TMY3
USA_KS_Manhattan.Rgnl.AP.724555_TMY3
USA_KS_Newton.AWOS.724509_TMY3
USA_KS_Olathe-Johnson.County.Executive.AP.724468_TMY3
USA_KS_Salina.Muni.AP.724586_TMY3
USA_KS_Topeka.724560_TMY2
USA_KY_Bowling.Green-Warren.County.AP.746716_TMY3
USA_KY_Cincinnati-Northern.Kentucky.AP.724210_TMY
USA_KY_Covington-Cincinnati.AP.724210_TMY2
USA_KY_Fort.Campbell.AAF.746710_TMY3
USA_KY_Fort.Knox-Godman.AAF.724240_TMY3
USA_KY_Henderson.City.County.AP.724238_TMY3
USA_KY_Jackson-Julian.Carroll.AP.724236_TMY3
USA_KY_Lexington.724220_TMY2
USA_KY_Lexington-Bluegrass.AP.724220_TMY
USA_KY_London-Corbin-Magee.Field.724243_TMY3
USA_KY_Louisville-Bowman.Field.724235_TMY3
USA_KY_Paducah-Barkley.Rgnl.AP.724350_TMY3
USA_KY_Somerset-Pulaski.County.AWOS.724354_TMY3
USA_MD_Andrews.AFB.745940_TMY3
USA_MD_Baltimore.724060_TMY2
USA_MD_Hagerstown-Washington.County.Rgnl.AP.724066_TMY3
USA_MD_Patuxent.River.NAS.724040_TMY
USA_MD_Salisbury-Wicomico.County.Rgnl.AP.724045_TMY3
USA_MO_Cape.Girardeau.Muni.AP.723489_TMY3
USA_MO_Columbia.724450_TMY2
USA_MO_Farmington.Rgnl.AP.724454_TMY3
USA_MO_Fort.Leonard.Wood-Forney.AAF.724457_TMY3
USA_MO_Jefferson.City.Mem.AP.724458_TMY3
USA_MO_Joplin.Muni.AP.723495_TMY3
USA_MO_Kaiser-Lee.Fine.Mem.AWOS.724459_TMY3
USA_MO_Kansas.City.724460_TMY2
USA_MO_Poplar.Bluff.AWOS.723300_TMY3
USA_MO_Rolla.National.AP.724456_TMY3
USA_MO_Springfield.724400_TMY2

USA_MO_St.Louis.724340_TMY2
USA_MO_Whiteman.AFB.724467_TMY3
USA_NC_Ashville.723150_TMY2
USA_NC_Greensboro.723170_TMY2
USA_NC_Greensboro-Piedmont.Triad.Intl.AP.723170_TMY
USA_NC_Hickory.Rgnl.AP.723145_TMY3
USA_NC_Raleigh-Durham.723060_TMY2
USA_NC_Winston.Salem-Smith.Reynolds.AP.723193_TMY3
USA_NJ_Atlantic.City.724070_TMY2
USA_NJ_Belmar-Monmouth.County.AP.724084_TMY3
USA_NJ_Caldwell-Essex.County.AP.724094_TMY3
USA_NJ_Cape.May.County.AP.745966_TMY3
USA_NJ_McGuire.AFB.724096_TMY
USA_NJ_Millville.Muni.AP.724075_TMY3
USA_NJ_Newark.725020_TMY2
USA_NM_Albuquerque.723650_TMY2
USA_NM_Clayton.Muni.AP.723600_TMY3
USA_NM_Clayton.Muni.AP.723600_TMY3
USA_NM_Ruidoso-Sierra.Blanca.Rgnl.AP.722683_TMY3
USA_NM_Truth.or.Consequences.Muni.AP.722710_TMY
USA_NM_Tucumcari.723676_TMY2
USA_NY_Islip-Long.Island.MacArthur.AP.725035_TMY3
USA_NY_New.York.City-Central.Park.94728_TMY
USA_NY_Republic.AP.744864_TMY3
USA_NY_Westhampton-Suffolk.County.AP.744865_TMY3
USA_NY_White.Plains-Westchester.County.AP.725037_TMY3
USA_OH_Cincinnati.Muni.AP-Lunken.Field.724297_TMY3
USA_PA_Philadelphia.724086_TMY2
USA_PA_Willow.Grove.NAS.724086_TMY3
USA_TN_Bristol.723183_TMY2
USA_TN_Bristol-TriCities.Rgnl.AP.723183_TMY3
USA_TN_Chattanooga.723240_TMY2
USA_TN_Crossville.Mem.AP.723265_TMY3
USA_TN_Knoxville-McGhee.Tyson.AP.723260_TMY
USA_TN_Nashville.723270_TMY2
USA_TX_Amarillo.723630_TMY2
USA_TX_Dalhart.Muni.AP.722636_TMY3

USA_TX_Sherman-Perrin.AFB.722541_TMY
USA_TX_Tyler-Pounds.Field.722448_TMY3
USA_VA_Abingdon-Virgina.Highlands.AP.724058_TMY3
USA_VA_Blacksburg-Virginia.Tech.AP.724113_TMY3
USA_VA_Charlottesville-Albemarle.County.AP.724016_TMY3
USA_VA_Danville.Rgnl.AP.724106_TMY3
USA_VA_Farmville.Muni.AP.724017_TMY3
USA_VA_Franklin.Muni.AP.723083_TMY3
USA_VA_Fredericksburg-Shannon.AP.724033_TMY3
USA_VA_Hillsville-Twin.County.AP.724107_TMY3
USA_VA_Hot.Springs-Ingalls.Field.724115_TMY3
USA_VA_Langley.AFB.745980_TMY3
USA_VA_Leesburg.Muni.AP-Godfrey.Field.724055_TMY3
USA_VA_Lynchburg.724100_TMY2
USA_VA_Manassas.Muni.AWOS.724036_TMY3
USA_VA_Marion-Wytheville-Mountain.Empire.AP.724056_TMY3
USA_VA_Martinsville-Blue.Ridge.AP.745985_TMY3
USA_VA_Melfa-Accomack.County.AP.724026_TMY3
USA_VA_Newport.News.723086_TMY3
USA_VA_Norfolk.723080_TMY2
USA_VA_Oceana.NAS.723075_TMY3
USA_VA_Petersburg.Muni.AP.724014_TMY3
USA_VA_Pulaski-New.River.Valley.AP.724116_TMY3
USA_VA_Quantico.MCAS.724035_TMY3
USA_VA_Richmond.724010_TMY2
USA_VA_Roanoke.724110_TMY2
USA_VA_Staunton-Shenandoah.Valley.Rgnl.AP.724105_TMY3
USA_VA_Sterling-Washington.Dulles.724030_TMY2
USA_VA_Winchester.Rgnl.AP.724053_TMY3
USA_VA_Wise-Lonesome.Pine.AP.724117_TMY3
USA_WV_Bluefield-Mercer.County.AP.724125_TMY3
USA_WV_Charleston.724140_TMY2
USA_WV_Huntington.724250_TMY2
USA_WV_Martinsburg-Eastern.WV.Rgnl.AP.724177_TMY3
USA_WV_Parkersburg-Wood.County-Gill.Robb.Wilson.AP.724273_TMY3
Climate Zone 5
USA_AZ_Flagstaff-Pulliam.AP.723755_TMY3

USA_AZ_Grand.Canyon.National.Park.AP.723783_TMY3
USA_AZ_Page.Muni.AWOS.723710_TMY3
USA_AZ_Show.Low.Muni.AP.723747_TMY3
USA_AZ_Winslow.Muni.AP.723740_TMY
USA_CA_Alturas.725958_TMY3
USA_CA_Montague-Siskiyou.County.AP.725955_TMY3
USA_CA_Mount.Shasta.725957_TMY
USA_CO_Akron-Washington.County.AP.724698_TMY3
USA_CO_Aurora-Buckley.Field.ANGB.724695_TMY3
USA_CO_Boulder.724699_TMY2
USA_CO_Colorado.Springs.724660_TMY2
USA_CO_Cortez-Montezuma.County.AP.724767_TMY3
USA_CO_Denver-Stapleton.724690_TMY
USA_CO_Durango-La.Plata.County.AP.724625_TMY3
USA_CO_Fort.Collins.AWOS.724769_TMY3
USA_CO_Golden-NREL.724666_TMY3
USA_CO_Grand.Junction-Walker.Field.724760_TMY
USA_CO_Greeley-Weld.County.AWOS.724768_TMY3
USA_CO_Lamar.Muni.AP.724636_TMY3
USA_CO_Limon.Muni.AP.724665_TMY3
USA_CO_Montrose.County.AP.724765_TMY3
USA_CO_Pueblo.724640_TMY2
USA_CO_Rifle-Garfield.County.Rgnl.AP.725717_TMY3
USA_CT_Bridgeport-Sikorsky.Mem.AP.725040_TMY3
USA_CT_Danbury.Muni.AP.725086_TMY3
USA_CT_Groton-New.London.AP.725046_TMY3
USA_CT_Hartford.725087_TMY2
USA_CT_Hartford-Bradley.Intl.AP.725080_TMY
USA_CT_New.Haven-Tweed.AP.725045_TMY3
USA_CT_Oxford.AWOS.725029_TMY3
USA_IA_Atlantic.Muni.AP.725453_TMY3
USA_IA_Boone.Muni.AP.725486_TMY3
USA_IA_Burlington.Muni.AP.725455_TMY
USA_IA_Carroll.Muni.AP.725468_TMY3
USA_IA_Cedar.Rapids.Muni.AP.725450_TMY3
USA_IA_Chariton.Muni.AP.725469_TMY3
USA_IA_Clinton.Muni.AWOS.725473_TMY3

USA_IA_Council.Bluffs.Muni.AP.725497_TMY3
USA_IA_Creston.Muni.AP.725474_TMY3
USA_IA_Denison.Muni.AP.725477_TMY3
USA_IA_Des.Moines.725460_TMY2
USA_IA_Dubuque.Rgnl.AP.725470_TMY3
USA_IA_Fairfield.Muni.AP.726498_TMY3
USA_IA_Fort.Madison.Muni.AP.725483_TMY3
USA_IA_Keokuk.Muni.AP.725456_TMY3
USA_IA_Knoxville.Muni.AP.725493_TMY3
USA_IA_Monticello.Muni.AP.725475_TMY3
USA_IA_Muscatine.Muni.AP.725487_TMY3
USA_IA_Newton.Muni.AP.725464_TMY3
USA_IA_Ottumwa.Industrial.AP.725465_TMY3
USA_IA_Red.Oak.Muni.AP.725494_TMY3
USA_IA_Sheldon.Muni.AP.725495_TMY3
USA_IA_Shenandoah.Muni.AP.725467_TMY3
USA_IA_Sioux.City.725570_TMY2
USA_ID_Burley.Muni.AP.725867_TMY3
USA_ID_Coeur.dAlene.AWOS.727834_TMY3
USA_ID_Lewiston-Nez.Perce.County.AP.727830_TMY
USA_ID_Mountain.Home.AFB.726815_TMY3
USA_IL_Aurora.Muni.AP.744655_TMY3
USA_IL_Bloomington.Normal-Central.Illinois.Rgnl.AP.724397_TMY3
USA_IL_Chicago-Midway.AP.725340_TMY
USA_IL_Decatur.AP.725316_TMY3
USA_IL_Du.Page.AP.725305_TMY3
USA_IL_Moline-Quad.City.Intl.AP.725440_TMY
USA_IL_Peoria-Greater.Peoria.AP.725320_TMY3
USA_IL_Quincy.Muni.AP.724396_TMY3
USA_IL_Rockford-Greater.Rockford.AP.725430_TMY3
USA_IL_Springfield-Capital.AP.724390_TMY
USA_IL_Sterling-Rock.Falls-Whiteside.County.AP.725326_TMY3
USA_IL_University.of.Illinois-Willard.AP.725315_TMY3
USA_IL_Waukegan.Rgnl.AP.725347_TMY3
USA_IN_Delaware.County-Johnson.Field.725336_TMY3
USA_IN_Fort.Wayne.725330_TMY2
USA_IN_Grissom.AFB.725335_TMY3

USA_IN_Indianapolis.724380_TMY2
USA_IN_Lafayette-Purdue.University.AP.724386_TMY3
USA_IN_South.Bend.725350_TMY2
USA_IN_South.Bend-Michiana.Rgnl.AP.725350_TMY
USA_KS_Concordia-Blosser.Muni.AP.724580_TMY3
USA_KS_Goodland-Renner.Field.724650_TMY
USA_KS_Hill.City.Muni.AP.724655_TMY3
USA_KS_Russell.Muni.AP.724585_TMY3
USA_KS_Wichita.724500_TMY2
USA_KS_Wichita-Col.Jabara.Field.724504_TMY3
USA_MA_Barnstable-Boardman.Poland.AP.725067_TMY3
USA_MA_Beverly.Muni.AP.725088_TMY3
USA_MA_Boston-Logan.725090_TMY2
USA_MA_Chicopee.Falls-Westover.AFB.744910_TMY3
USA_MA_Lawrence.Muni.AP.744904_TMY3
USA_MA_Marthas.Vineyard.AP.725066_TMY3
USA_MA_Nantucket.Mem.AP.725063_TMY3
USA_MA_New.Bedford.Rgnl.AP.725065_TMY3
USA_MA_North.Adams.AP.725075_TMY3
USA_MA_Norwood.Mem.AP.725098_TMY3
USA_MA_Otis.ANGB.725060_TMY3
USA_MA_Plymouth.Muni.AP.725064_TMY3
USA_MA_Provincetown.AWOS.725073_TMY3
USA_MA_Westfield-Barnes.Muni.AP.744915_TMY3
USA_MI_Ann.Arbor.Muni.AP.725374_TMY3
USA_MI_Battle.Creek-Kellogg.AP.725396_TMY3
USA_MI_Benton.Harbor-Ross.Field-Twin.Cities.AP.726355_TMY3
USA_MI_Detroit-City.AP.725375_TMY
USA_MI_Flint.726370_TMY2
USA_MI_Grand.Rapids-Kent.County.Intl.AP.726350_TMY
USA_MI_Howell-Livingston.County.AP.725378_TMY3
USA_MI_Jackson-Reynolds.Field.725395_TMY3
USA_MI_Kalamazoo-Battle.Creek.Intl.AP.726357_TMY3
USA_MI_Lansing-Capital.City.AP.725390_TMY3
USA_MI_Mount.Clemens-Selfridge.ANGB.725377_TMY3
USA_MI_Muskegon.County.AP.726360_TMY3
USA_MI_Oakland.County.Intl.AP.726375_TMY3

USA_MI_Saginaw-Tri.City.Intl.AP.726379_TMY3
USA_MI_St.Clair.County.Intl.AP.725384_TMY3
USA_MO_Kirksville.Muni.AP.724455_TMY3
USA_MO_St.Joseph-Rosecrans.Mem.AP.724490_TMY3
USA_NE_Ainsworth.Muni.AP.725556_TMY3
USA_NE_Alliance.Muni.AP.725635_TMY3
USA_NE_Beatrice.Muni.AP.725515_TMY3
USA_NE_Bellevue-Offutt.AFB.725540_TMY3
USA_NE_Broken.Bow.Muni.AP.725555_TMY3
USA_NE_Chadron.Muni.AP.725636_TMY3
USA_NE_Columbus.Muni.AP.725565_TMY3
USA_NE_Falls.City-Brenner.Field.725533_TMY3
USA_NE_Fremont.Muni.AP.725564_TMY3
USA_NE_Grand.Island.725520_TMY2
USA_NE_Hastings.Muni.AP.725525_TMY3
USA_NE_Holdrege-Brewster.Field.725628_TMY3
USA_NE_Imperial.Muni.AP.725626_TMY3
USA_NE_Kearney.Muni.AWOS.725526_TMY3
USA_NE_Lincoln.Muni.AP.725510_TMY3
USA_NE_McCook.Muni.AP.725625_TMY3
USA_NE_Norfolk.725560_TMY2
USA_NE_North.Platte.725620_TMY2
USA_NE_Omaha.725500_TMY2
USA_NE_ONeill-Baker.Field.725566_TMY3
USA_NE_Ord-Sharp.Field.725524_TMY3
USA_NE_Scottsbluff.725660_TMY2
USA_NE_Sidney.Muni.AP.725610_TMY3
USA_NE_Tekamah.AWOS.725527_TMY3
USA_NE_Valentine-Miller.Field.725670_TMY3
USA_NH_Keene-Dillant.Hopkins.AP.726165_TMY3
USA_NH_Manchester.Muni.AP.743945_TMY3
USA_NH_Pease.Intl.Tradeport.726055_TMY3
USA_NJ_Teterboro.AP.725025_TMY3
USA_NJ_Trenton-Mercer.County.AP.724095_TMY3
USA_NM_Farmington-Four.Corners.Rgnl.AP.723658_TMY3
USA_NM_Gallup-Sen.Clarke.Field.723627_TMY3
USA_NM_Las.Vegas-Muni.AP.723677_TMY3

USA_NM_Los.Alamos.723654_TMY2
USA_NM_Santa.Fe.County.Muni.AP.723656_TMY3
USA_NM_Taos.Muni.AP.723663_TMY3
USA_NV_Ely.724860_TMY2
USA_NV_Fallon.NAS.724885_TMY3
USA_NV_Lovelock-Derby.Field.725805_TMY
USA_NV_Mercury-Desert.Rock.AP.723870_TMY3
USA_NV_Reno.724880_TMY2
USA_NV_Tonopah.724855_TMY2
USA_NV_Winnemucca.725830_TMY2
USA_NV_Yucca.Flats.723850_TMY
USA_NY_Albany.725180_TMY2
USA_NY_Buffalo.725280_TMY2
USA_NY_Elmira.Rgnl.AP.725156_TMY3
USA_NY_Jamestown.AWOS.725235_TMY3
USA_NY_Newburgh-Stewart.Intl.AP.725038_TMY3
USA_NY_Niagara.Falls.Intl.AP.725287_TMY3
USA_NY_Poughkeepsie-Dutchess.County.AP.725036_TMY3
USA_NY_Rochester.725290_TMY2
USA_NY_Syracuse.725190_TMY2
USA_OH_Akron.725210_TMY2
USA_OH_Cleveland-Burke.Lakefront.AP.725245_TMY3
USA_OH_Columbus-Port.Columbus.Intl.AP.724280_TMY
USA_OH_Dayton-Wright.Patterson.AFB.745700_TMY
USA_OH_Findlay.AP.725366_TMY3
USA_OH_Mansfield.725246_TMY2
USA_OH_Ohio.State.University.AP.724288_TMY3
USA_OH_Toledo.725360_TMY2
USA_OH_Youngstown.725250_TMY2
USA_OH_Zanesville.Muni.AP.724286_TMY3
USA_OR_Astoria.727910_TMY2
USA_OR_Aurora.State.AP.726959_TMY3
USA_OR_Baker.Muni.AP.726886_TMY3
USA_OR_Burns.726830_TMY2
USA_OR_Corvallis.Muni.AP.726945_TMY3
USA_OR_Eugene.726930_TMY2
USA_OR_Klamath.Falls.Intl.AP.725895_TMY3

USA_OR_La.Grande.Muni.AP.726884_TMY3
USA_OR_Lakeview.AWOS.725976_TMY3
USA_OR_Medford.725970_TMY2
USA_OR_North.Bend.726917_TMY2
USA_OR_Pendleton.726880_TMY2
USA_OR_Portland.726980_TMY2
USA_OR_Redmond.726835_TMY2
USA_OR_Roseburg.Rgnl.AP.726904_TMY3
USA_OR_Salem.726940_TMY2
USA_OR_Sexton.Summit.725975_TMY3
USA_PA_Allentown-Lehigh.Valley.Intl.AP.725170_TMY
USA_PA_Altoona-Blair.County.AP.725126_TMY3
USA_PA_Bradford.725266_TMY2
USA_PA_Butler.County.AWOS.725124_TMY3
USA_PA_DuBois-Jefferson.County.AP.725125_TMY3
USA_PA_Erie.725260_TMY2
USA_PA_Franklin-Chess.Lemberton.AP.725267_TMY3
USA_PA_Harrisburg.725115_TMY2
USA_PA_Johnstown-Cambria.County.AP.725127_TMY3
USA_PA_Lancaster.AP.725116_TMY3
USA_PA_Pittsburgh.725200_TMY2
USA_PA_Reading.Mem.AP-Spaatz.Field.725103_TMY3
USA_PA_State.College-Penn.State.University.725128_TMY3
USA_PA_Washington.AWOS.725117_TMY3
USA_PA_Wilkes.Barre-Scranton.725130_TMY2
USA_PA_Williamsport.725140_TMY2
USA_RI_Block.Island.State.AP.725058_TMY3
USA_RI_Pawtucket.AWOS.725054_TMY3
USA_RI_Providence.725070_TMY2
USA_RI_Providence-T.F.Green.State.AP.725070_TMY
USA_SD_Yankton-Chan.Gurney.Muni.AP.726525_TMY3
USA_UT_Blanding.Muni.AP.724723_TMY3
USA_UT_Bryce.Canyon.AP.724756_TMY
USA_UT_Cedar.City.724755_TMY2
USA_UT_Delta.Muni.AP.724795_TMY3
USA_UT_Moab-Canyonlands.Field.724776_TMY3
USA_UT_Ogden-Hill.AFB.725755_TMY3

USA_UT_Provo.Muni.AWOS.725724_TMY3
USA_UT_Salt.Lake.City.725720_TMY2
USA_UT_Wendover.USAF.Auxiliary.Field.725810_TMY3
USA_WA_Bremerton.National.AP.727928_TMY3
USA_WA_Ephrata.Muni.AP.727826_TMY3
USA_WA_Fairchild.AFB.727855_TMY3
USA_WA_Fort.Lewis-Gray.AAF.742070_TMY3
USA_WA_Hanford.727840_TMY3
USA_WA_Hoquiam.AP.727923_TMY3
USA_WA_Kelso.AP.727924_TMY3
USA_WA_Olympia.727920_TMY2
USA_WA_Pasco-Tri.Cities.AP.727845_TMY3
USA_WA_Port.Angeles-William.R.Fairchild.Intl.AP.727885_TMY3
USA_WA_Pullman-Moscow.Rgnl.AP.727857_TMY3
USA_WA_Quillayute.727970_TMY2
USA_WA_Renton.Muni.AP.727934_TMY3
USA_WA_Seattle-Tacoma.727930_TMY2
USA_WA_Snohomish.County.AP.727937_TMY3
USA_WA_Spokane-Felts.Field.727856_TMY3
USA_WA_Stampede.Pass.727815_TMY3
USA_WA_Tacoma.Narrows.AP.727938_TMY3
USA_WA_The.Dalles.Muni.AP.726988_TMY3
USA_WA_Toledo-Winlock-Ed.Carlson.Mem.AP.727926_TMY3
USA_WA_Walla.Walla.City-County.AP.727846_TMY3
USA_WA_Whidbey.Island.NAS.690230_TMY
USA_WA_Yakima.727810_TMY2
USA_WV_Beckley-Raleigh.County.Mem.AP.724120_TMY3
USA_WV_Clarksburg-Harrison.Marion.Rgnl.AP.724175_TMY3
USA_WV_Elkins.724170_TMY2
USA_WV_Lewisburg-Greenbrier.Valley.AP.724127_TMY3
USA_WV_Morgantown.Muni-Hart.Field.724176_TMY3
USA_WV_Wheeling-Ohio.County.AP.724275_TMY3
Climate Zone 6
USA_CO_Alamosa.724620_TMY2
USA_CO_Craig.Moffat.AP.725700_TMY3
USA_CO_Eagle.724675_TMY2
USA_IA_Algona.Muni.AP.725457_TMY3

USA_IA_Charles.City.Muni.AP.725463_TMY3
USA_IA_Clarinda.Muni.AP.725479_TMY3
USA_IA_Decorah.Muni.AP.725476_TMY3
USA_IA_Estherville.Muni.AP.726499_TMY3
USA_IA_Fort.Dodge.AWOS.725490_TMY3
USA_IA_Le.Mars.Muni.AP.725484_TMY3
USA_IA_Mason.City.725485_TMY2
USA_IA_Oelwein.Muni.AP.725488_TMY3
USA_IA_Orange.City.Muni.AP.725489_TMY3
USA_IA_Spencer.Muni.AP.726500_TMY3
USA_IA_Storm.Lake.Muni.AP.725496_TMY3
USA_IA_Waterloo.725480_TMY2
USA_IA_Webster.City.Muni.AP.725478_TMY3
USA_ID_Boise.726810_TMY2
USA_ID_Caldwell.AWOS.726813_TMY3
USA_ID_Hailey-Sun.Valley.AP.725865_TMY3
USA_ID_Idaho.Falls-Fanning.Field.725785_TMY3
USA_ID_Malad.City.AP.725786_TMY3
USA_ID_Pocatello.725780_TMY2
USA_ID_Salmon-Lemhi.AWOS.726865_TMY3
USA_ID_Soda.Springs-Tigert.AP.725868_TMY3
USA_ME_Auburn-Lewiston.Muni.AP.726184_TMY3
USA_ME_Augusta.AP.726185_TMY3
USA_ME_Bangor.Intl.AP.726088_TMY
USA_ME_Bar.Harbor.AWOS.726077_TMY3
USA_ME_Brunswick.NAS.743920_TMY3
USA_ME_Millinocket.Muni.AP.726196_TMY3
USA_ME_Portland.726060_TMY2
USA_ME_Rockland-Knox.AWOS.726079_TMY3
USA_ME_Sanford.Muni.AWOS.726064_TMY3
USA_ME_Waterville.AWOS.726073_TMY3
USA_ME_Wiscasset.AP.727135_TMY3
USA_MI_Alpena.726390_TMY2
USA_MI_Cadillac-Wexford.County.AP.726384_TMY3
USA_MI_Escanaba.AWOS.726480_TMY3
USA_MI_Iron.Mountain-Ford.Field.727437_TMY3
USA_MI_Manistee.AWOS.726385_TMY3

USA_MI_Menominee.AWOS.726487_TMY3
USA_MI_Oscoda-Wurtsmith.AFB.726395_TMY3
USA_MI_Pellston-Emmet.County.AP.727347_TMY3
USA_MI_Traverse.City-Cherry.Capital.AP.726387_TMY
USA_MN_Albert.Lea.AWOS.726589_TMY3
USA_MN_Alexandria.Muni.AP.726557_TMY3
USA_MN_Austin.Muni.AP.727566_TMY3
USA_MN_Benson.Muni.AP.727507_TMY3
USA_MN_Cambridge.Muni.AP.727503_TMY3
USA_MN_Edin.Prairie-Flying.Cloud.AP.726579_TMY3
USA_MN_Fairmont.Muni.AWOS.726586_TMY3
USA_MN_Faribault.Muni.AWOS.726563_TMY3
USA_MN_Glenwood.AWOS.726547_TMY3
USA_MN_Hutchinson.AWOS.726569_TMY3
USA_MN_Litchfield.Muni.AP.726583_TMY3
USA_MN_Little.Falls.AWOS.726578_TMY3
USA_MN_Mankato.AWOS.726585_TMY3
USA_MN_Marshall.Muni-Ryan.Field.AWOS.726559_TMY3
USA_MN_Minneapolis-Crystal.AP.726575_TMY3
USA_MN_New.Ulm.Muni.AWOS.726567_TMY3
USA_MN_Owatonna.AWOS.726568_TMY3
USA_MN_Pipestone.AWOS.726566_TMY3
USA_MN_Red.Wing.Muni.AP.726564_TMY3
USA_MN_Redwood.Falls.Muni.AP.726556_TMY3
USA_MN_Rochester.726440_TMY2
USA_MN_Saint.Cloud.726550_TMY2
USA_MN_South.St.Paul.Muni.AP.726603_TMY3
USA_MN_St.Cloud.Muni.AP.726550_TMY3
USA_MN_St.Paul-Downtown.AP.726584_TMY3
USA_MN_Wheaton.AWOS.727533_TMY3
USA_MN_Willmar.Muni.AP.726576_TMY3
USA_MN_Winona.Muni.AWOS.726588_TMY3
USA_MN_Worthington.AWOS.726587_TMY3
USA_MT_Billings-Logan.Intl.AP.726770_TMY
USA_MT_Bozeman-Gallatin.Field.726797_TMY3
USA_MT_Butte-Bert.Mooney.AP.726785_TMY3
USA_MT_Cut.Bank.727796_TMY2

USA_MT_Dillon.726796_TMY
USA_MT_Glasgow.727680_TMY2
USA_MT_Glendive.AWOS.726676_TMY3
USA_MT_Great.Falls.727755_TMY2
USA_MT_Havre.City-County.AP.727770_TMY3
USA_MT_Helena.727720_TMY2
USA_MT_Kalispell-Glacier.Park.Intl.AP.727790_TMY3
USA_MT_Lewistown.726776_TMY2
USA_MT_Livingston-Mission.Field.726798_TMY3
USA_MT_Miles.City.742300_TMY2
USA_MT_Missoula.727730_TMY2
USA_MT_Sidney-Richland.Muni.AP.727687_TMY3
USA_MT_Wolf.Point.Intl.AP.727686_TMY3
USA_ND_Bismarck.727640_TMY2
USA_ND_Dickinson.Muni.AP.727645_TMY3
USA_NH_Berlin.Muni.AP.726160_TMY3
USA_NH_Concord.726050_TMY2
USA_NH_Laconia.Muni.AWOS.726155_TMY3
USA_NH_Mount.Washington.726130_TMY3
USA_NY_Binghamton.725150_TMY2
USA_NY_Fort.Drum-Wheeler.Sack.AAF.743700_TMY3
USA_NY_Glens.Falls-Bennett.Mem.AP.725185_TMY3
USA_NY_Massena.726223_TMY2
USA_NY_Monticello.AWOS.725145_TMY3
USA_NY_Utica-Oneida.County.AP.725197_TMY3
USA_NY_Watertown.AP.726227_TMY3
USA_SD_Aberdeen.Rgnl.AP.726590_TMY3
USA_SD_Brookings.AWOS.726515_TMY3
USA_SD_Ellsworth.AFB.726625_TMY3
USA_SD_Huron.726540_TMY2
USA_SD_Mitchell.AWOS.726545_TMY3
USA_SD_Mobridge.Muni.AP.726685_TMY3
USA_SD_Pierre.726686_TMY2
USA_SD_Rapid.City.726620_TMY2
USA_SD_Sioux.Falls.726510_TMY2
USA_SD_Watertown.Muni.AP.726546_TMY3
USA_UT_Hanksville.AP.724735_TMY3

USA_UT_Vernal.AP.725705_TMY3
USA_VT_Burlington.726170_TMY2
USA_VT_Montpelier.AP.726145_TMY3
USA_VT_Rutland.State.AP.725165_TMY3
USA_VT_Springfield-Hartnes.State.AP.726115_TMY3
USA_WI_Appleton-Outagamie.County.AP.726457_TMY3
USA_WI_Eau.Claire.726435_TMY2
USA_WI_Ephraim.AWOS.726626_TMY3
USA_WI_Green.Bay.726450_TMY2
USA_WI_Janesville-Rock.County.AP.726415_TMY3
USA_WI_La.Crosse.726430_TMY2
USA_WI_Lone.Rock.AP.726416_TMY3
USA_WI_Madison.726410_TMY2
USA_WI_Manitowac.Muni.AWOS.726455_TMY3
USA_WI_Marshfield.Muni.AP.726574_TMY3
USA_WI_Milwaukee.726400_TMY2
USA_WI_Mosinee-Central.Wisconsin.AP.726465_TMY3
USA_WI_Rice.Lake.Muni.AP.726467_TMY3
USA_WI_Sturgeon.Bay-Door.County.AP.726458_TMY3
USA_WI_Watertown.Muni.AP.726464_TMY3
USA_WI_Wausau.Muni.AP.726463_TMY3
USA_WI_Wittman.Rgnl.AP.726456_TMY3
USA_WY_Casper-Natrona.County.Intl.AP.725690_TMY
USA_WY_Cheyenne.725640_TMY2
USA_WY_Cody.Muni.AWOS.726700_TMY3
USA_WY_Evanston-Uinta.County.AP-Burns.Field.725775_TMY3
USA_WY_Gillette-Gillette.County.AP.726650_TMY3
USA_WY_Green.River-Greater.Green.River.Intergalactic.Spaceport.725744_TMY
USA_WY_Lander.725760_TMY2
USA_WY_Laramie-General.Brees.Field.725645_TMY3
USA_WY_Rawlins.Muni.AP.725745_TMY3
USA_WY_Riverton.Rgnl.AP.725765_TMY3
USA_WY_Rock.Springs.725744_TMY2
USA_WY_Sheridan.726660_TMY2
USA_WY_Worland.Muni.AP.726665_TMY3
Climate Zone 7
USA_CO_Aspen-Pitkin.County-Sardy.Field.724676_TMY3

USA_CO_Gunnison.County.AWOS.724677_TMY3
USA_CO_Hayden-Yampa.AWOS.725715_TMY3
USA_CO_Leadville-Lake.County.AP.724673_TMY3
USA_ME_Caribou.727120_TMY2
USA_ME_Edmundston-Northern.Aroostook.Rgnl.AP.726083_TMY3
USA_ME_Houlton.Intl.AP.727033_TMY3
USA_ME_Presque.Isle.Muni.AP.727130_TMY3
USA_MI_Chippewa.County.Intl.AP.727344_TMY3
USA_MI_Hancock-Houghton.County.AP.727440_TMY3
USA_MI_Houghton-Lake.Roscommon.County.AP.726380_TMY3
USA_MI_Ironwood.AWOS.727445_TMY3
USA_MI_Sault.Ste.Marie-Sanderson.Field.727340_TMY
USA_MN_Aitkin.AWOS.727504_TMY3
USA_MN_Baudette.Intl.AP.727476_TMY3
USA_MN_Bemidji.Muni.AP.727550_TMY3
USA_MN_Brainerd-Crow.Wing.County.AP.726555_TMY3
USA_MN_Cloquet.AWOS.726558_TMY3
USA_MN_Crane.Lake.AWOS.727473_TMY3
USA_MN_Crookston.Muni.Field.727452_TMY3
USA_MN_Detroit.Lakes.AWOS.727457_TMY3
USA_MN_Duluth.727450_TMY2
USA_MN_Ely.Muni.AP.727459_TMY3
USA_MN_Eveleth.Muni.AWOS.727474_TMY3
USA_MN_Fergus.Falls.AWOS.726560_TMY3
USA_MN_Fosston.AWOS.727505_TMY3
USA_MN_Grand.Rapids.AWOS.727458_TMY3
USA_MN_Hallock.727478_TMY3
USA_MN_Hibbing-Chisholm.Hibbing.AP.727455_TMY3
USA_MN_International.Falls.727470_TMY2
USA_MN_Mora.Muni.AWOS.727475_TMY3
USA_MN_Orr.Rgnl.AP.726544_TMY3
USA_MN_Park.Rapids.Muni.AP.727453_TMY3
USA_MN_Roseau.Muni.AWOS.727477_TMY3
USA_MN_Silver.Bay.Muni.AP.727556_TMY3
USA_MN_Thief.River.AWOS.727555_TMY3
USA_MN_Two.Harbors.Muni.AP.727444_TMY3
USA_ND_Devils.Lake.AWOS.727573_TMY3

USA_ND_Fargo.727530_TMY2
USA_ND_Grand.Forks.AFB.727575_TMY3
USA_ND_Jamestown.Muni.AP.727535_TMY3
USA_ND_Minot.727676_TMY2
USA_ND_Williston-Sloulin.Field.Intl.AP.727670_TMY3
USA_WI_Minocqua-Woodruff-Lee.Field.726404_TMY3
USA_WI_Phillips-Price.County.AP.726468_TMY3
USA_WY_Jackson.Hole.AP.725776_TMY3

APPENDIX C. Annual Simulation Result of MPC-based TABS Operation

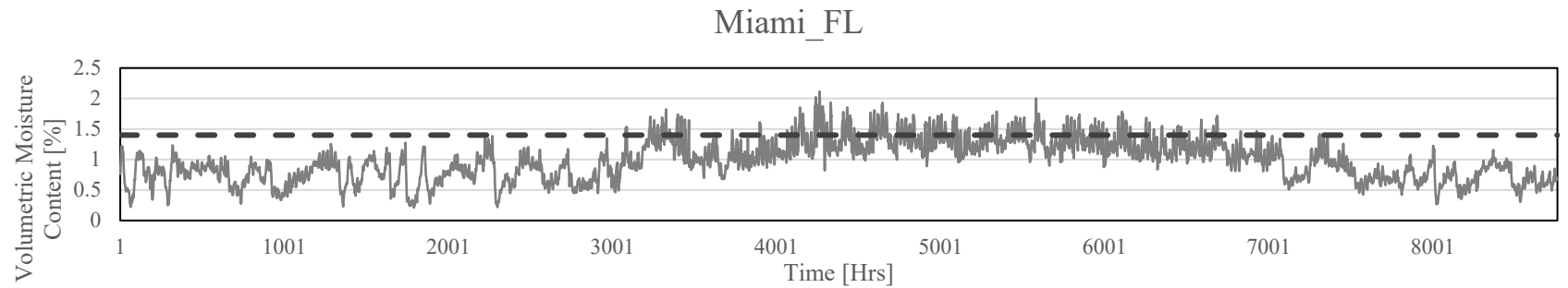


Figure 45. Volumetric moisture content change in concrete layer with TABS operation, disregarding surface condensation risk (Miami_FL)

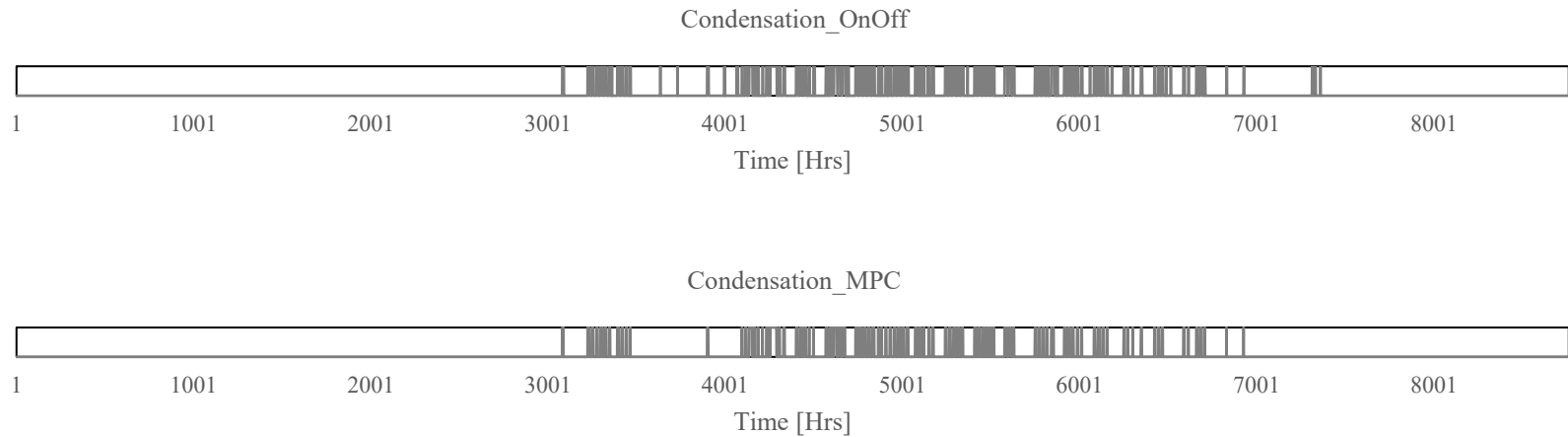


Figure 46. Surface condensation development on TABS with on/off control and MPC (Miami_FL)

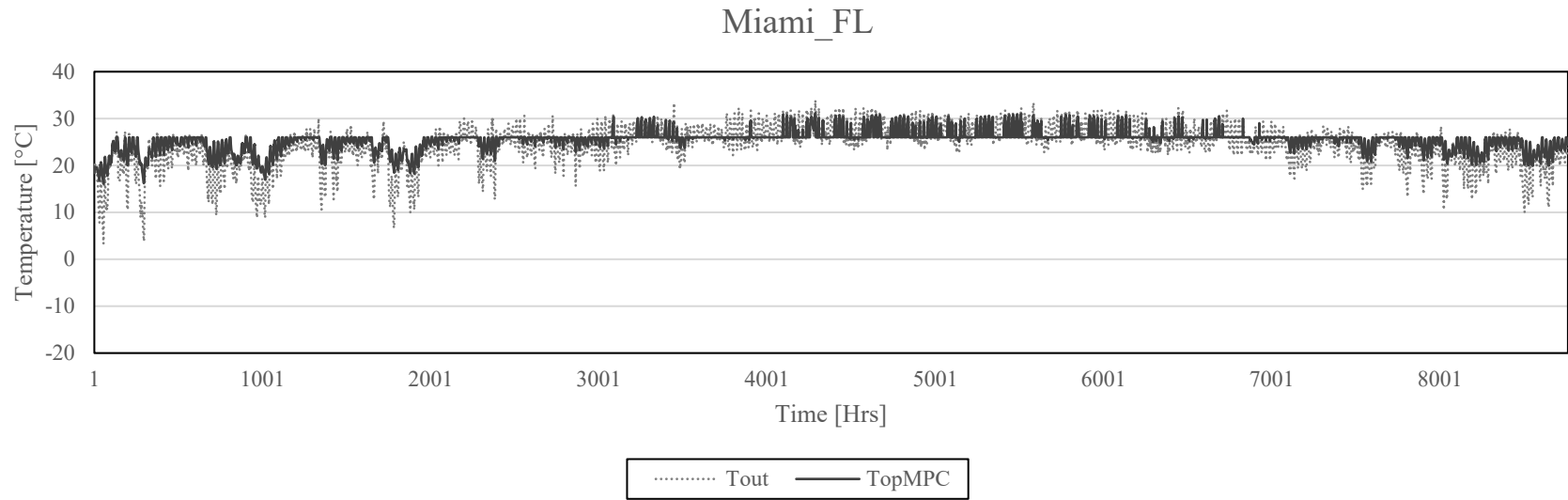


Figure 47. Outdoor air temperature and indoor operative temperature with MPC-based TABS operation (Miami_FL)

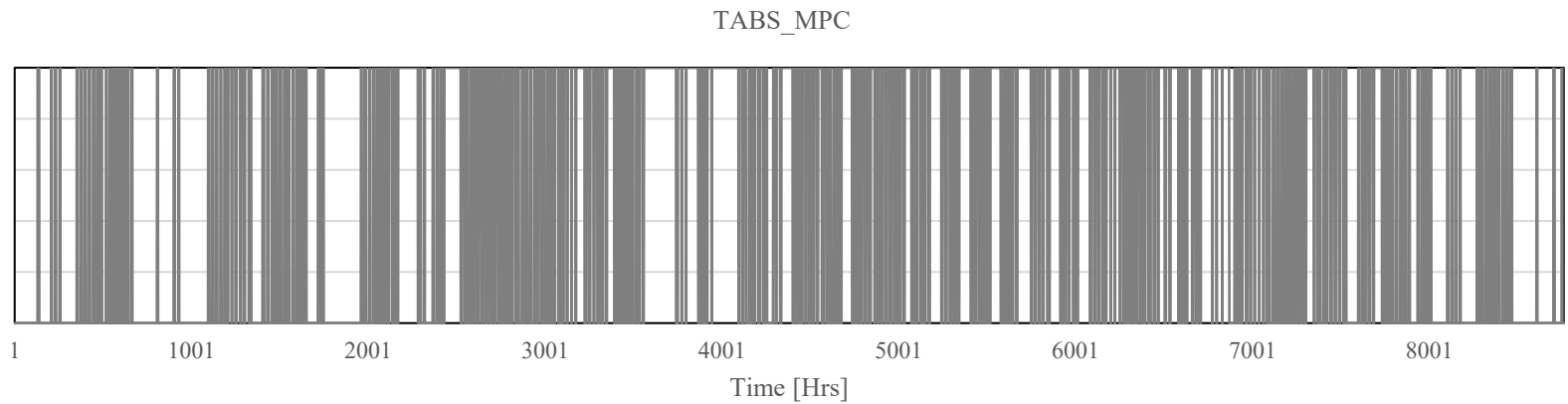


Figure 48. TABS operation with the MPC-based surface condensation prevention framework in cooling season (Miami_FL)

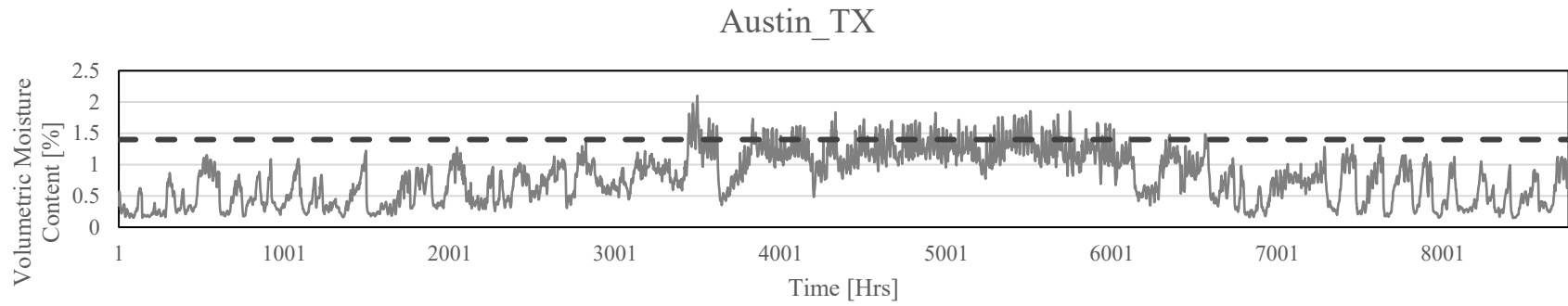


Figure 49. Volumetric moisture content change in concrete layer with TABS operation, disregarding surface condensation risk (Austin_TX)

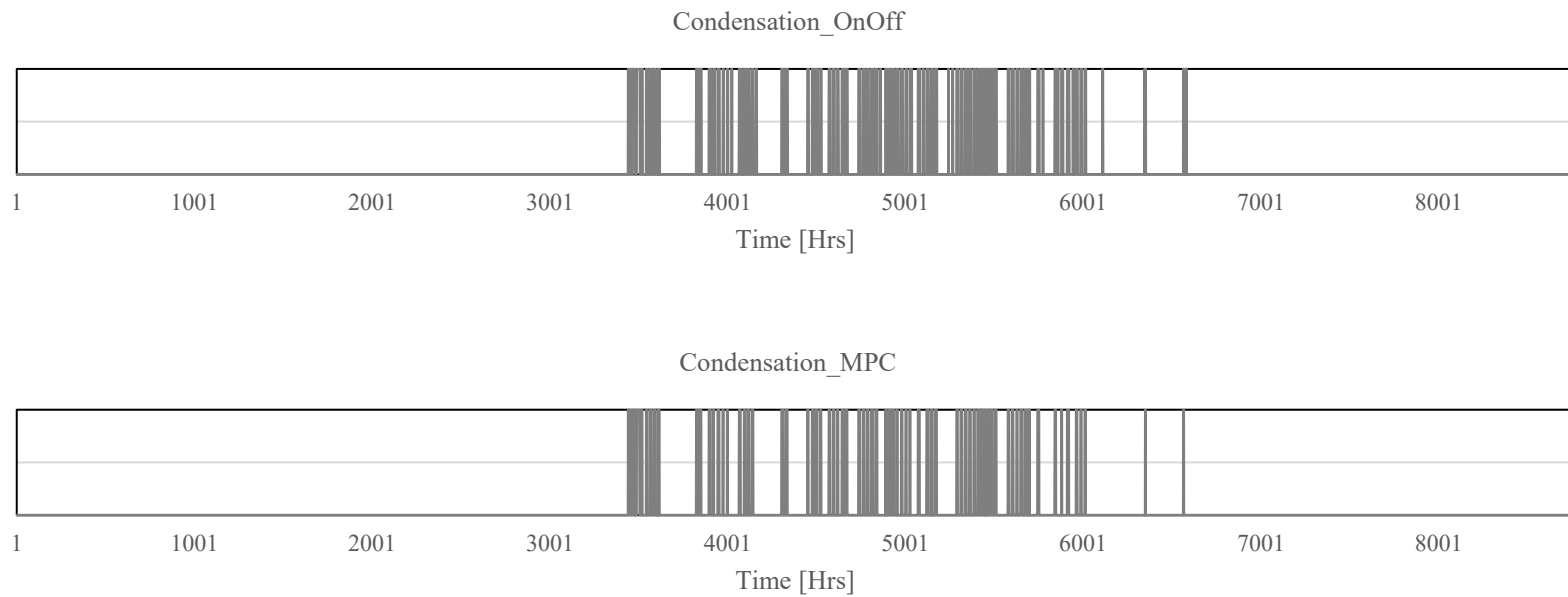


Figure 50. Surface condensation development on TABS with on/off control and MPC (Austin_TX)

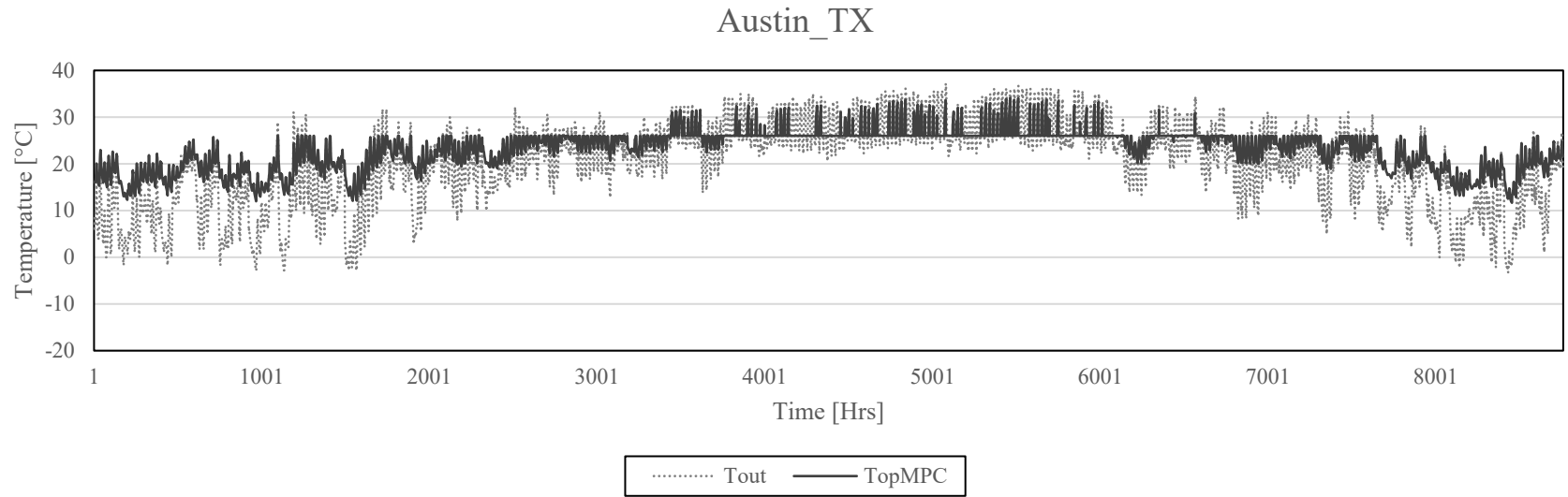


Figure 51. Outdoor air temperature and indoor operative temperature with MPC-based TABS operation (Austin_TX)

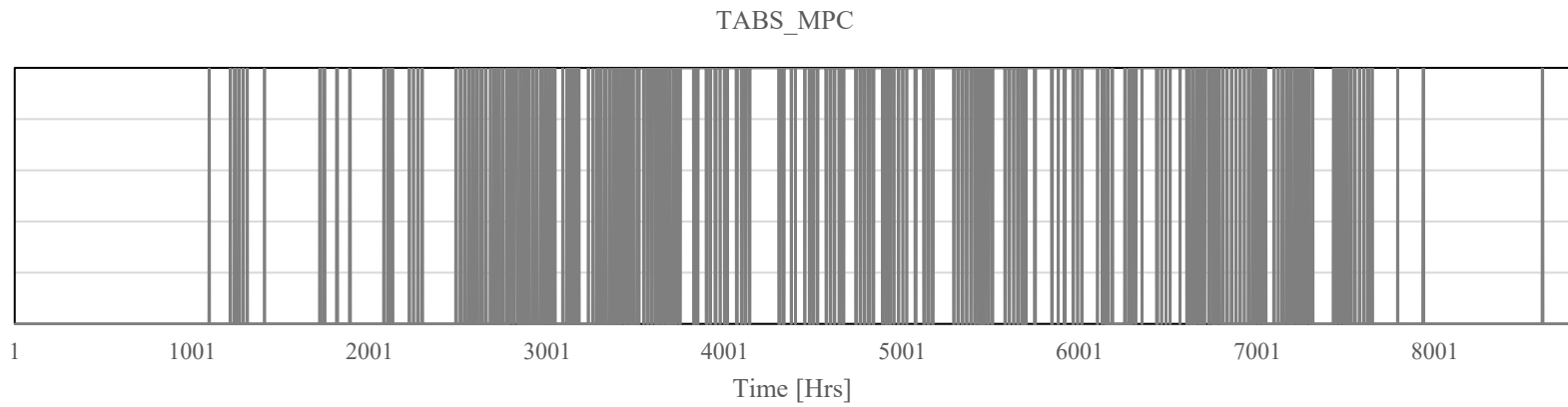


Figure 52. TABS operation with the MPC-based surface condensation prevention framework in cooling season (Austin_TX)

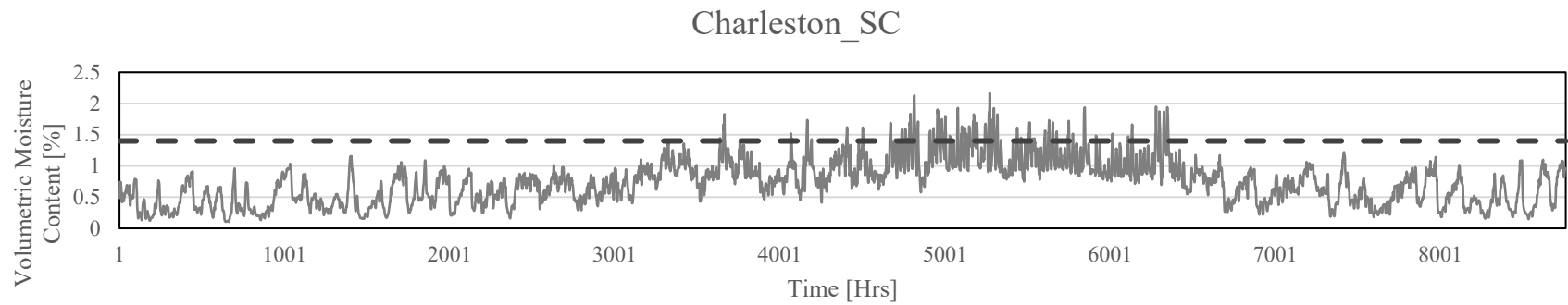


Figure 53. Volumetric moisture content change in concrete layer with TABS operation, disregarding surface condensation risk (Charleston_SC)

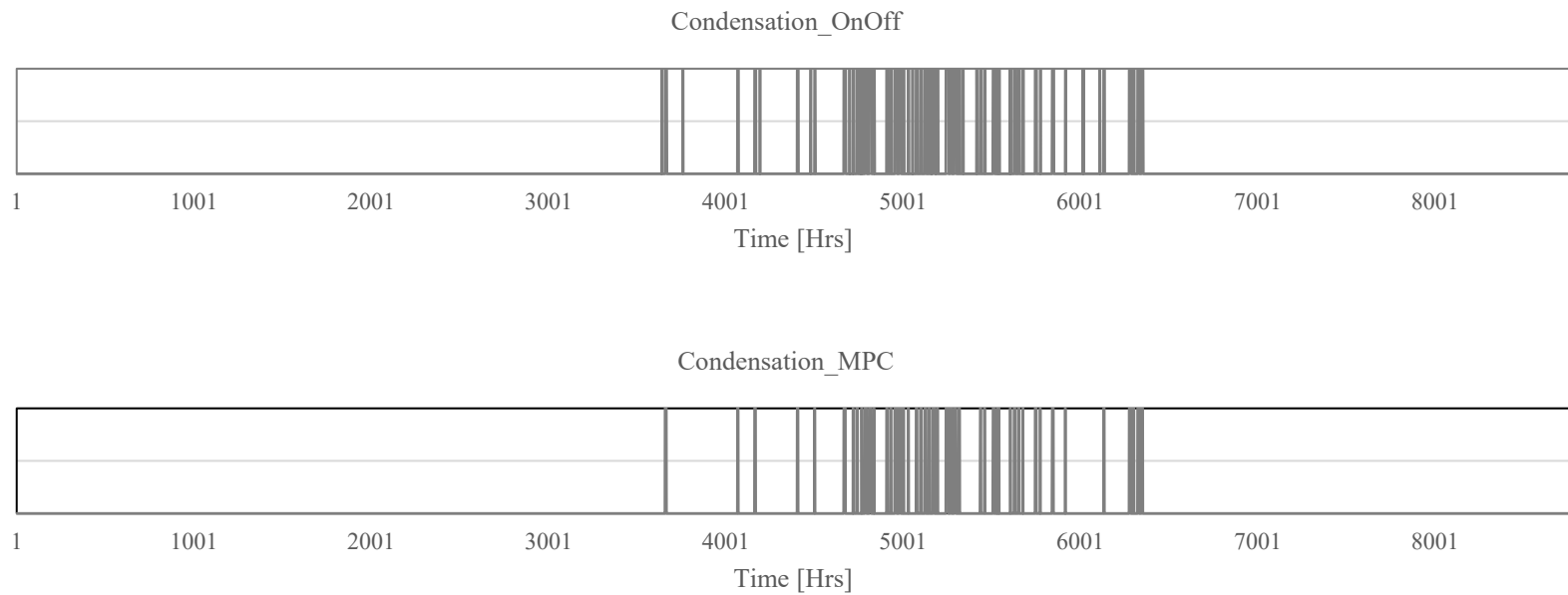


Figure 54. Surface condensation development on TABS with on/off control and MPC (Charleston_SC)

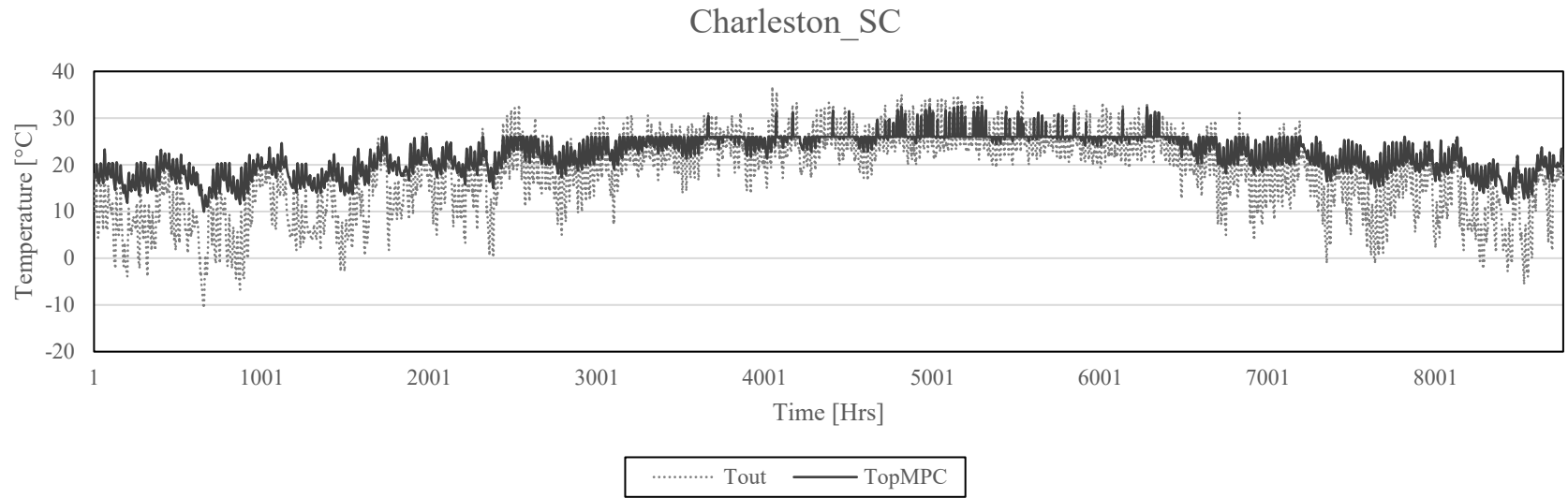


Figure 55. Outdoor air temperature and indoor operative temperature with MPC-based TABS operation (Charleston_SC)

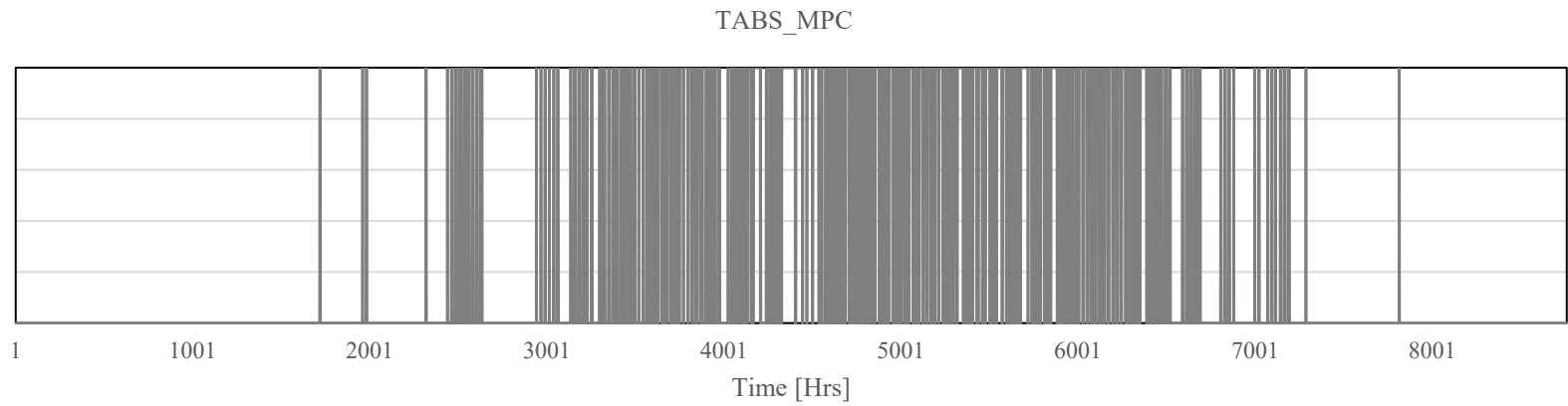


Figure 56. TABS operation with the MPC-based surface condensation prevention framework in cooling season (Charleston_SC)

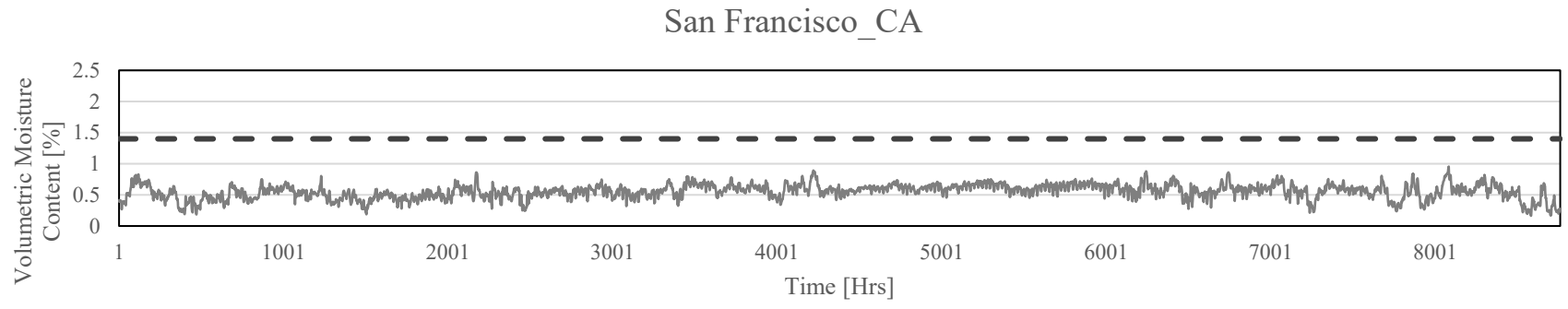


Figure 57. Volumetric moisture content change in concrete layer with TABS operation, disregarding surface condensation risk (San Francisco_CA)

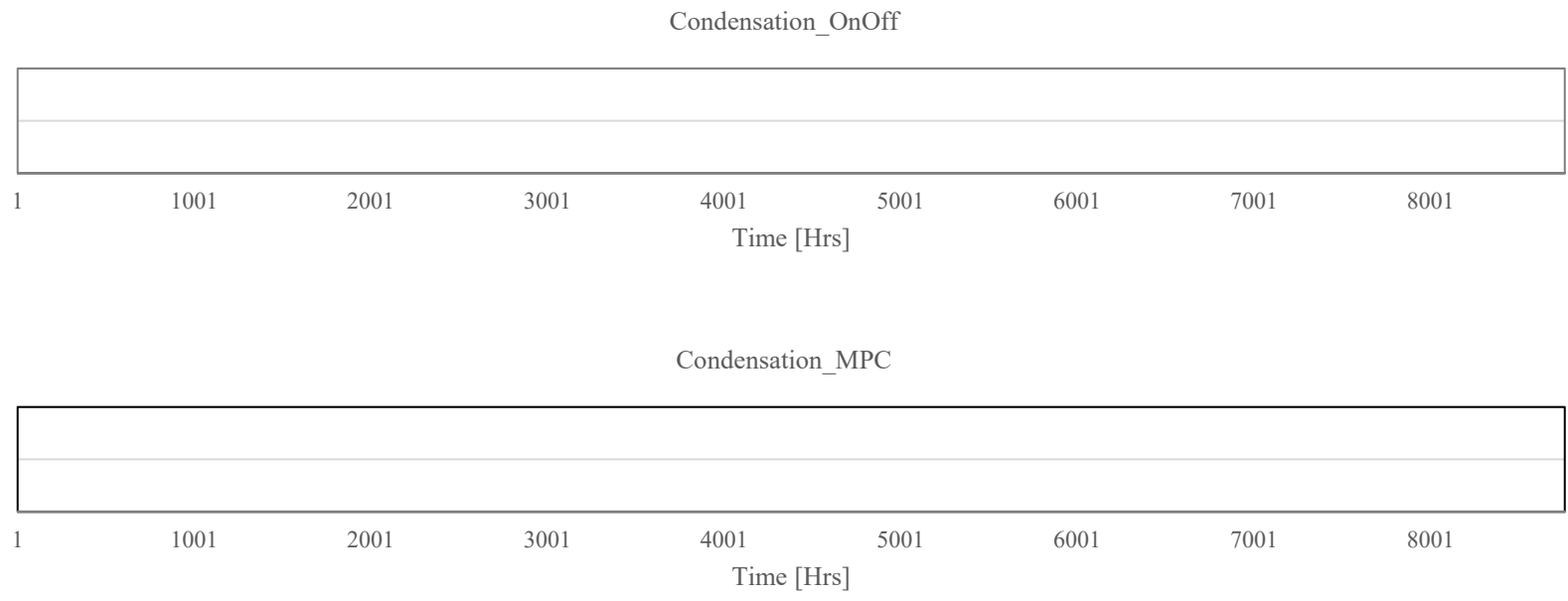


Figure 58. Surface condensation development on TABS with on/off control and MPC (San Francisco_CA)

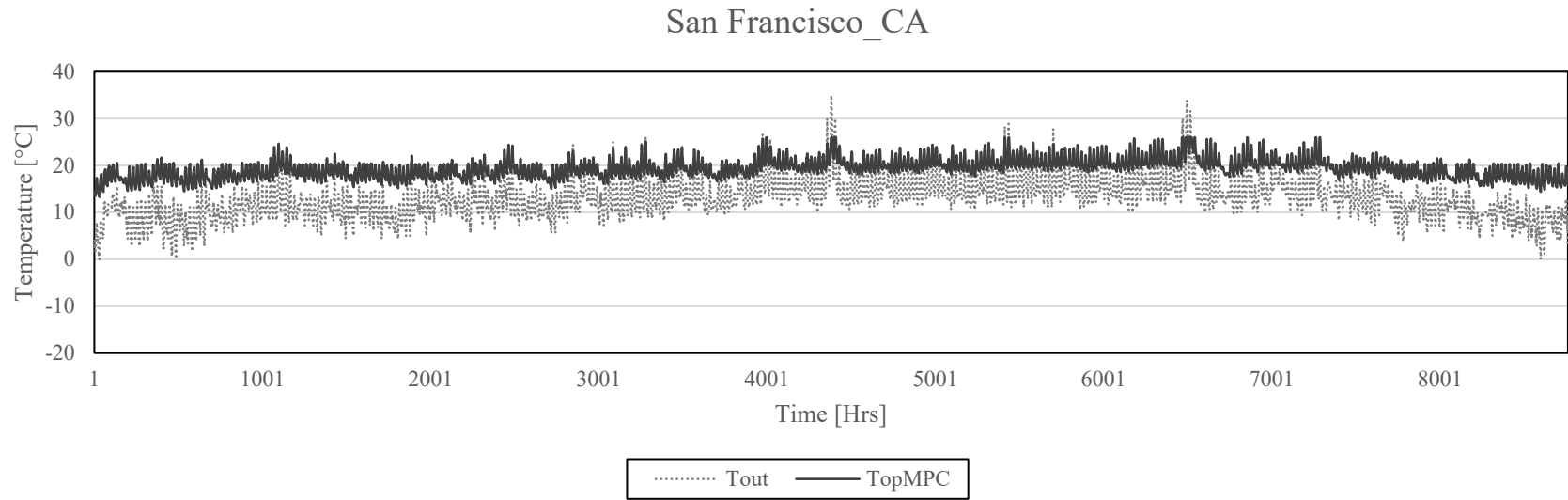


Figure 59. Outdoor air temperature and indoor operative temperature with MPC-based TABS operation (San Francisco_CA)

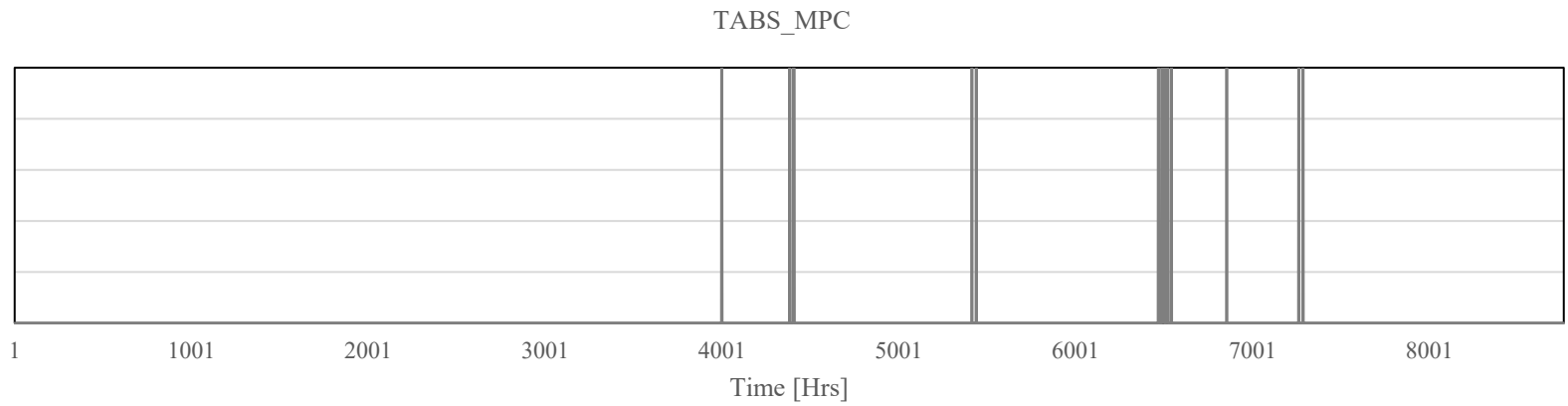


Figure 60. TABS operation with the MPC-based surface condensation prevention framework in cooling season (San Francisco_CA)

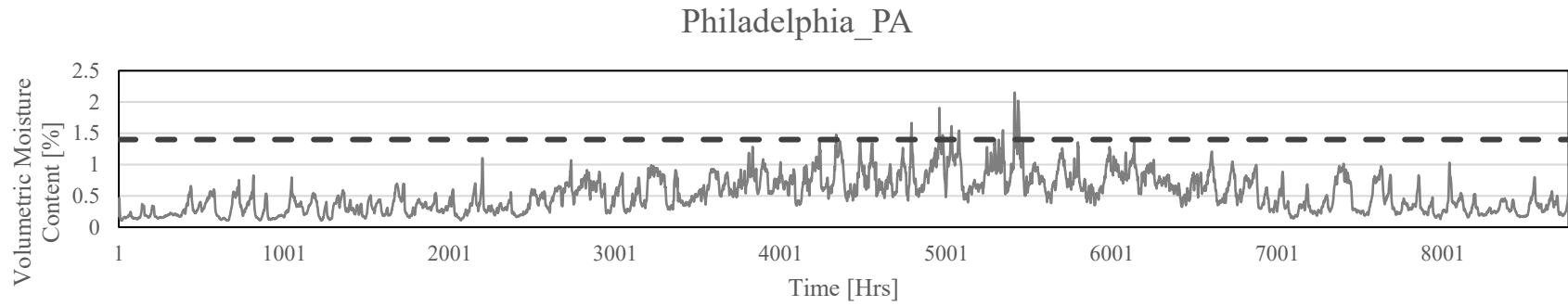


Figure 61. Volumetric moisture content change in concrete layer with TABS operation, disregarding surface condensation risk (Philadelphia_PA)

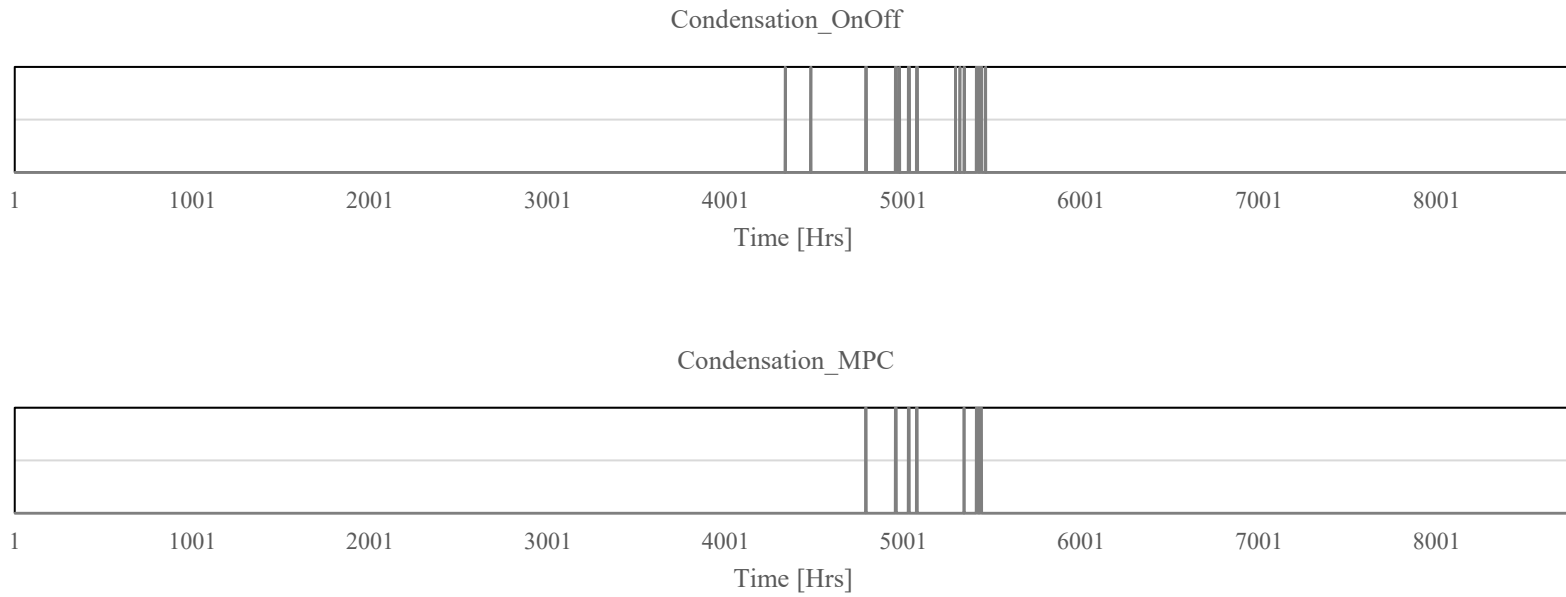


Figure 62. Surface condensation development on TABS with on/off control and MPC (Philadelphia_PA)

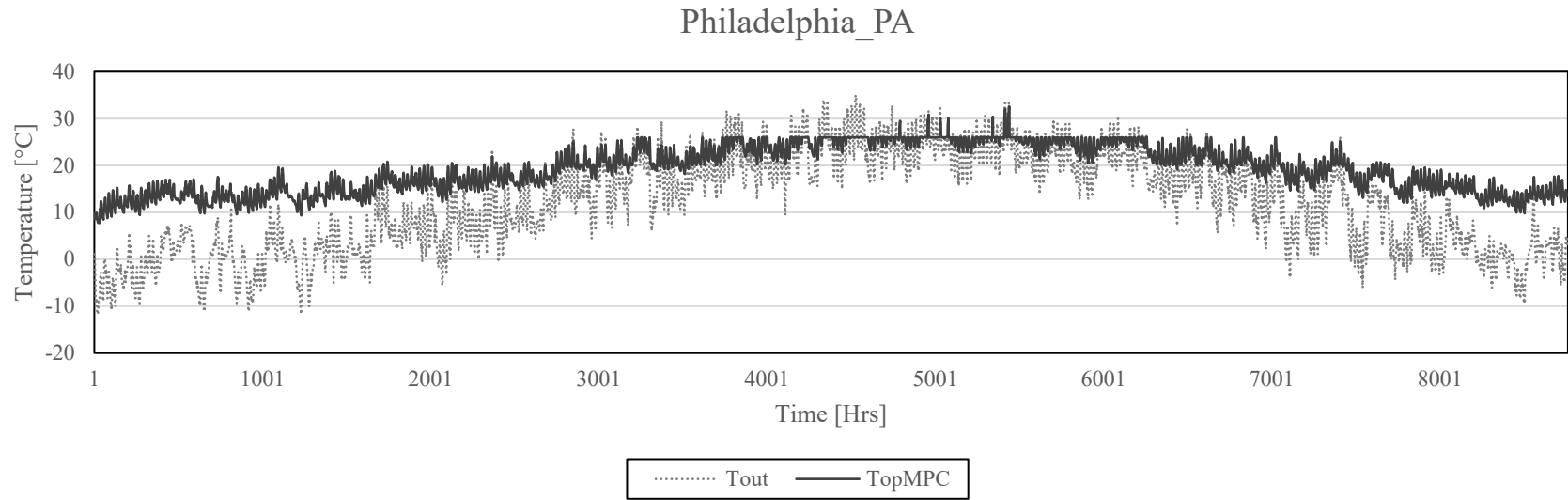


Figure 63. Outdoor air temperature and indoor operative temperature with MPC-based TABS operation (Philadelphia_PA)

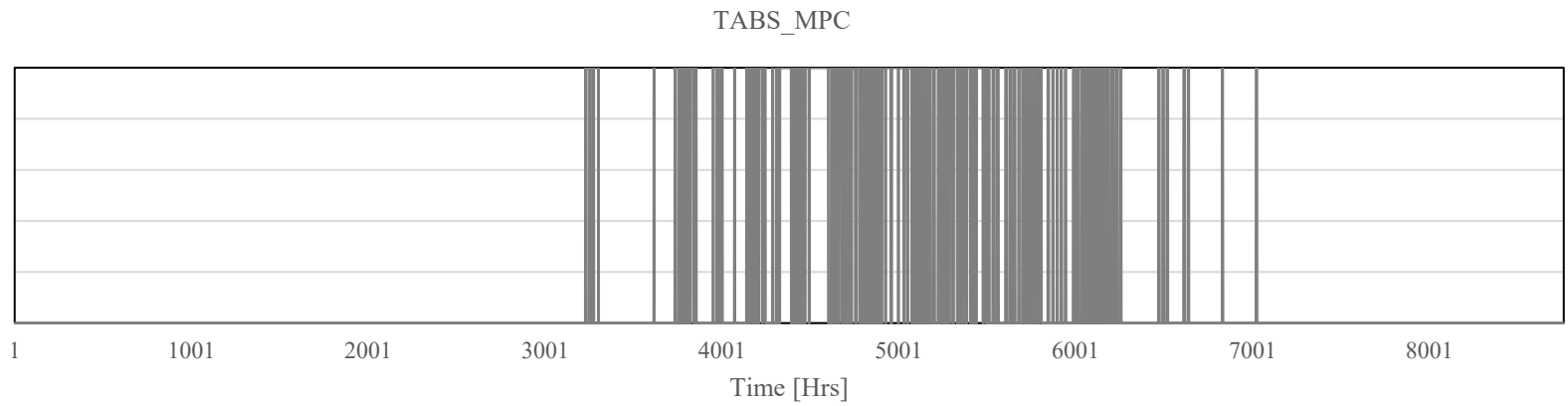


Figure 64. TABS operation with the MPC-based surface condensation prevention framework in cooling season (Philadelphia_PA)

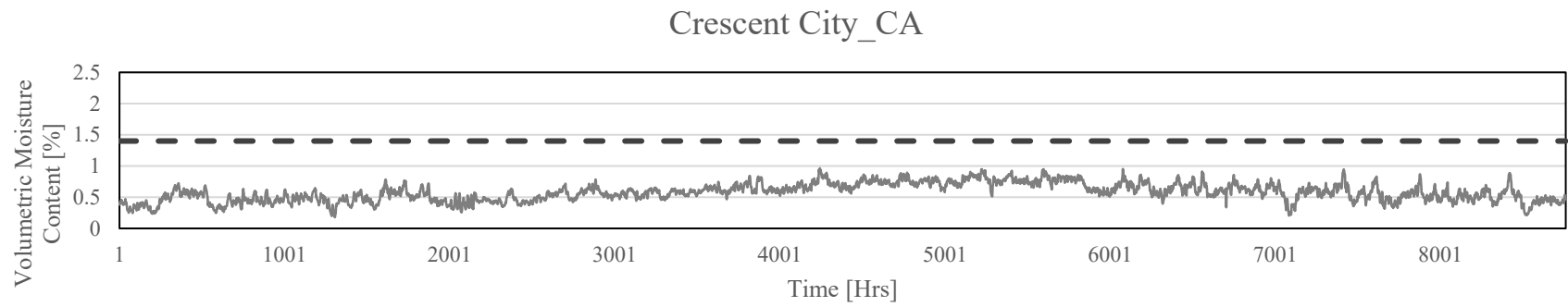


Figure 65. Volumetric moisture content change in concrete layer with TABS operation, disregarding surface condensation risk (Crescent City_CA)

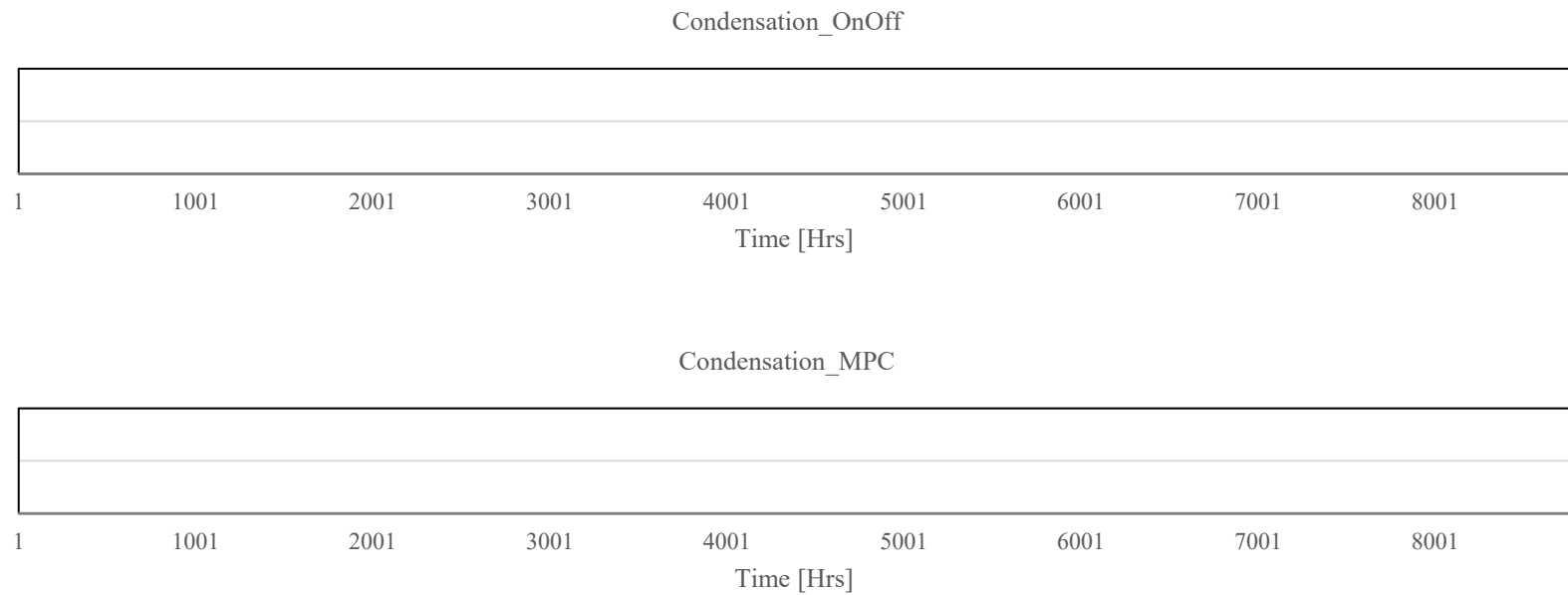


Figure 66. Surface condensation development on TABS with on/off control and MPC (Crescent City_CA)

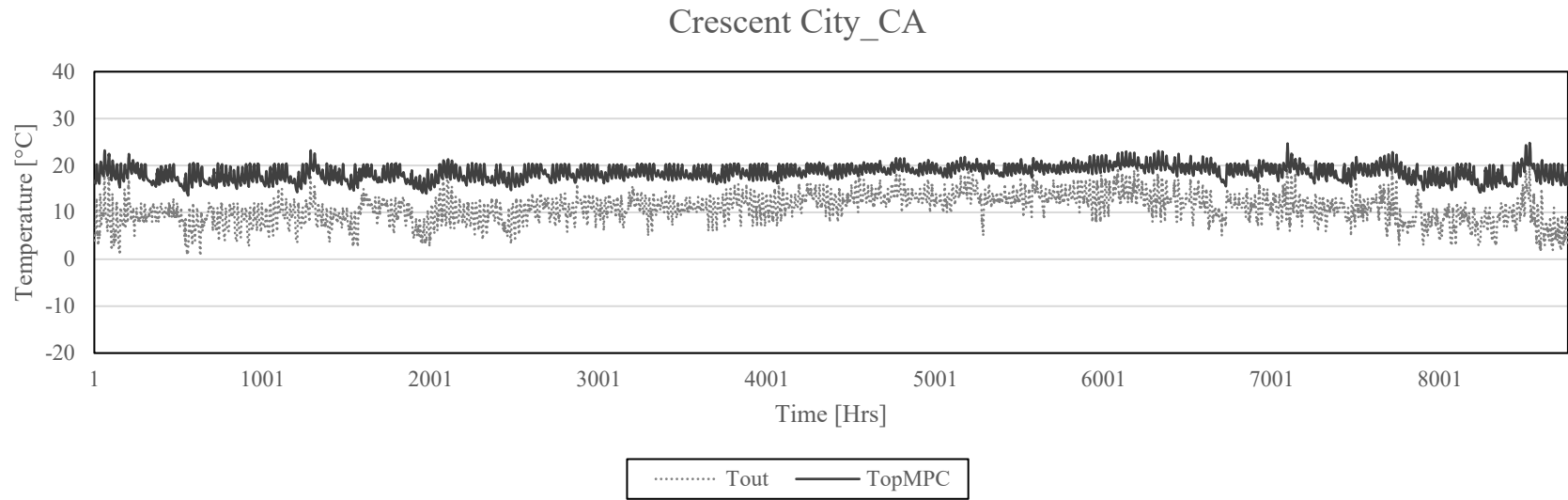


Figure 67. Outdoor air temperature and indoor operative temperature with MPC-based TABS operation (Crescent City_CA)

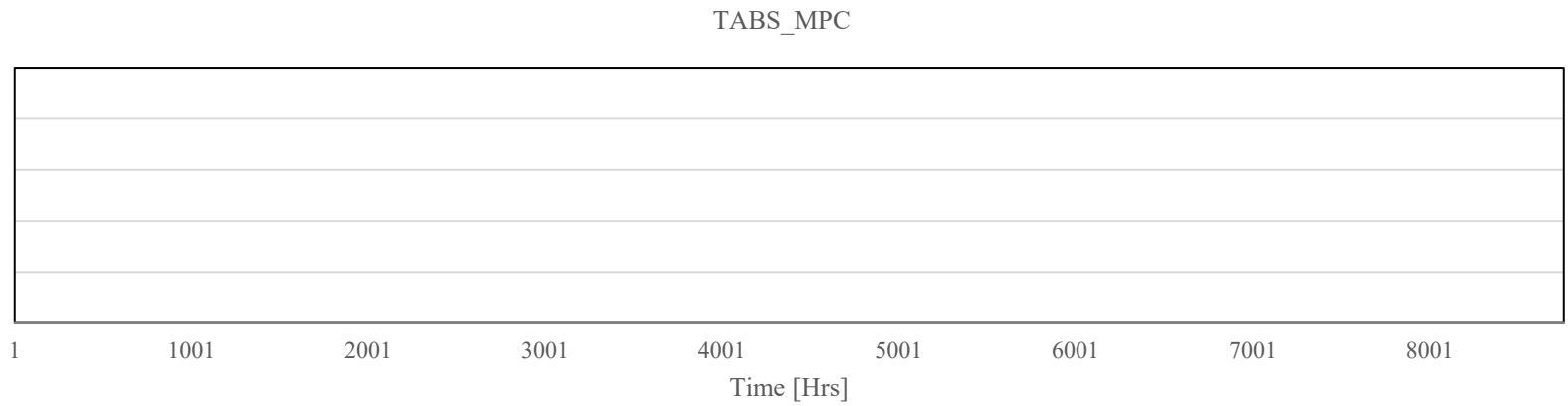


Figure 68. TABS operation with the MPC-based surface condensation prevention framework in cooling season (Crescent City_CA)

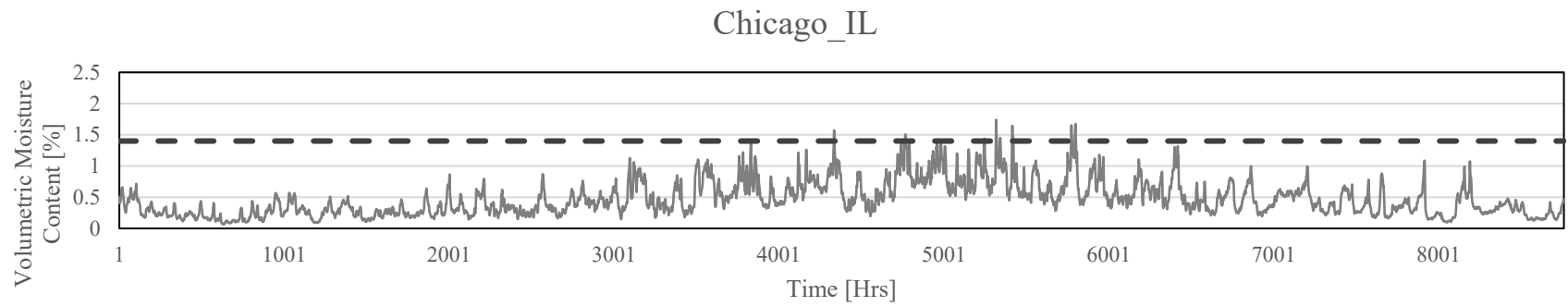


Figure 69. Volumetric moisture content change in concrete layer with TABS operation, disregarding surface condensation risk (Chicago_IL)

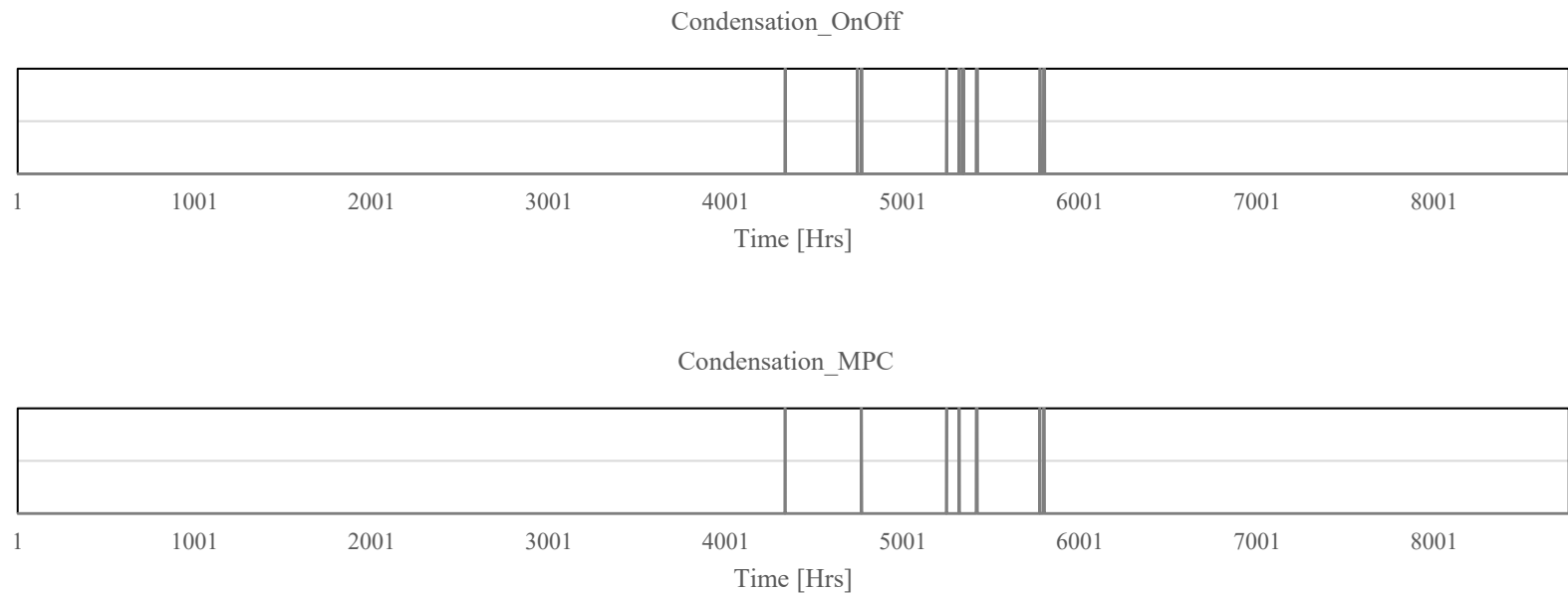


Figure 70. Surface condensation development on TABS with on/off control and MPC (Chicago_IL)

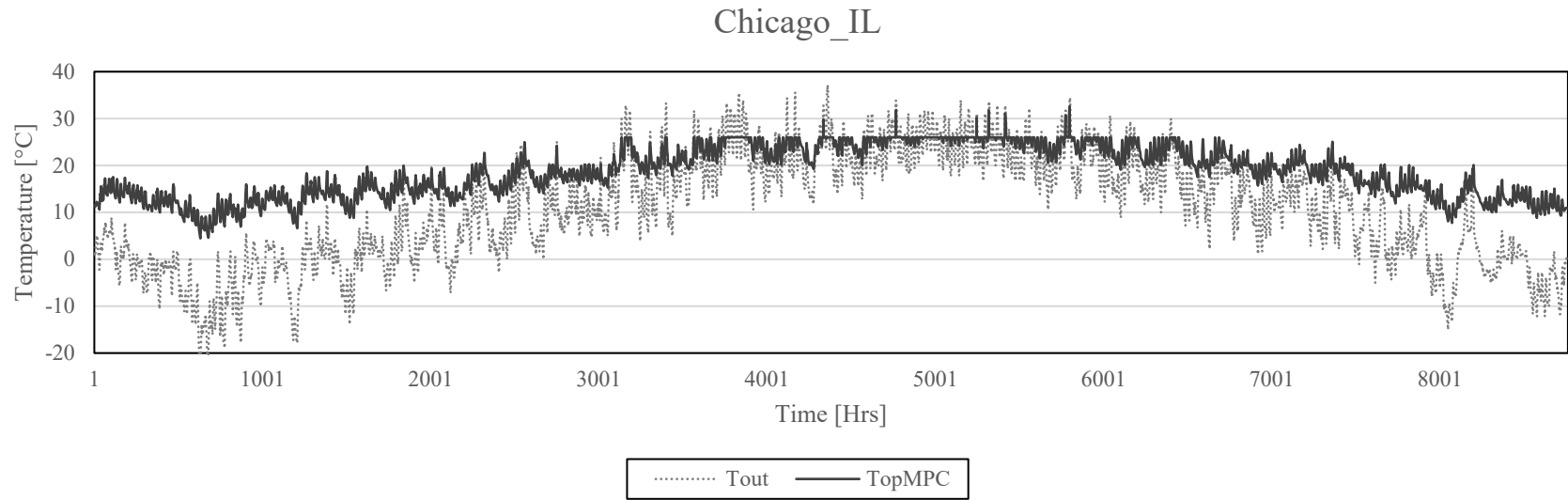


Figure 71. Outdoor air temperature and indoor operative temperature with MPC-based TABS operation (Chicago_IL)

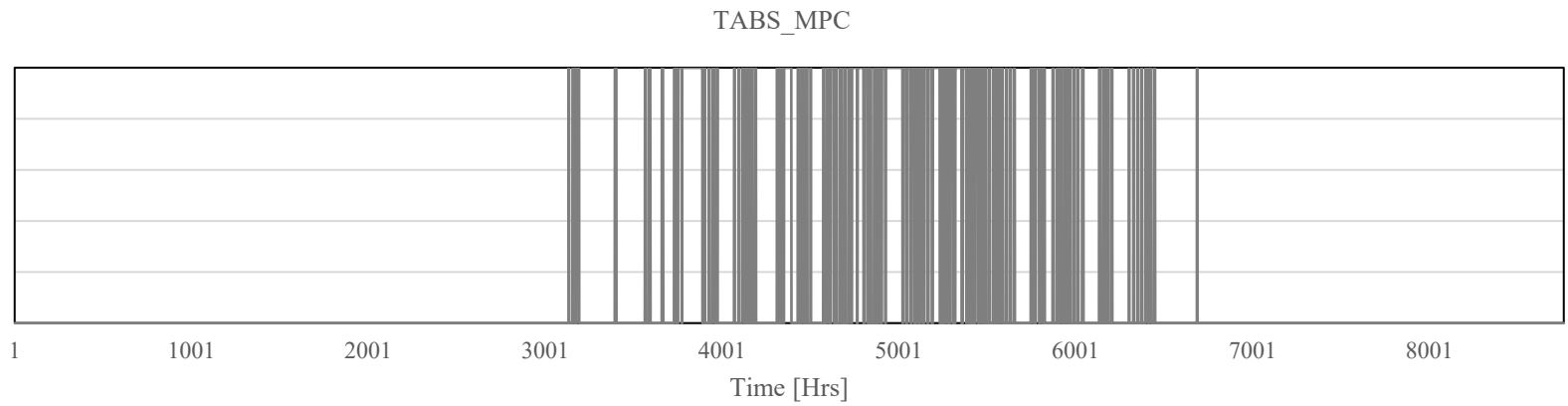


Figure 72. TABS operation with the MPC-based surface condensation prevention framework in cooling season (Chicago_IL)

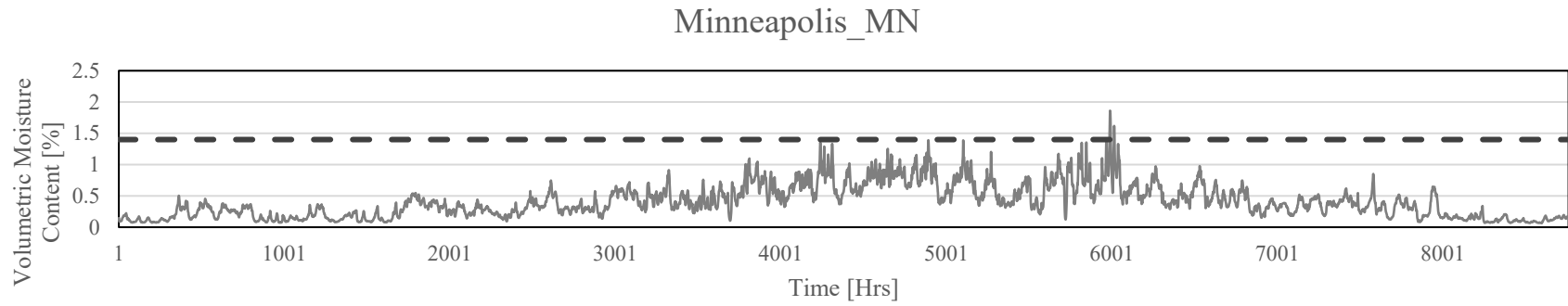


Figure 73. Volumetric moisture content change in concrete layer with TABS operation, disregarding surface condensation risk (Minneapolis_MN)

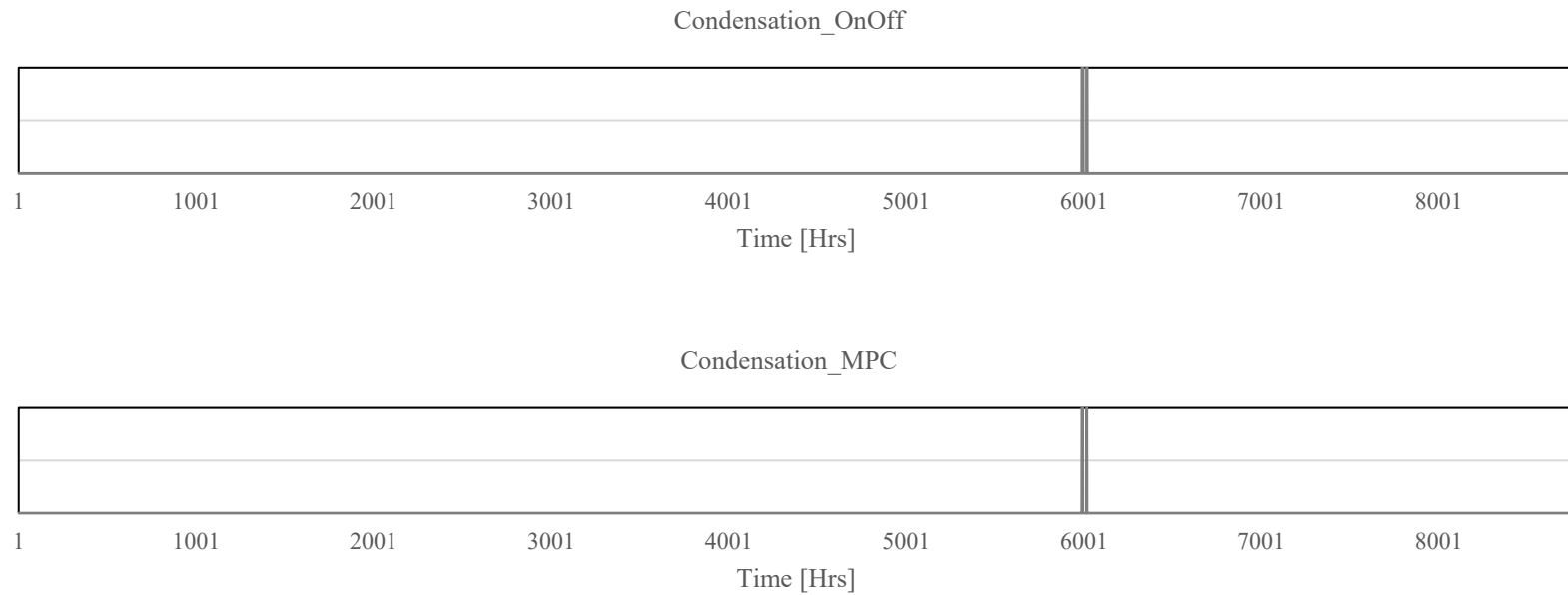


Figure 74. Surface condensation development on TABS with on/off control and MPC (Minneapolis_MN)

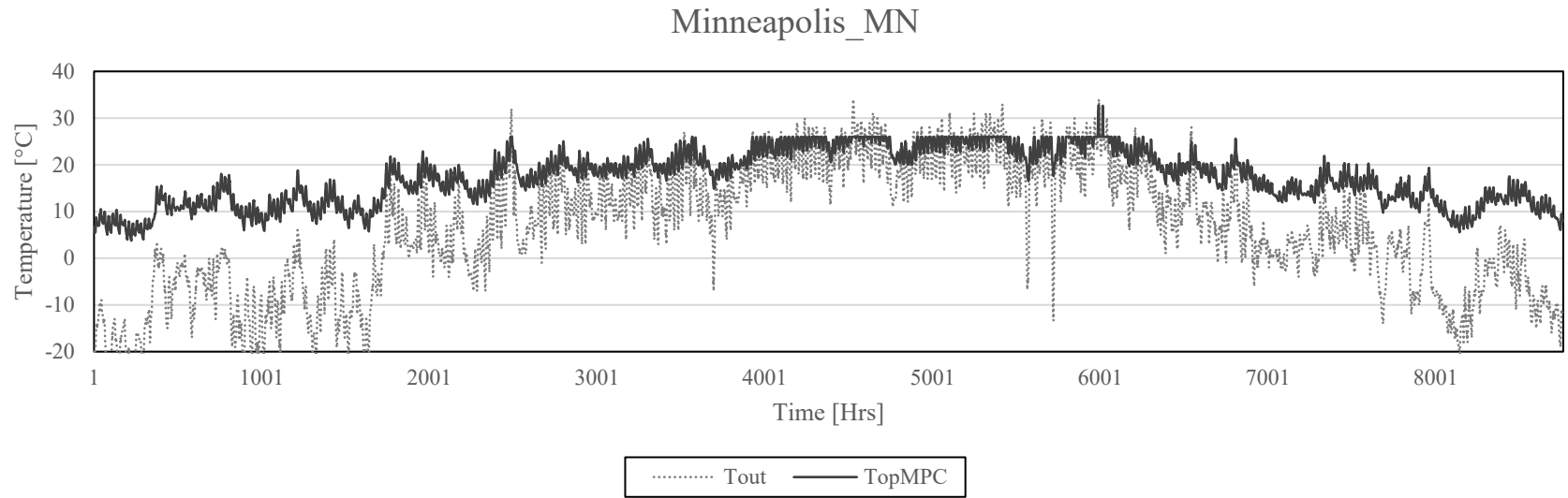


Figure 75. Outdoor air temperature and indoor operative temperature with MPC-based TABS operation (Minneapolis_MN)

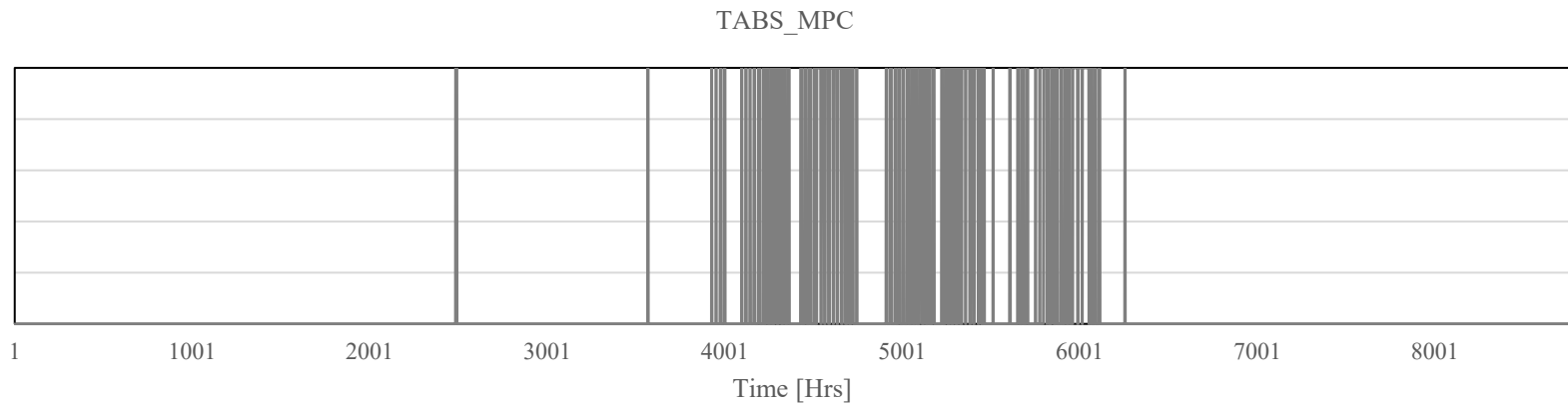


Figure 76. TABS operation with the MPC-based surface condensation prevention framework in cooling season (Minneapolis_MN)

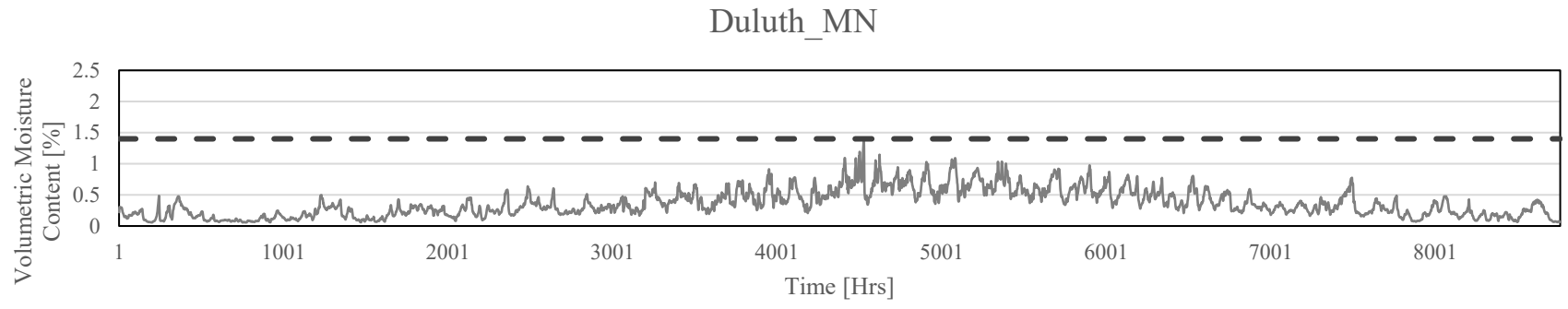


Figure 77. Volumetric moisture content change in concrete layer with TABS operation, disregarding surface condensation risk (Duluth_MN)

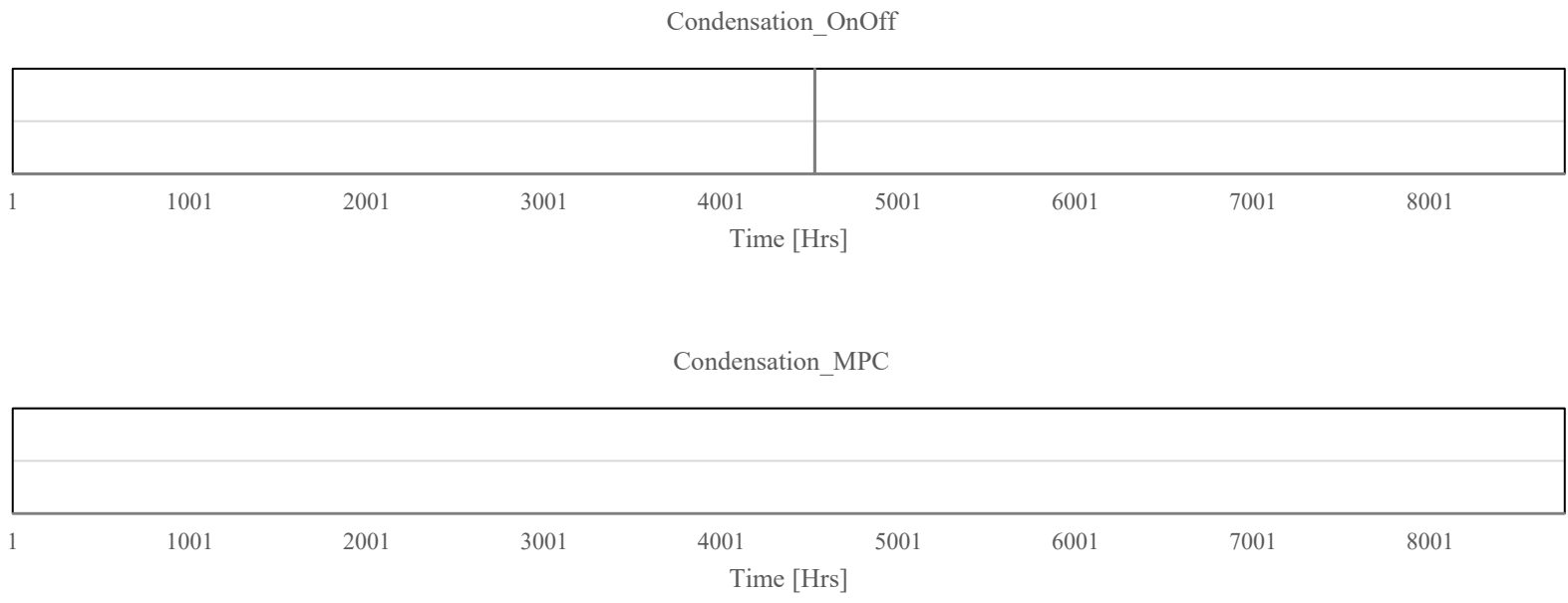


Figure 78. Surface condensation development on TABS with on/off control and MPC (Duluth_MN)

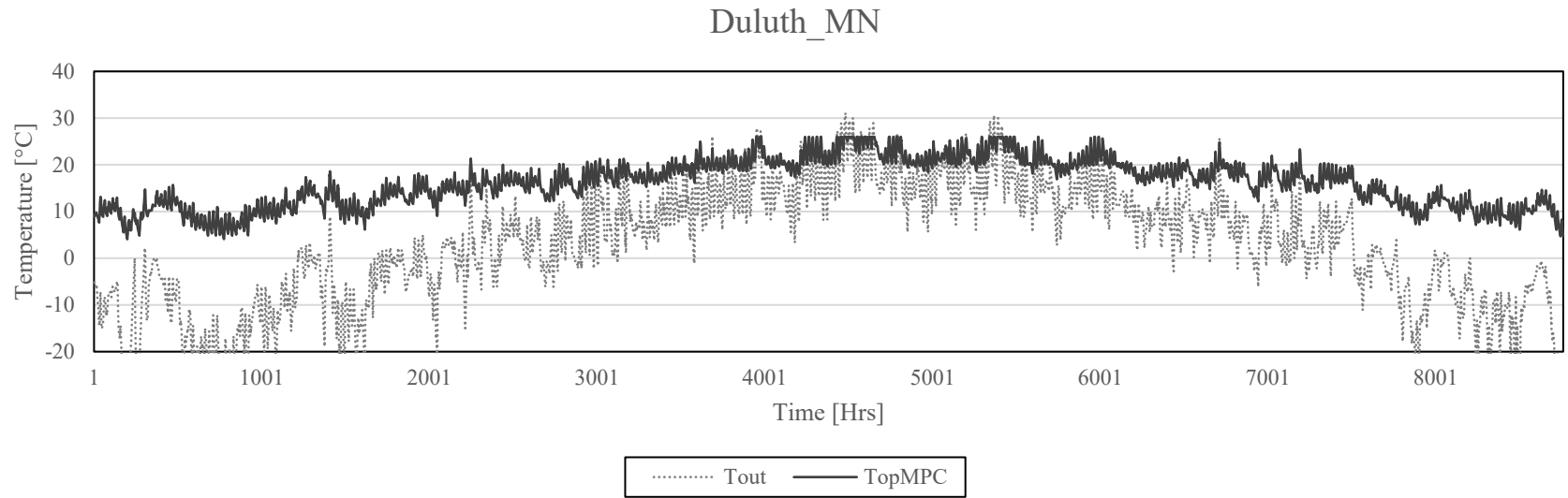


Figure 79. Outdoor air temperature and indoor operative temperature with MPC-based TABS operation (Duluth_MN)

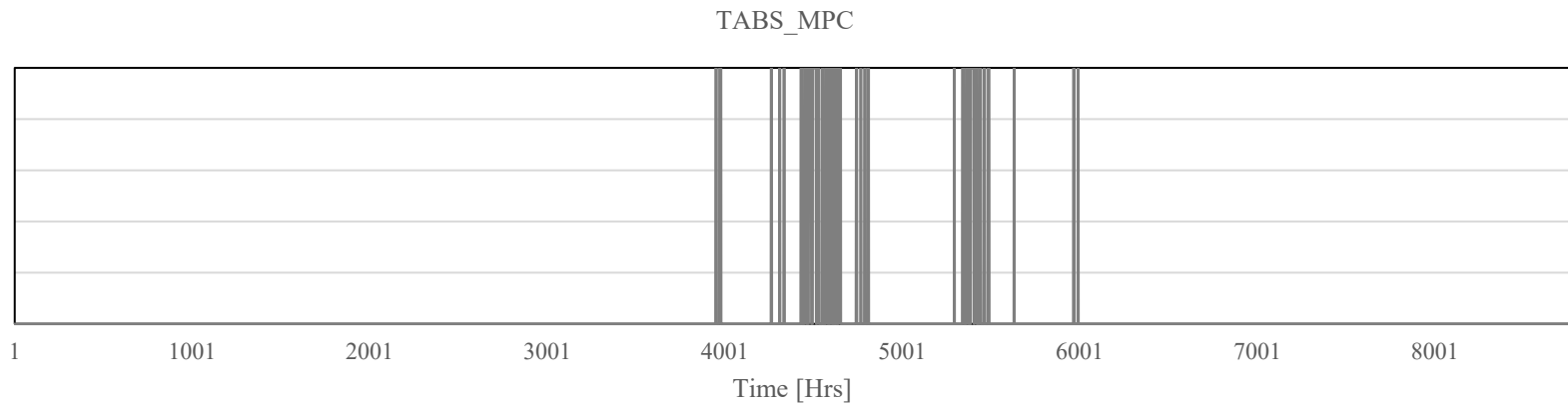


Figure 80. TABS operation with the MPC-based surface condensation prevention framework in cooling season (Duluth_MN)

APPENDIX D. Summary of Parameter Values for the Site Cooling Energy Calculation

Table 19. Summary of parameter values for the site cooling energy calculation

Parameter	Value	References
COP for water-to-water compression chiller (Mechanical ventilation cooling)	3.5 [-]	[107–109]
COP for water-to-water compression chiller (TABS)	4.5 [-]	[107–109]
Mechanical ventilation temperature difference	10 [K]	[111]
TABS temperature difference	3 [K]	[111]
Outdoor air supply rate	426.6 [m ³ /hr] = 0.27 [ACH]	[10]
Total pressure drop for air system	1000 [Pa]	[112]
Blower efficiency	0.6 [-]	[112]
Blower electric power	0.55 [W/m ³ hr]	[111]
Total pressure drop for water system	30000 [Pa]	[112]
Pump efficiency	0.72 [-]	[112]
Closed cooling tower efficiency	$(T_{\text{inlet}} - T_{\text{outlet}}) / (T_{\text{inlet}} - T_{\text{wet-bulb}})$ [-]	[113, 114]
Cooling tower electric power	0.033 [kW/kW]	[111]